

Development and application of  
a Cylindrical Active Tracker and Calorimeter system  
for Hyperon-proton scattering “CATCH”

(ハイペロン-陽子散乱実験に向けた  
円筒形飛跡検出器・カロリメータシステム  
“CATCH”の開発と利用)

Yuya Akazawa  
(赤澤 雄也)

平成30年



## Abstract

A scattering experiment between a  $\Sigma$  hyperon and a proton is planned at J-PARC (J-PARC E40) in order to investigate the baryon-baryon interaction and to confirm the repulsive force due to the quark Pauli effect, which is considered as one of the origins of the repulsive core in the nuclear force.

In order to measure the cross section of  $\Sigma p$  scattering, a hydrogen target is irradiated with a pion beam and a  $\Sigma$  particle is produced with a reaction of  $\pi + p \rightarrow \Sigma + K^+$ . The probability that this produced  $\Sigma$  is scattered with a proton in the target is measured for the cross section.

In the past experiment at KEK, all particles related to the scattering reaction needed to be measured with the “imaging method” by using imaging detectors such as a scintillating fiber active target to identify the scattering event. However the detector response was slow and thus the meson beam intensity was limited to be 250 k/spill (spill  $\simeq$  2 seconds). Due to both the underlying experimental difficulty due to the hyperon’s short lifetime and the low beam intensity, the number of the detected scattering events was only a few tens.

In order to measure the cross section with high statistics and a good accuracy, we introduce a new identification method of the scattering event. In this new method, momenta of a  $\Sigma$  beam and a recoil proton are used without detecting  $\Sigma$  particle directly, and the scattering event can be identified by checking the kinematical consistency that is represented by “ $\Delta E$ ”.  $\Delta E$  is defined as a difference between two values for the recoil proton energy obtained by two different methods. The first value ( $E_{p_{calc}}$ ) is a calculated energy of the recoil proton kinematically from the  $\Sigma$  beam energy and the scattering angle. The second value ( $E_{p_{measure}}$ ) is an actually measured energy. For the  $\Sigma p$  scattering events, the  $\Delta E$  distribution has a peak around zero. From the number of the peak counts, we can derive the cross section of the scattering. Because any slow detectors are not used in this method, a high intensity  $\pi$  beam can be used in order to produce many  $\Sigma$  particles

In order to realize the new experimental method, detector systems for both the  $\Sigma$  beam reconstruction and the recoil proton detection were essential. For the  $\Sigma$  beam reconstruction, the existing spectrometer systems for multi-purposes

are utilized. On the other hand, the recoil proton detector should be a dedicated system with a large acceptance and sufficient performance for detecting  $\Sigma p$  scattering events. For this reason, we developed a new detector system called CATCH (Cylindrical Active Tracker and Calorimeter system for Hyperon-proton scattering).

In the  $\Sigma p$  scattering experiment at J-PARC, a high intensity  $\pi$  beam of  $2 \times 10^7$ /spill (spill is about 2 second beam duration for 6 second beam cycle) is used to produce as many  $\Sigma$  beam as possible via the  $\pi p \rightarrow \Sigma K^+$  reactions. In order to realize the kinematical identification of  $\Sigma p$  scattering, a liquid hydrogen target, which is installed inside CATCH, is quite important because two body reactions of the  $\Sigma$  production and the  $\Sigma p$  scattering can be assured. The momenta of  $\pi$  beam and scattered  $K^+$  are analyzed by each spectrometer in order to reconstruct the momentum of a produced  $\Sigma$  particle. The scattering angle and the kinetic energy of the recoil proton are measured by CATCH in order to identify  $\Sigma p$  scattering events.

CATCH consists of a Cylindrical Fiber Tracker (CFT) and a bismuth germanate (BGO) calorimeter. The CFT is a tracking detector with a fast time response made of 5,000 scintillation fibers with a diameter of 0.75 mm. Each fiber signal is readout by a Multi-Pixel Photon Counter (MPPC,  $1 \times 1$  mm<sup>2</sup>, 400 pixels) fiber by fiber. In order to reconstruct tracks three dimensionally, we realized two types of cylindrical layers where fibers are placed with the straight and spiral configurations on the surface of the cylindrical layer, respectively, by using a special frame with a hole for fixing the fiber position. CFT consists of four straight layers and four spiral layers. At the fabrication of CFT, it was difficult to place fibers at the ideal position exactly. This fiber position could be corrected with cosmic ray data. As for the BGO calorimeter, 24 BGO crystals are placed to surround CFT and are used to measure the kinetic energy of recoil proton. The size of one crystal piece is  $30 \times 25 \times 400$  mm<sup>3</sup>. The waveform of the BGO signal is readout with a Flash ADC in order to separate pile-up events. After each detector was fabricated, CFT and the BGO calorimeter were combined together as CATCH.

In order to evaluate the performance of CATCH, we performed a  $pp$  and  $pC$  scattering experiment at CYRIC (Tohoku University). The Polyethylene (CH<sub>2</sub>) target installed inside CATCH was irradiated by an 80 MeV proton beam, and scattered protons were measured by CATCH. The one of the most

important purposes of this experiment is to evaluate the resolution for the  $\Delta E$  value to identify the scattering event.  $E_{p_{calc}}$  and  $E_{p_{measure}}$  are determined by the angular resolution of CFT and the energy resolutions of CFT and the BGO calorimeter, respectively. The angular resolution was evaluated to be 1.6 degrees ( $\sigma$ ) from the opening angle between two protons emitted from  $pp$  scattering. The energy calibrations of CFT and the BGO calorimeter were performed by using the relation between the energy of the scattered protons and the scattering angle measured by CFT. The energy resolution of the BGO calorimeter was obtained to be 1.5% ( $\sigma$ ) for 80 MeV proton, and that of CFT was obtained to be better than 20% for the energy deposit of a proton in CFT (8 MeV  $\sim$  20MeV). The  $\Delta E$  resolution for the  $pC$  scattering was obtained to be about 2.3 MeV ( $\sigma$ ). Since  $\sigma_{\Delta E}$  depends on the beam energy and kinematics, the estimation for the  $\Sigma p$  scattering experiment is necessary. Based on the obtained angular resolution and energy resolution of CFT and the BGO calorimeter, the  $\Delta E$  resolution for the  $\Sigma p$  scattering was estimated to be better than 5.5 MeV ( $\sigma$ ) for all conditions. This value satisfies the requirement of 7 MeV ( $\sigma$ ) to well discriminate the  $\Delta E$  peak from background.

The (relative) differential cross sections of  $pp$  and  $pC$  scatterings were derived with CATCH and the  $\Delta E$  method. For the newly developed CATCH system, we have established an analysis method for deriving the cross section. Thus we have confirmed that the CATCH system has sufficient performances for the  $\Sigma p$  scattering experiment at J-PARC.



# Contents

<b>1</b>	<b>Introduction</b>	<b>1</b>
1.1	Baryon-Baryon interaction . . . . .	2
1.2	$\Sigma N$ interaction and scattering cross section . . . . .	7
<b>2</b>	<b>A new <math>\Sigma p</math> scattering experiment and requirements for CATCH system</b>	<b>11</b>
2.1	Past Experiment . . . . .	11
2.2	New $\Sigma p$ scattering Experiment (J-PARC E40 experiment) . . .	13
2.2.1	Measurement method of “ $\Delta E$ method” . . . . .	17
2.3	Requirements for CATCH system . . . . .	20
2.4	CATCH system . . . . .	27
<b>3</b>	<b>Structure and Development of CATCH system</b>	<b>32</b>
3.1	Cylindrical Fiber Tracker . . . . .	32
3.1.1	Features of a Fiber Tracker . . . . .	32
3.1.2	Specification and Structure . . . . .	33
3.1.3	Fabrication . . . . .	36
3.2	BGO Calorimeter . . . . .	42
3.3	PiID counter . . . . .	44
3.4	MPPC readout system with EASIROC board . . . . .	45
3.5	Data acquisition system and Data set of CATCH system . . . . .	46
3.6	The process to the application of CATCH system . . . . .	47
<b>4</b>	<b>Commissioning of Cylindrical Fiber Tracker</b>	<b>48</b>
4.1	Cosmic ray measurement with CFT . . . . .	48
4.2	Measured data . . . . .	51
4.2.1	CFT ADC . . . . .	51

4.2.2	CFT TDC . . . . .	52
4.2.3	CFT hit pattern . . . . .	54
4.3	CFT Fiber position correction . . . . .	56
4.3.1	CFT Tracking procedure . . . . .	57
4.3.2	Position correction in Straight layers . . . . .	59
4.3.3	Spiral layer position correction . . . . .	66
4.3.4	Results of position correction . . . . .	70
4.4	Angular resolution for cosmic ray . . . . .	71
4.5	Operation procedure . . . . .	74
<b>5</b>	<b>Performance evaluation of CATCH by a beam experiment</b>	<b>75</b>
5.1	Overview . . . . .	75
5.2	Experimental setup and conditions . . . . .	75
5.3	Analysis and evaluation procedure . . . . .	77
5.4	CFT tracking performance . . . . .	78
5.4.1	angular resolution . . . . .	78
5.4.2	CFT Time resolution . . . . .	82
5.5	Energy calibration . . . . .	88
5.6	Energy calibration of BGO calorimeter . . . . .	88
5.7	Energy calibration of CFT . . . . .	96
5.7.1	MPPC output normalization . . . . .	96
5.7.2	CFT straight layer . . . . .	98
5.7.3	CFT spiral layer . . . . .	102
5.8	$\Delta E$ distribution . . . . .	106
5.9	Cross section of $pp$ and $pC$ scattering . . . . .	110
5.9.1	Event identification from $\Delta E$ distribution . . . . .	110
5.9.2	Proton detection efficiency of CATCH system . . . . .	111
5.9.3	Probability of proton penetration CFT . . . . .	112
5.9.4	Probability that CFT reconstructs trajectory of proton .	116
5.9.5	Probability that BGO calorimeters measure the energy correctly . . . . .	123
5.9.6	Result of cross section . . . . .	126
5.9.7	The target position dependence of the derivation of the cross section . . . . .	135

<b>6</b>	<b>Estimation for the <math>\Sigma p</math> scattering experiment</b>	<b>140</b>
6.1	Evaluation results of CATCH performances . . . . .	140
6.2	$\Delta E$ resolution . . . . .	141
6.2.1	The spread of the energy calculated from recoil angle . .	141
6.2.2	The spread of the energy measured by CFT and BGO calorimeter . . . . .	143
6.2.3	The spread of $\Delta E$ . . . . .	144
<b>7</b>	<b>Summary</b>	<b>147</b>

# List of Figures

1.1	Baryon octet . . . . .	3
1.2	$B_8 B_8$ potentials expected from lattice QCD simulation . . . . .	6
1.3	Model dependence of cross section of $\Sigma p$ scattering . . . . .	9
2.1	“Imaging method” to identify $\Sigma p$ scattering . . . . .	12
2.2	The result of past experiment . . . . .	13
2.3	Setup of J-PARC K1.8 beamline for E40 experiment . . . . .	15
2.4	Schema of $\Sigma$ production . . . . .	18
2.5	Schema of $\Sigma p$ scattering event measurement . . . . .	19
2.6	$\Delta E$ distribution simulated for $\Sigma p$ scattering experiment . . . . .	21
2.7	Flow chart of the simulation of the $\Sigma p$ scattering . . . . .	22
2.8	$\Delta E$ distribution simulated for $\Sigma p$ scattering experiment . . . . .	23
2.9	Required angular resolution of CFT . . . . .	25
2.10	CATCH . . . . .	28
2.11	Target size and position . . . . .	29
2.12	Amount of material of CATCH system . . . . .	30
3.1	Principle of Fiber Detector . . . . .	33
3.2	Structure of fiber arrangement . . . . .	34
3.3	Three dimensional position from two fiber structures . . . . .	35
3.4	CFT straight layer structure . . . . .	36
3.5	CFT straight layer 4 structure . . . . .	38
3.6	Picture of straight layer frame (reflection side) . . . . .	39
3.7	Picture of straight layer frame (readout side) . . . . .	39
3.8	Fabrication method of CFT spiral layer . . . . .	40
3.9	Picture of CFT spiral layer in fabrication . . . . .	41
3.10	Picture of a BGO crystal . . . . .	42
3.11	BGO readout circuit . . . . .	43

3.12	BGOsignal . . . . .	44
3.13	DAQ system . . . . .	46
4.1	Trigger logic . . . . .	49
4.2	Event Display . . . . .	50
4.3	CFT ADC distribution for cosmic ray . . . . .	52
4.4	CFT TDC distribution for cosmic ray . . . . .	53
4.5	CFT ctime distribution . . . . .	54
4.6	Hit pattern distribution of CFT straight layer for cosmic ray . . . . .	55
4.7	Hit pattern distribution of CFT spiral layer for cosmic ray . . . . .	55
4.8	Fiber position correction by using cosmic lay penetration . . . . .	57
4.9	CFT Tracking procedure . . . . .	58
4.10	CFT Tracking procedure with fiber position correction . . . . .	59
4.11	Definition of $d\phi$ . . . . .	60
4.12	$z$ dependence of straight layer fiber deviation . . . . .	61
4.13	Illustration of deviation of fiber position . . . . .	62
4.14	Fiber segment dependence of fiber position deviation . . . . .	63
4.15	$z$ dependence of fiber deviation after correction . . . . .	64
4.16	$\phi$ dependence of fiber deviation . . . . .	65
4.17	Residual distribution of $d\phi$ in CFT straight layer . . . . .	66
4.18	fiber deviation of spiral layers . . . . .	67
4.19	$\phi$ dependence of fiber deviation of spiral layers . . . . .	68
4.20	$z$ dependence of fiber deviation of spiral layers . . . . .	69
4.21	Residual distribution of $d\phi$ in CFT straight layer . . . . .	69
4.22	$\chi^2$ distribution of CFT fitting . . . . .	70
4.23	Tracked $\theta$ distribution for cosmic ray . . . . .	72
4.24	$\theta_1 + \theta_2$ for cosmic ray . . . . .	73
5.1	Setup for $pp$ and $pC$ scattering experiment . . . . .	76
5.2	Analysis procedure to derive the scattering cross section with CATCH . . . . .	77
5.3	$\theta$ distribution which . . . . .	79
5.4	Schema of summation of 2 $\theta$ from $pp$ scattering . . . . .	79
5.5	Summation of measured 2 $\theta$ from $pp$ scattering . . . . .	80
5.6	Image of the shift of the CFT tracking . . . . .	81
5.7	Time distribution of protons detected by CFT . . . . .	83

5.8	Path difference between straight and spiral layer of CFT . . . . .	84
5.9	z position dependence of CFT time distribution . . . . .	85
5.10	CFT time distribution corrected by z position dependence . . . . .	86
5.11	CFT ctime distribution corrected from z position dependence . . . . .	86
5.12	CFT time resolution . . . . .	87
5.13	Waveform analysis for BGO calorimeters . . . . .	88
5.14	Correlation between BGO wave height and $\theta$ . . . . .	89
5.15	Request condition to select $pp$ scattering . . . . .	90
5.16	Simulated energy deposit in BGO calorimeter from $pp$ and $pC$ scattering . . . . .	91
5.17	Selected BGO wave height for $pp$ and $pC$ scattering . . . . .	91
5.18	Correlation between the measured BGO wave height and the simulated energy deposit . . . . .	92
5.19	Correlation between BGO energy and scattering angle $\theta$ after calibration . . . . .	93
5.20	$\theta$ dependence of the BGO energy resolution . . . . .	94
5.21	BGO energy selected in scattering angular range of $25 \pm 2.5$ degrees . . . . .	94
5.22	CFT ADC normalization . . . . .	97
5.23	Normalized CFT ADC . . . . .	97
5.24	Correlation between $\theta$ and energy deposit in CFT in simulation . . . . .	98
5.25	Correlation between $\theta$ and photon yield in CFT . . . . .	99
5.26	Correlation between the number of detected photons and simulated energy deposit in CFT . . . . .	100
5.27	Saturation curve of MPPC output obtained from straight layer . . . . .	102
5.28	Correlation between $\theta$ and photon yield in CFT spiral layer . . . . .	103
5.29	Cross sectional shape of the fiber section on the plane of the scattered proton. . . . .	103
5.30	Energy calibration curve for the CFT spiral layer . . . . .	104
5.31	Measured energy spread of CFT . . . . .	105
5.32	Scattering plot of scattering angle $\theta$ and energy of $p'$ . . . . .	107
5.33	Correlation between $\Delta E$ and $\theta$ selected . . . . .	108
5.34	$\Delta E$ distribution of $p'$ from $pC$ scattering . . . . .	108
5.35	$\Delta E$ spread . . . . .	109
5.36	Event number identified from $\Delta E$ distribution . . . . .	110

5.37	Flow chart of measuring $p'$	111
5.38	Path length in fibers of a CFT spiral layer	113
5.39	Probability that proton from $pp$ scattering penetrate CFT	114
5.40	Probability that $p'$ from $pC$ scattering penetrates CFT	114
5.41	Probability that the scattered proton from $pC$ scattering penetrates CFT	115
5.42	Analysis method for obtaining CFT detection efficiency	116
5.43	$\phi$ dependence of detection efficiency of CFT straight layers	117
5.44	Detection and Tracking efficiency of CFT straight layers	118
5.45	Detection and Tracking efficiency of CFT spiral layers	119
5.46	$\theta$ dependence of Detection and Tracking efficiency of CFT straight layers	119
5.47	$\theta$ dependence of Detection and Tracking efficiency of CFT spiral layers	120
5.48	Fiber arrangement structure of CFT Spiral layer	120
5.49	Efficiency of CFT tracking	121
5.50	Correlation between BGO Energy and $\theta$	122
5.51	CFT tracking efficiency	123
5.52	Probability that BGO calorimeters measure the energy of $p'$ from $pp$ scattering correctly	124
5.53	Misleading BGO efficiency for $pC$ scattering	125
5.54	Application of BGO efficiency of $pp$ scattering to $pC$ scattering	126
5.55	Efficiency that CATCH system detect protons	127
5.56	Relative cross section of $pp$ and $pC$ scattering	128
5.57	Comparison between the measured relative differential cross section of $pp$ scattering	129
5.58	The differential cross section of the $pC$ scattering obtained from a past experiment	131
5.59	$\Delta E$ distribution of $pC$ scattering at three points of $\theta$	132
5.60	Two kinds of fitting method of $\Delta E$ distribution of $pC$ scattering	133
5.61	Difference between two kinds of fitting method for $pC$ scattering	134
5.62	Target position and Combinations of $\theta$ and $z$ position	135
5.63	Efficiency of CATCH for three target $z$ position	136
5.64	Target position and Cross Section	137
5.65	Systematic error of the cross section	139

6.1	Calculated energy of recoil protons from $\Sigma p$ scattering . . . . .	142
6.2	Spread of the calculated energy of recoil proton in $\Sigma p$ scattering	143
6.3	Spread of the measured energy of recoil proton in $\Sigma p$ scattering	144
6.4	$\Delta E$ resolution . . . . .	145

# List of Tables

1.1	The combinations of the irreducible multiplets in flavor SU(3) . . . . .	5
2.1	Specifications of the spectrometer systems . . . . .	16
2.2	The estimated yield of the tagged number of the produced $\Sigma$ beam . . . . .	17
2.3	$\Delta E$ resolution dependence of the accuracy of the cross section . . . . .	24
2.4	Required performances for CATCH . . . . .	24
2.5	Amount of material in the CATCH system . . . . .	30
3.1	Measurement data set of CATCH system . . . . .	46
4.1	Measurement condition for cosmic ray. . . . .	51
4.2	CFT missing channels . . . . .	56
4.3	The spreads of $d\phi$ and $dz$ of CFT tracking . . . . .	71
5.1	Experimental condition of CATCH test measuring protons . . . . .	76
5.2	Time spread of CFT TDC for tracked protons . . . . .	83
5.3	Ratio of the flight path of light between the straight and spiral layers . . . . .	84
5.4	Summary of CFT time resolution (rms) for each layer in the units of ns . . . . .	87
5.5	Simulated energy spread of the BGO calorimeter . . . . .	95
6.1	Summary of the evaluated performances of the CATCH system . . . . .	140

# Chapter 1

## Introduction

In this thesis, I explain the development and the performance evaluation of a new detector system “CATCH”, which was designed for a scattering experiment between a  $\Sigma$  hyperon and a proton (J-PARC E40). The CATCH system was designed to have a cylindrical shape covering a target and to measure a trajectory and an energy of emitted protons from the target in order to identify the scattering events kinematically. A particular feature of this detector system is that the CATCH is able to detect multi particles at the same time with an angular resolution of 2 degrees ( $\sigma$ ) and a large angular acceptance. Furthermore, a time response is so good to be operated under a high singles rate environment of about 2 MHz. The accuracy of the differential cross section of the scattering reaction is required to be better than  $\pm 10\%$ . By realizing the CATCH system, a comparable experimental data of the scattering cross section with some theoretical models will be taken for the first time to study the baryon-baryon interaction.

This detector system is considered to be applied to other experiments. Actually, CATCH was tested by obtaining the differential cross sections of  $pp$  and  $pC$  scatterings by measuring protons emitted from the scattering reactions. We also performed a  $pd$  scattering experiment, and it was also confirmed that it is possible to measure deuterons with CATCH. It is also effective to apply to reactions such as break-up reactions, which require the detection of multiple particles at the same time. For example, by detecting all emitted protons from the  $pd$  scattering or the  ${}^3\text{He}$  break-up reaction, these reaction events can be identified. In this way, there is a possibility to realize various new experiments not only the hyperon-proton scattering experiment.

However, this thesis focuses on the  $\Sigma p$  scattering experiment as the main purpose of CATCH system. In the following, I explain the physics motivation of the  $\Sigma p$  scattering experiment. The required performances of the CATCH system is also discussed based on the physics motivation.

## 1.1 Baryon-Baryon interaction

The nuclear force has been studied experimentally by proton-proton and proton-neutron scattering. It works as an attractive force in the long range region between the two nucleons, that is understood well by meson exchange models. On the other hand, a strongly repulsive core exists in the short distance region less than 1 fm. With a miraculous balance between the attractive force and the repulsive force, the nucleus exists stably and forms all the matter in nature. However, our understanding of the nuclear force is quite unsatisfactory yet especially in the short range. The repulsive core is treated phenomenologically in conventional meson exchange models. In such a short range region, it is expected that dynamics of quarks and gluons play an important role. Therefore, by introducing a new flavor of quarks, which is a strange quark in this study, it is expected to provide a clue to approach this problem.

The nucleons, the lightest spin 1/2 baryons, made of  $u$  and  $d$  quarks, can be extended to the baryon octet ( $B_8$ ) by introducing  $s$  quarks as shown in Figure 1.1. In order to understand the nuclear force, it is important to investigate the baryon-baryon ( $B_8 B_8$ ) interactions.

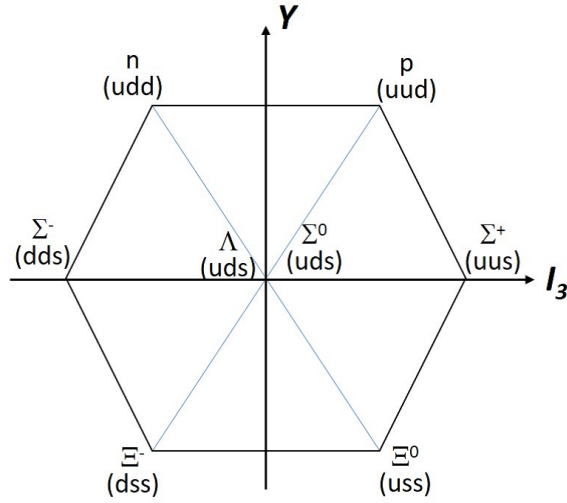


Figure 1.1: Nucleons made of  $u$  and  $d$  quarks with spin  $1/2$  are extended to the baryon octet by introducing  $s$  quarks.  $I_3$  and  $Y$  represent  $z$  component of isospin and hyper charge of the baryon, respectively.

The interactions between the octet baryons ( $B_8 B_8$ ) have been studied theoretically by two different types of theoretical models. One is the One Boson Exchange (OBE) models such as Nijmegen OBEP models [1] based on meson exchange picture between baryons, and the other is quark based models such as Quark Cluster Model (QCM) [2]. The Nijmegen group developed OBEP models that extend nuclear force to  $B_8 B_8$  interactions based on the flavor  $SU(3)$  symmetry with the phenomenological repulsive core potential. The QCM was developed from a QCD inspired model that takes into account the effect of one gluon exchange between constituent quarks in the confined potential.

The  $B_8 B_8$  interactions are classified by the isospin irreducible representations with the flavor  $SU(3)$  group. In the case of the two nucleon system, the interactions are classified into the isospin triplet and singlet as followings,

$$2 \otimes 2 = 3 \oplus 1. \quad (1.1)$$

Here, 2 means the isospin doublet of nucleon (proton and neutron), 3 and 1 correspond to the isospin triplet and singlet, respectively. Due to the isospin symmetry, it is considered that the same interaction works in the same multiplets.

As an extension of this expression, the interactions between two members of

the baryon octet ( $B_8 B_8$ ) are classified as followings,

$$8 \otimes 8 = 27 \oplus 8_s \oplus 1 \oplus 10^* \oplus 10 \oplus 8_a. \quad (1.2)$$

Here, the number means the number of members of the multiplet, and “s” and “a” mean symmetric and anti-symmetric under exchanging of two baryons. The components belonging to the common multiplet should have the same baryon-baryon interaction. It has entirely different structure between the symmetric and antisymmetric cases under a flavor exchange of two baryons. Here, the first three multiplets 27,  $8_s$ , and 1 are symmetric and the others are anti-symmetric configurations.

The same interaction is predicted in the common multiplets. This classification is expected to show various features in the interaction at the short range region. In addition to the interactions between nucleons, which is classified to (27) and ( $10^*$ ), the newly appeared interactions are predicted to show interesting characteristics especially in the short range region such as a quite strong repulsive core in ( $8_s$ ) and (10), and an attractive core in (1).

Especially among the  $\Sigma N$  interactions, the  $\Sigma^+ p$  channel with spin = 1 is very interesting because it is expected to be very repulsive in the quark picture. Since  $\Sigma^+$  has an isospin of 1, the spins of the two  $u$  quarks of the constituent quarks ( $uus$ ) have the same direction. For the  $\Sigma^+ p$  channel with a total spin of 1, the probability that one of the two  $u$  quarks in  $\Sigma^+$  and one of the two  $u$  quarks in the proton have the same spin and color becomes very large. This causes the strong repulsive force by Pauli principle in the quark level, and the repulsive core becomes very large.

This “quark Pauli effect” is considered to be one of the origins of the repulsive core in the  $NN$  interaction. However, it has not been confirmed experimentally yet.

The interaction between two baryons are represented by combinations of these multiplets expressed in Equation (1.2). The combinations corresponding to the systems of  $NN$ ,  $\Lambda N$  and  $\Sigma N$  in the isospin basis are summarized in Table 1.1.

Table 1.1: The combinations of the irreducible multiplets of  $BB$  interactions in flavor  $SU(3)$  for  $NN$ ,  $\Lambda N$  and  $\Sigma N$  in the isospin basis

BB(I)	flavor symmetric	flavor anti-symmetric
NN (I=0)	-	(10*)
NN (I=1)	(27)	-
$\Lambda N$ (I=1/2)	$\frac{1}{\sqrt{10}}\{(8_s) + 3(27)\}$	$\frac{1}{\sqrt{2}}\{-(8_a) + (10^*)\}$
$\Sigma N$ (I=1/2)	$\frac{1}{\sqrt{10}}\{3(8_s) - (27)\}$	$\frac{1}{\sqrt{2}}\{(8_a) + (10^*)\}$
$\Sigma N$ (I=3/2)	(27)	(10)

The interactions between nucleons are expressed by multiplets of (27) and (10\*) corresponding to the flavor symmetric and anti-symmetric channel, respectively. The same multiplets of (27) appears in the several ( $^1S_0$ ) states of  $NN$ (I=1),  $\Sigma N$ (I=3/2),  $\Sigma\Sigma$ (I= 2),  $\Xi\Sigma$ (I=3/2) and  $\Xi\Xi$ (I=1).

In the strangeness  $S = -1$  sector, the  $\Lambda N$  interaction is intensively studied by the spectroscopy of  $\Lambda$  hypernuclei [3]. Information on the two body  $\Lambda N$  interaction can be extracted from the level structure of  $\Lambda$  hypernuclei with the G-matrix calculation [4]. On the other hand, knowledge of the  $\Sigma N$  interaction is quite limited because  $\Sigma$  hypernuclei except for  $^4_{\Sigma}\text{He}$  [5] are not observed. In such a situation, in order to study the overview of the  $BB$  interaction, the  $\Sigma N$  system plays an important role.

The  $\Sigma N$  interaction is expected to be quite dependent on the configuration of the isospin and spin. At first, the  $\Sigma N$ (I=1/2) channel, two spin states contain some multiplets. These states are expected to be weakly repulsive and weakly attractive.

The  $\Sigma N$  (I = 3/2) is a special channel for study of the repulsive core due to the quark Pauli effect. This channel is simply described by two multiplets. The spin singlet state corresponding to the flavor symmetric state belongs to the (27) multiplet, which is the same as the  $NN$ (I = 1) interaction as described above. Therefore, the contribution of this channel can be estimated from the study of the rich data of  $NN$  scattering experiments. The spin triplet state corresponding to the flavor anti-symmetric state belongs to the (10) multiplet, which is the almost Pauli forbidden state. Therefore, this channel is expected to reveal the repulsive force due to the quark Pauli effect.

Recently, a new method to extract the  $B_8B_8$  potentials in the coordinate space from lattice QCD simulations [6] has been proposed and applied to the

$NN$  and  $YN$  ( $Y$  represents a hyperon that includes  $s$  quarks as constituent quarks) systems. Figure 1.2 show the six independent  $B_8B_8$  potentials classified in Equation (1.2) calculated by a lattice QCD simulation. The results of the simulations at  $m_\pi = 1014$  MeV (red bars) and  $m_\pi = 835$  MeV (green bars) are shown in this figure.

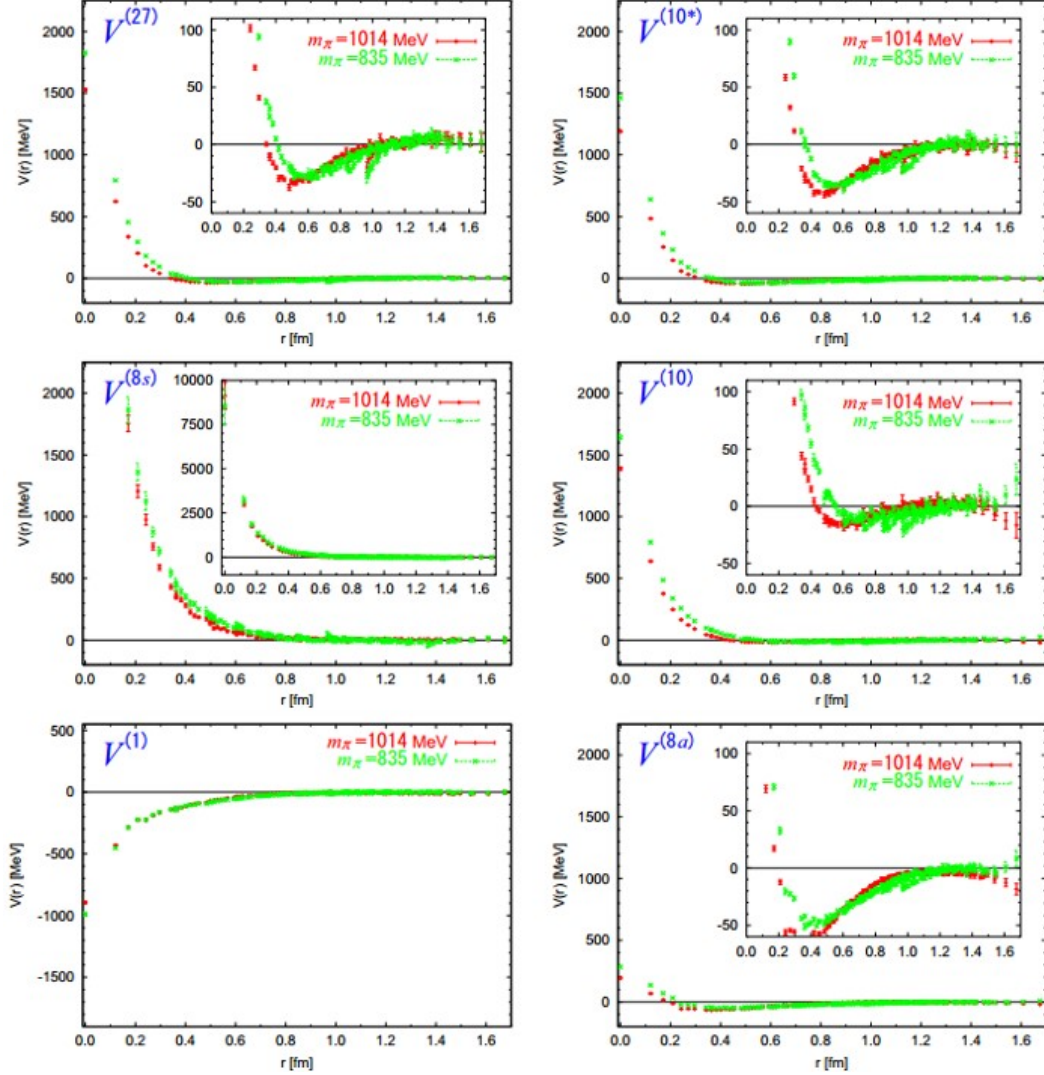


Figure 1.2: Six independent  $B_8B_8$  potentials classified in the Equation (1.2) calculated by a lattice QCD simulation at  $m_\pi = 1014$  MeV (red bars) and  $m_\pi = 835$  MeV (green bars) [6].

The lattice QCD simulation has also suggested that the repulsive core of  $\Sigma^+p$  is large. By confirming the actual behavior experimentally and comparing it

with these predictions, we can promote understanding of the  $BB$  interaction at the short range.

## 1.2 $\Sigma N$ interaction and scattering cross section

As described in the previous section, in order to study the  $BB$  interaction systematically, the  $\Sigma N$  channel is quite important. We will measure the following three reactions, that is, the  $\Sigma^+ p$  and  $\Sigma^- p$  elastic scatterings, and the  $\Sigma^- p \rightarrow \Lambda n$  reaction.

The strength of the repulsive core contributes to the phase shift of the scattering reaction and consequently affects the scattering cross section.

The phase shift can be obtained experimentally from the differential cross section of the  $\Sigma^+ p$  scattering. The differential cross section is expressed by partial wave expansion with the orbital angular momentum  $l$  and the phase shift  $\delta_l$ . Here, the Legendre function  $P_l(\cos\theta)$  become 0 at  $\theta = 90$  degrees for an odd number  $l$ . At the scattering angle of  $\theta = 90$  degrees, the scattering cross section is approximated by the following equation,

$$\frac{d\sigma}{d\Omega}(90\text{degrees}) = \frac{1}{4} \frac{1}{k^2} \sin^2 \delta_{1S_0} + \frac{3}{4} \frac{1}{k^2} \sin^2 \delta_{3S_1} + (\text{higher } l \text{ wave}). \quad (1.3)$$

Because the same interaction works in the same isospin multiplets in the flavor  $SU(3)$  symmetry, the contribution of  $^1S_0$  can be estimated from the rich experimental data of  $NN$  scattering, which contains the same multiplet of (27). Even taking into account the breaking of the flavor  $SU(3)$ , the difference between the phase shifts of each channel in the multiplet of (27) is estimated to be small from Ref. [7].

The contributions of higher  $l$  waves are expected to be small and can be well estimated as described in Ref. [7].

The momentum dependence of the cross section is also important to study the size of the repulsive core. Because the higher momentum scattering is influenced by the interaction between the two baryons in the shorter range region, the phase shift should be larger depending on the size of the repulsive core. The  $\frac{d\sigma}{d\Omega}(90\text{degrees})$  in the momentum region of 400-700 MeV/c is dominated by the  $^3S_1$  because  $\delta_{1S_0}$  is small in this momentum region [7].

Figures 1.3 shows the expected results of the cross sections of the  $\Sigma p$  scattering for each model for the  $BB$  interaction. The  $\Sigma^+ p$  scattering cross sections in

the momentum region of 0.5-0.6 GeV/c are predicted by the OBEP (Nijmegen Soft Core) models, the quark cluster (RGM FSS) models and the Chiral EFT model [8] as shown in the top of Figure 1.3. The predicted values are different due to their different treatment of the repulsion core. The differential cross sections of the  $\Sigma^-p$  scattering and the  $\Sigma^-p \rightarrow \Lambda n$  conversion are also shown in the middle and bottom of Figure 1.3, respectively.

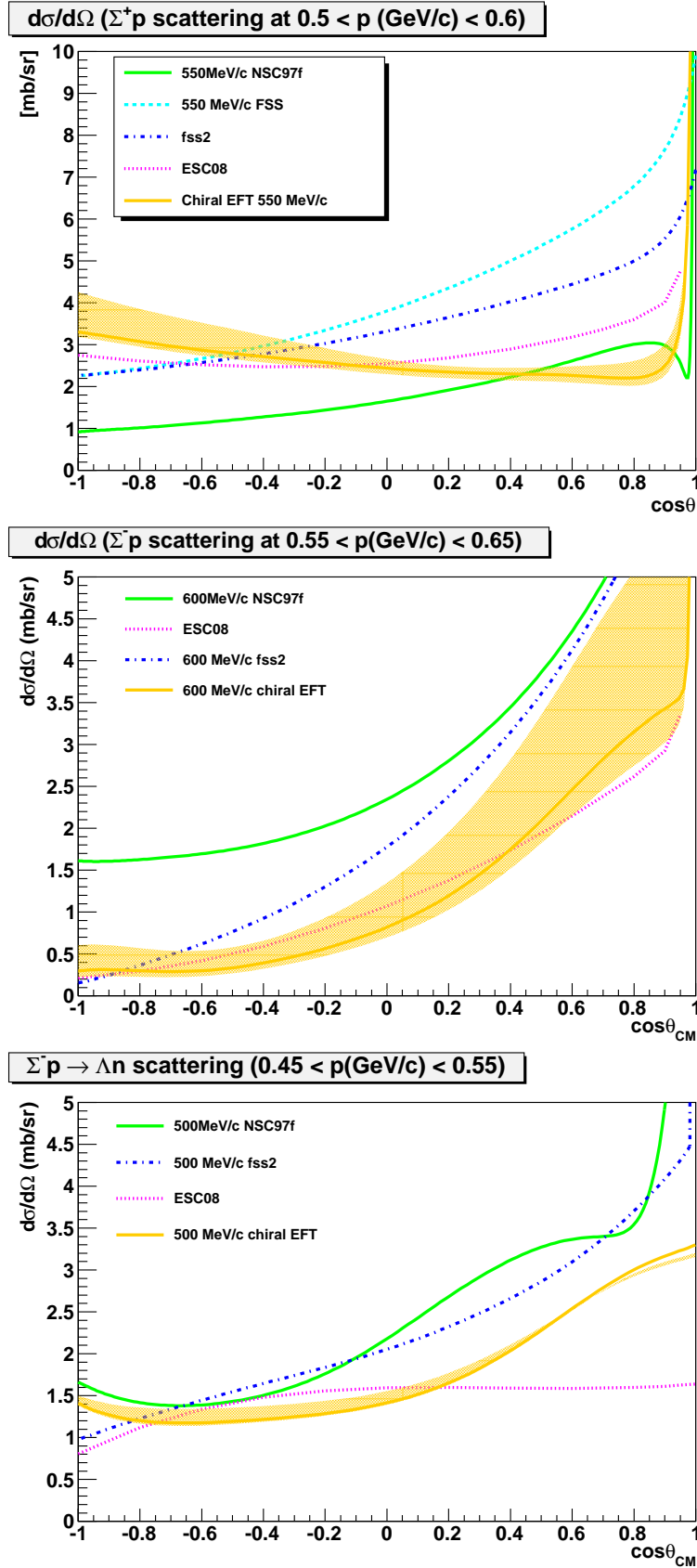


Figure 1.3:

The expected differential cross sections of the  $\Sigma^+p$  (Top) and the  $\Sigma^-p$  (Middle) scatterings and  $\Sigma^-p \rightarrow \Lambda n$  conversion (Bottom). These cross sections were predicted by the OBEP (Nijmegen Soft Core) models, the quark cluster (RGM FSS) models and the Chiral EFT model [8].

Although the  $\Sigma^-p$  ( isospin  $I = \frac{1}{2}$ ) channel is strongly affected by the quark Pauli effect, its contribution is smaller than in the case of the  $\Sigma^+p$  (spin = 1) channel in the  $\Sigma^+p$  scattering. Investigation of the  $\Sigma^-p$  elastic scattering and the reaction of  $\Sigma^- + p \rightarrow \Lambda + n$  also contributes to understanding of the  $\Sigma N$  interaction that has not yet been investigated quantitatively.

From the above reasons, we are planning to perform a  $\Sigma p$  scattering experiments in order to quantitatively determine the strength of the repulsive force and to verify the Pauli effect in the quark level by measuring the differential sections of the  $\Sigma p$  scattering. We aim to measure  $\frac{d\sigma}{d\Omega}(90^\circ)$  within a 10% statistical error and extract the  $\delta_{3S_1}$  value in order to discriminate the theoretical models. For this purpose, the scattering experiment with high statistics is necessary.

## Chapter 2

# A new $\Sigma p$ scattering experiment and requirements for CATCH system

The  $YN$  interactions have been studied through structure of hypernuclei (nuclei including hyperons). Especially, spectroscopic studies of  $\Lambda$  hypernuclei have been intensively performed with a high energy resolution. Theoretical models of  $BB$  interactions have been constructed to reproduce the accumulated experimental data with the G-matrix approach. However, it is not straightforward to extract information on the two-body  $BB$  interaction in free space from complex multi-baryon structure. It is true that there still exists uncertainty even for the  $\Lambda N$  interaction. For other  $YN$  interactions, our knowledge is quite limited. Especially, because a  $\Sigma$  particle is not bound as a hypernucleus except for  ${}^4_{\Lambda}\text{He}$ , the  $\Sigma p$  scattering experiment is a unique method to extract information on the  $\Sigma N$  interaction.

### 2.1 Past Experiment

Hyperon-nucleon scattering experiments were experimentally difficult due to the short lifetimes of hyperons ( $\sim 10^{-10}$  s). In the past,  $\Sigma p$  scattering experiments were performed using bubble chambers [9] or active targets made of scintillation fibers [10][11][12]. Both used "imaging method" in which scattering events are identified from image data of trajectories of all particles in the scattering events. Figure 2.1 shows a typical image data [10] in the two different planes,  $u$ - $z$  plane and  $v$ - $z$  plane, which was identified as a  $\Sigma^+ p$  elastic scattering event. All particles related to the scattering reaction should be detected for the event identification in this method.

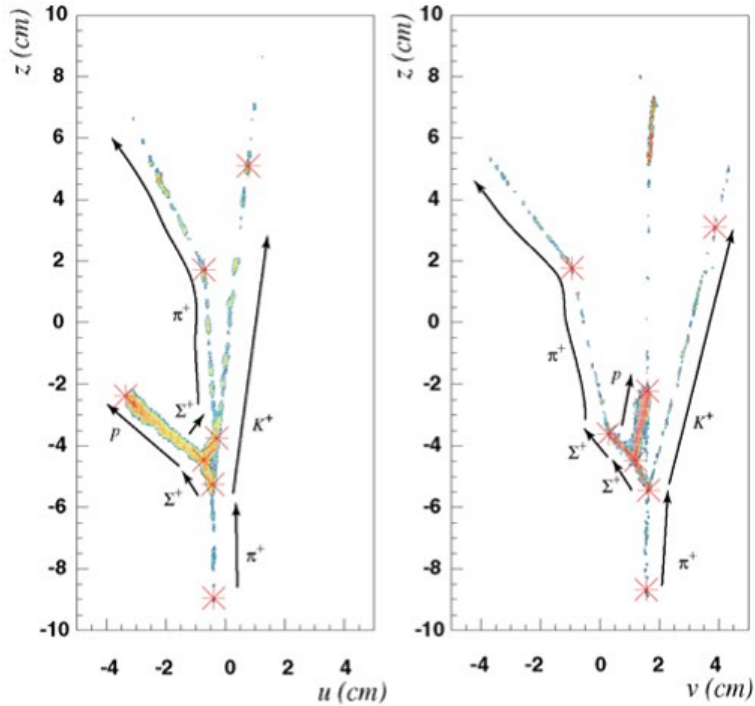


Figure 2.1: Typical image data in the two different planes,  $u$ - $z$  plane and  $v$ - $z$  plane, which was identified as a  $\Sigma^+p$  elastic scattering event [10]. All particles related to the scattering reaction should be detected for the event identification in this method.

In the experiment using scintillation fibers at KEK-PS, there were some experimental difficulties as followings leading to low statistics of identified events,

- Low beam intensity necessary to operate the slow imaging detector,
- Decay of  $\Sigma$  particles before obtaining their trajectories,
- Quasi-free production of  $\Sigma$  particle on a carbon nucleus in the target.

The readout time as long as several  $10 \mu\text{s}$  was necessary for holding the image and thus the beam intensity was limited to about 200 kHz. Furthermore, if the  $\Sigma$  particle decayed before reaching a flight length long enough ( $\sim 5 \text{ mm}$ ) to identify the trajectory by the scintillation fibers, its trajectory could not be recognized. In addition, the experiment suffered from a background due to quasi-free  $\Sigma$  production on carbon nuclei in the scintillation fiber target. Such background contribution was not small. As a result, the number of identified  $\Sigma p$

scattering events remained of the order of 30 and the differential cross section was obtained [11] with large errors as shown in Figure 2.2.

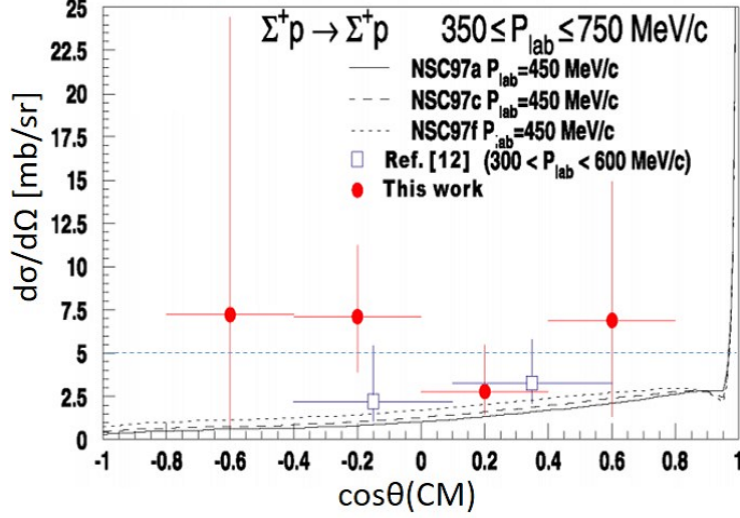


Figure 2.2: Differential cross section obtained in the past  $\Sigma p$  scattering experiment with the imaging method [11]. The result was obtained with large errors due to low statistics.

The data quality of the past experiments was not sufficient to set an experimental constraint to theoretical models.

## 2.2 New $\Sigma p$ scattering Experiment (J-PARC E40 experiment)

In order to overcome the low statistics of identified scattering events due to the experimental difficulties, we have introduced a new measurement method. The main features are summarized as following,

- New event identification method without detecting  $\Sigma$  particles directly,
- High intensity meson beam which becomes usable by introducing new detectors operational at high counting rates,
- Liquid hydrogen target as hyperon production and hyperon-proton scattering targets.

By introducing a new event identification method without detecting  $\Sigma$  particles directly, the difficulty in detecting the  $\Sigma$  particle can be solved. In the new method, “ $\Delta E$  method”, we identify the scattering events by solving kinematics from the measurement of only a  $\Sigma$  beam and a recoil proton.

By using a hydrogen target both for the  $\Sigma$  production and the  $\Sigma p$  scattering, both of the  $\Sigma$  production ( $\pi p \rightarrow K^+ \Sigma$ ) and  $\Sigma p$  scattering ( $\Sigma p \rightarrow \Sigma p$ ) become two-body reaction, which are free from the background events such as a quasi-free scattering on other nuclei. Therefore, by detecting the incident  $\pi$  beam, the scattered  $K^+$  and the recoil proton,  $\Sigma p$  scattering can be identified kinematically. This method enables us to use a high intensity  $\pi$  beam to produce a lot of  $\Sigma$  particles because we can use fast detectors only without taking image data by slow detectors..

We use a liquid hydrogen ( $\text{LH}_2$ ) target. The target is irradiated with a high intensity  $\pi$  beam and a  $\Sigma$  particle is produced. In order to reconstruct the momentum of the produced  $\Sigma$  particle, the spectrometers are installed at the upstream and at the downstream of the target to measure the momenta of  $\pi$  beam and scattered  $K^+$ . The recoil protons from  $\Sigma p$  scattering are detected by a detector system installed around the target. The detector system is called CATCH (Cylindrical Active Tracker and Calorimeter system for Hyperon proton scattering), which consists of a cylindrical tracking detector (Cylindrical Fiber Tracker, CFT) and a BGO calorimeter.

This experiment was approved as the J-PARC E40 experiment [13], and it is planned to be carried out at the J-PARC K1.8 beam line. The high intensity  $\pi$  beam of about 20 [M/spill] (the spill length is about 2 seconds) can be used at this beam line. In order to detect scattered  $K^+$  with a large acceptance, the KURAMA spectrometer will be used as the downstream spectrometer. Figure 2.3 shows the experimental setup of the K1.8 beam line and the KURAMA spectrometers and CATCH system around the  $\text{LH}_2$  target. The K1.8 spectrometer and the KURAMA spectrometer analyze the momenta of the incident  $\pi$  beam particle and the scattered  $K^+$ , respectively. CATCH detects the recoil proton emitted from  $\Sigma p$  scattering.

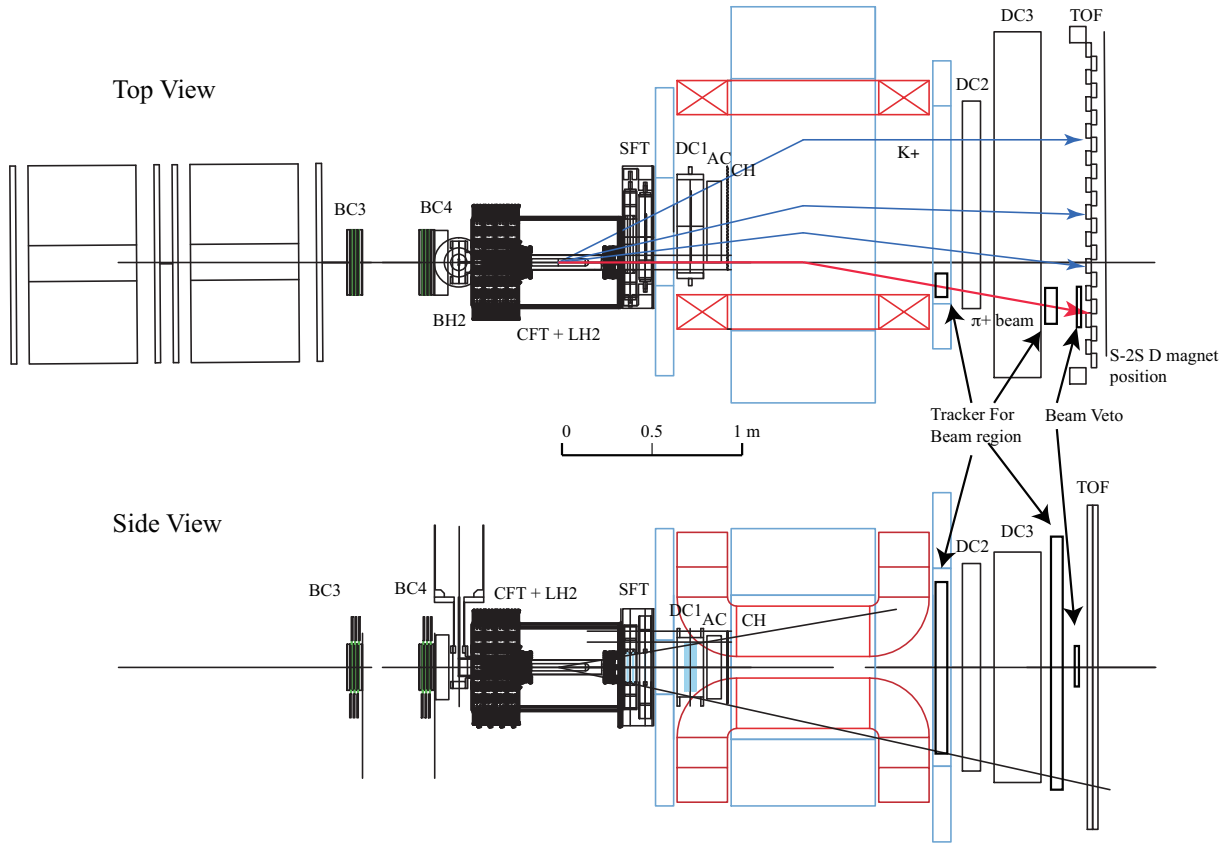


Figure 2.3: Experimental setup of the  $\Sigma p$  scattering experiment, J-PARC E40. The K1.8 spectrometer and the KURAMA spectrometer analyze the incident  $\pi$  beam particle and the scattered  $K^+$ , respectively. CATCH installed around the  $\text{LH}_2$  target detects the recoil proton emitted from  $\Sigma p$  scattering.

The angular acceptance of the KURAMA spectrometer for the scattered  $K^+$  is correlated with the momentum acceptance of the  $\Sigma$  beam. In order to tag  $\Sigma$  beam for a wide momentum region from 0.4 GeV/c to 0.7 GeV/c for the study of the repulsive core, the KURAMA spectrometer setup was modified to cover up to 20 degrees of the scattering angle for  $K^+$ . Specifications of the spectrometer system are summarized in Table 2.1.

Table 2.1: Specifications of the spectrometer systems

KURAMA spectrometer	
Momentum resolution of $\Sigma$ ( $\sigma_P/P$ )	$10^{-2}$
Angular resolution of $\Sigma$	$\sigma \sim 0.4$ degrees
Acceptance	280 mrad
Magnetic field	0.72 T
Angular acceptance	$\sim 20$ degrees
Flight length of $K^+$	3 m

In the KURAMA spectrometer, the flight length of the scattered  $K^+$  is 3 m. It is about a half for the SKS spectrometer, which was another candidate of the downstream spectrometer. Such a short flight length leads to a higher survival rates of  $K^+$ . The survival rates of  $K^+$  are estimated to be 65% and 59% for the  $\Sigma^+$  and  $\Sigma^-$  production, respectively.

By using these detector systems and setup, we estimated the yield of the tagged number of the produced  $\Sigma$  beam in this experiment [14] as shown in Table 2.2. We used the cross sections of the  $\Sigma^\pm$  production obtained from the past experiments [15][16].

Table 2.2: The estimated yield of the tagged number of the produced  $\Sigma$  beam

$\Sigma^-p$ scattering experiment	
Cross section of $\Sigma^-$ production	245 $\mu\text{b}$
$\pi^-$ beam intensity	$2 \times 10^7$ /spill (2 sec beam time in 6 sec cycle)
LH <sub>2</sub> target thickness	30 cm
KURAMA Acceptance	4.0%
Survival rate of $K^+$	59%
DAQ live time	70%
Analysis efficiency	70%
Tagged $\Sigma^-$ /spill	72 /spill
Tagged $\Sigma^-$ /day	$0.97 \times 10^6$
Accumulated Tagged $\Sigma^-$	$18 \times 10^6$ (20 days)
$\Sigma^+p$ scattering experiment	
Cross section of $\Sigma^+$ production	523 $\mu\text{b}$
$\pi^+$ beam intensity	$2 \times 10^7$ /spill (2 sec beam time in 6 sec cycle)
LH <sub>2</sub> target thickness	30 cm
KURAMA Acceptance	6.7%
Survival rate of $K^+$	65%
DAQ live time	70%
Analysis efficiency	70%
Tagged $\Sigma^+$ /spill	283 /spill
Tagged $\Sigma^+$ /day	$4.0 \times 10^6$
Accumulated Tagged $\Sigma^+$	$81 \times 10^6$ (20 days)

In addition to the spectrometer systems, we introduce a new method and a new detector system to detect the  $\Sigma p$  scattering events with an acceptance as large as possible.

### 2.2.1 Measurement method of “ $\Delta E$ method”

The setup of the experiment is roughly divided into two. One is the magnetic spectrometers systems which tag  $\Sigma$  production as shown in Fig. 2.3 and the other is the recoil proton detector system, CATCH, surrounding the target. From these two detector sets, we derive the  $\Delta E$  distribution which is used to identify scattering events.

- Measurement system for  $\Sigma$  production

The  $\pi$  beam is incident on the liquid hydrogen target and  $\Sigma$  particles are produced by the  $\pi^\pm + p \rightarrow \Sigma^\pm + K^+$  reaction as shown in Figure 2.4. The

beam is planned to be used at an intensity of 10 MHz with momenta of 1.32 and 1.4 GeV/c for  $\pi^-$  and  $\pi^+$  beam, respectively. The momentum vector of the incident  $\pi$  beam is measured by the beam line spectrometer with QQDQQ magnets ( the downstream part of the K1.8 beam line) placed upstream of the target. The momentum vector of scattered  $K^+$  is measured by the KURAMA spectrometer system. From the measured momenta of  $\pi$  beam and scattered  $K^+$ , the momentum vector of the produced  $\Sigma$  is reconstructed.

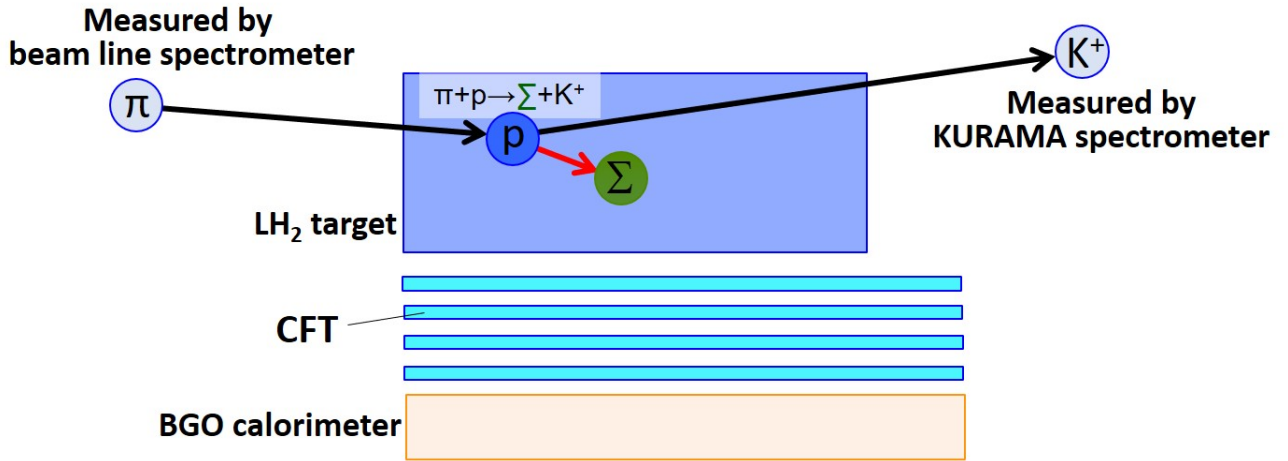


Figure 2.4: Schematic view of  $\Sigma$  production in the liquid hydrogen target.  $\Sigma$  particle is produced by the  $\pi^\pm + p \rightarrow \Sigma^\pm + K^+$  reaction. From the measured momenta of  $\pi$  beam and scattered  $K^+$  by the spectrometers, the momentum vector of the produced  $\Sigma$  is reconstructed.

- Measurement system for recoil proton

CATCH detects recoil protons and decay products from  $\Sigma$  decay emitted by  $\Sigma + p \rightarrow \Sigma' + p'$  and measures the direction and the kinetic energy of the recoil proton as shown in Figure 2.5. The momentum vector of the  $\Sigma$  beam is reconstructed from the spectrometer systems. By combining the incident direction of the  $\Sigma$  and the emission direction of the proton, we can obtain the scattering angle  $\theta$  of  $\Sigma p$  scattering.

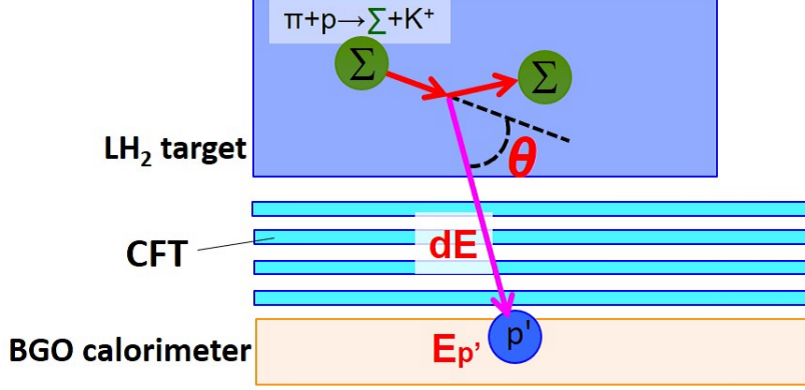


Figure 2.5: Schematic view of the detection of the recoil proton with CATCH. CATCH detects recoil protons and decay products from  $\Sigma$  decay emitted by  $\Sigma + p \rightarrow \Sigma' + p'$  and measures the direction and kinetic energy of the recoil proton.

In such a 2-body system of the elastic scattering, since the target particle is at rest, the energy of recoil proton ( $E_{p'calc}$ ) can be calculated kinematically from the kinetic energy of the  $\Sigma$  and the scattering angle of the recoil proton. In non-relativistic approximation,  $E_{p'calc}$  is represented by Equation 2.1,

$$E_{p'calc} = 4E_{\Sigma} \frac{m_{\Sigma} m_p}{(m_{\Sigma} + m_p)^2} \cos^2 \theta, \quad (2.1)$$

where  $E_{\Sigma}$  is the kinetic energy of the produced  $\Sigma$  beam, and  $m_{\Sigma}$  and  $m_p$  are the mass of  $\Sigma$  and  $p$ , respectively.  $\theta$  is the recoil angle (the angle between the incident  $\Sigma$  and the recoil proton).

From the above measurement, two types of  $E_{p'}$  are obtained as followings.

- $E_{p'measure}$ : The energy measured by CFT and BGO. The protons are stopped in the BGO calorimeter and the total kinetic energy is measured.
- $E_{p'calc}$ : The energy of proton calculated from  $\theta$  and the energy of the  $\Sigma$  beam.

Here,  $\Delta E$  is defined as a criterion to identify the  $\Sigma p$  scattering event as follows.

$$\Delta E = E_{p'calc} - E_{p'measure}. \quad (2.2)$$

The  $\Delta E$  value of  $\Sigma p$  scattering should become zero for  $\Sigma p$  scattering events, although due to the experimental resolution the  $\Delta E$  distribution has a certain width. On the other hand, for background events the  $\Delta E$  distribution should have no peak structure around zero.

In the  $\Sigma p$  scattering experiment, the following background events are expected.

a)  $\Sigma^+ p$  scattering

- Directly measuring the proton from  $\Sigma^+$  decay;  $\Sigma^+ \rightarrow p + \pi^0$
- Scattering with  $\Sigma$  decay products or beam  $\pi$ ;  $\Sigma^+ \rightarrow p + \pi^0, n + \pi^+$   
 $Np$  scattering:  $p + p \rightarrow p' + p'$  or  $n + p \rightarrow n' + p'$   
 $\pi p$  scattering:  $\pi + p \rightarrow \pi' + p'$

b)  $\Sigma^- p$  scattering

- Scattering with  $\Sigma$  decay products or beam  $\pi$ ;  $\Sigma^- \rightarrow n + \pi^-, n + p \rightarrow n' + p'$
- $\Sigma^0 n$  conversion

The resolution of  $\Delta E$  becomes important when counting the number of scattering events from the  $\Delta E$  distribution. If the  $\Delta E$  resolution is not sufficient, it causes a large statistical error in deriving the differential cross section of the  $\Sigma p$  scattering due to background events.

### 2.3 Requirements for CATCH system

A detector system for proton detection needs to be newly developed in order to realize such a new  $\Sigma p$  scattering experiment. Therefore, we introduced a new detector system called a Cylindrical Active Tracker and Calorimeter system for Hyperon-proton scattering ( “CATCH”). CATCH is designed to measure the trajectory and energy of the emitted proton in  $\Sigma p$  scattering events.

In this section, I estimated the required performances for CATCH system for the measurement of the  $\Sigma p$  scattering cross section with a sufficient accuracy to compare with the theoretical models. For example, in order to distinguish the predictions from fss2 and ESC08 models, with are blue and magenta lines in Figure 1.3 with the confidence level of  $3\sigma$ , the accuracy of the cross section is required to be better than 10% at 3 mb/sr.

Since the  $\Delta E$  resolution affects the number of background events under the peak in the  $\Delta E$  distribution as shown in Figure 2.6, the required  $\Delta E$  resolution can be estimated from the required statistical error in counting the number of peak events. A simulation of the  $\Sigma p$  scattering experiment was performed based on the known performance of the spectrometer system. By changing the  $\Delta E$  resolution and the assumed value of the cross section, the accuracy of deriving the cross section with the detector system was estimated.

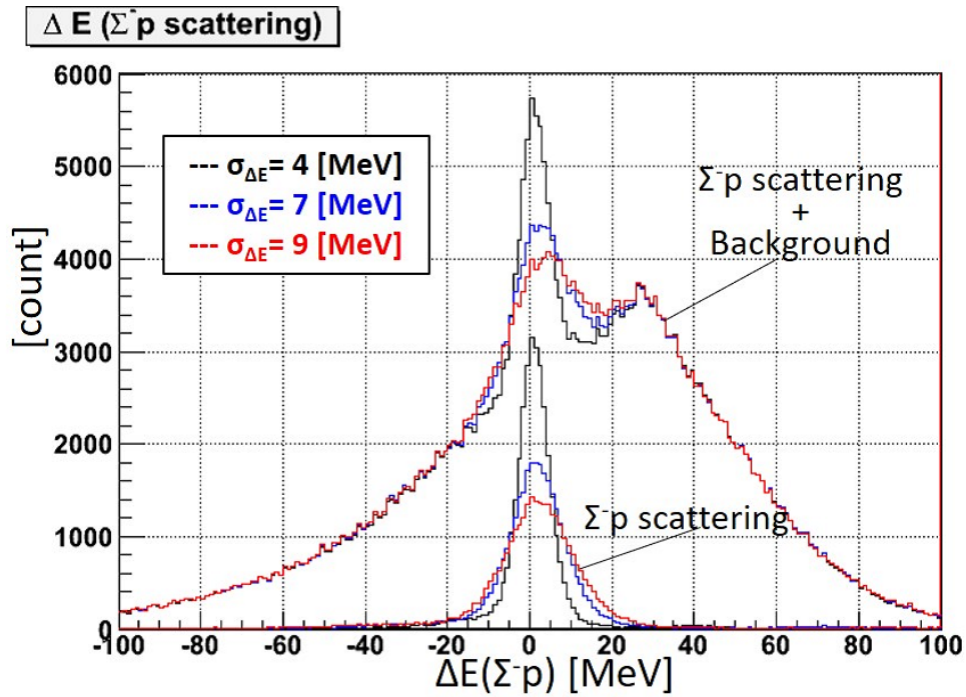


Figure 2.6: The  $\Delta E$  distributions obtained from the simulations of  $\Sigma^-p$  scatterings considering the different resolutions of  $\Delta E$  ( $\sigma_{\Delta E} = 4, 7, 9$  MeV).

The LH<sub>2</sub> target, the spectrometer system and the CATCH system were reproduced in this simulation. The flow chart of the simulation is shown in Figure 2.7. Generated  $\Sigma p$  scattering events were identified by the detector system.

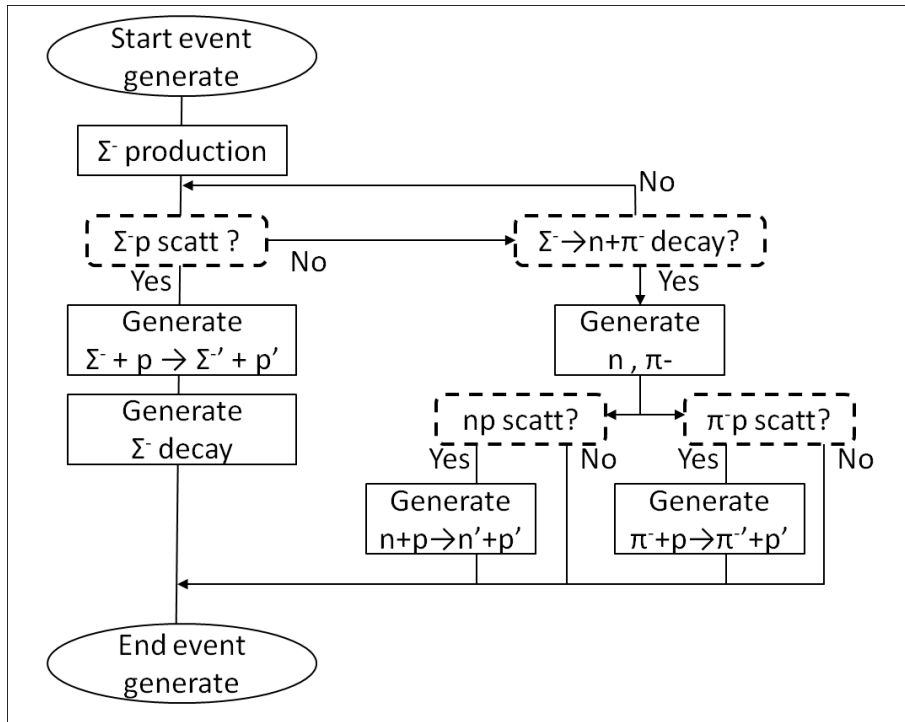


Figure 2.7: The flow chart of the simulation of the  $\Sigma p$  scattering experiment at J-PARC.

Figure 2.8 show the simulated result of the cross sections (dots) and those from the theoretical models (lines). In this simulation, the differential cross section is assumed to be 2.4 mb/sr for the  $\Sigma^+ p$  scattering, and 2.4, 1.2 and 0.6 mb/sr for the  $\Sigma^- p$  scatterings. The difference between the assumed cross section and the derived value can be treated as a systematic error in this experiment. As the performance of CATCH system, the  $\Delta E$  resolution is assumed to be  $\sigma_{\Delta E} = 5$  MeV in this figure.

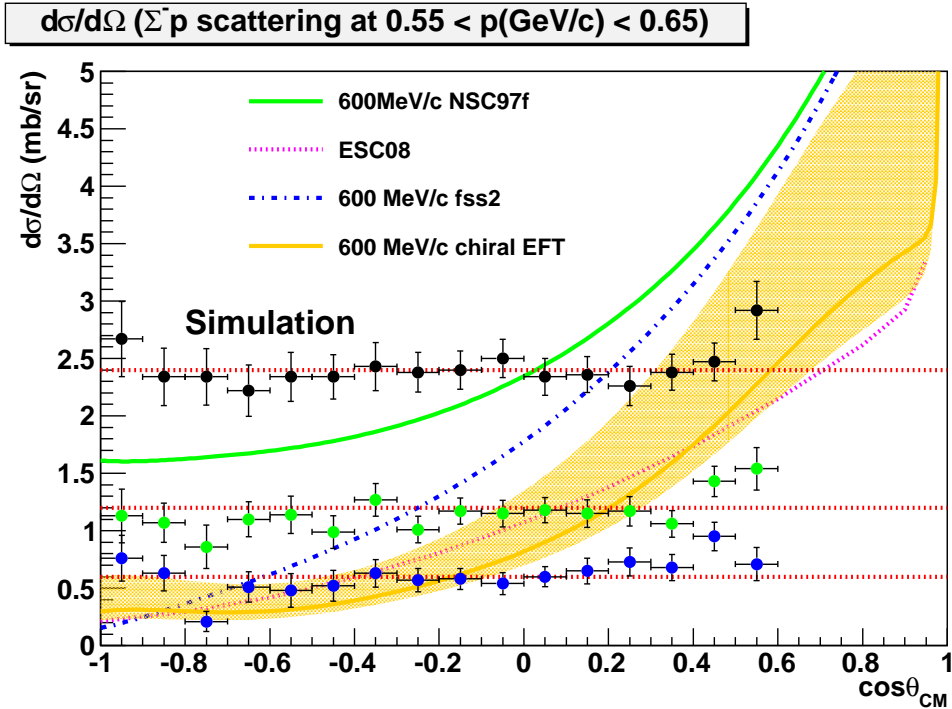
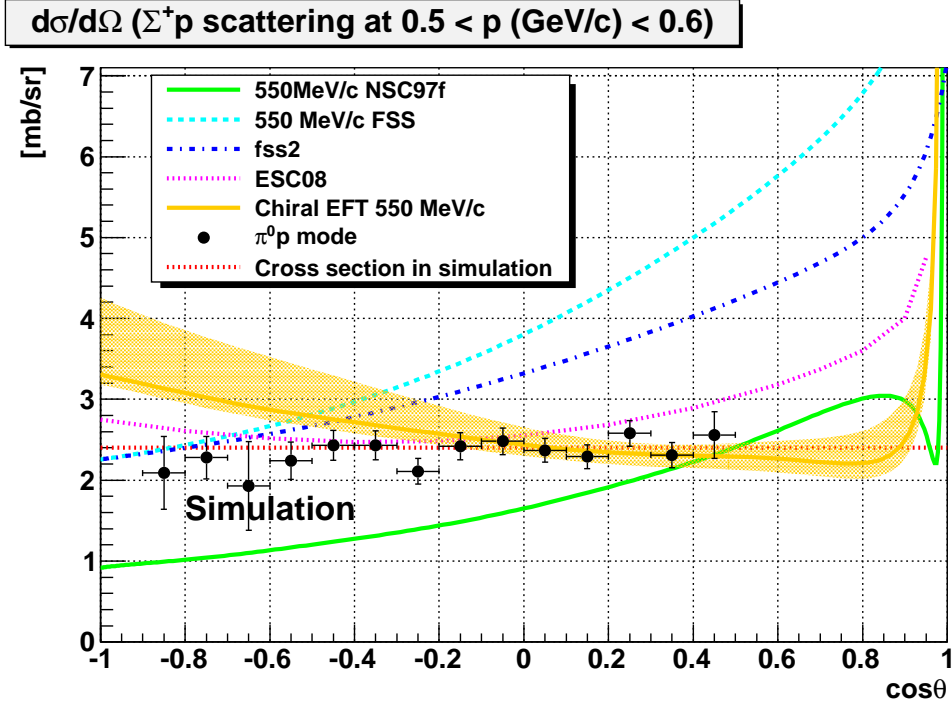


Figure 2.8: The differential cross section of the  $\Sigma p$  scattering predicted by theoretical models described in Chapter 1 (lines). The simulated accuracy of the cross section in the E40 experiment is also shown (dots). In this simulation, the differential cross section is assumed to be 2.4 mb/sr for the  $\Sigma^+ p$  scattering, and 2.4, 1.2 and 0.6 mb/sr for the  $\Sigma^- p$  scattering. The difference between the assumed cross section and the derived value is treated as a systematic error of E40 experiment. As the performance of CATCH system, the  $\Delta E$  resolution is assumed to be  $\sigma_{\Delta E} = 5$  MeV in this figure.

The simulation results for several assumed  $\Delta E$  resolutions are summarized in Table 2.3.

Table 2.3:  $\Delta E$  resolution dependence of the accuracy of the cross section

$\sigma_{\Delta E}$ [MeV]	4	7	9
Accuracy of $d\sigma/d\Omega$ at 2.4[mb/sr]	6.7%	8.6%	11.4%

As a result of the simulation, the resolution of  $\Delta E$  is required to be better than 7 MeV to achieve the accuracy of the cross section better than 10%.

Not only the  $\Delta E$  resolution but also the operation under a high rate environment is also important for the CATCH system. The required performances of the CATCH detectors are summarized in Table 2.4.

Each performance and requirement are explained in the following.

Table 2.4: Required performances for CATCH

Detectors	Requirements	Required performance
CFT	Time resolution Energy resolution Angular resolution	$\sigma_{time} < 2$ ns proton and $\pi$ can be discriminated $\sigma_{\theta} < 2$ degrees
BGO calorimeter	Energy resolution Counting rate for operation	$\sigma_{Energy} = 3\%$ at 80 MeV proton Operatable under Singles rate of $\sim 40$ kHz
CATCH system	Compact size Acceptance $\Delta E$ resolution	$-1 < \cos(\theta_{CM}) < 0.5$ $\sigma_{\Delta E} < 7$ MeV

## Requirement for $\Delta E$ resolution

In order to estimate the requirement for the CATCH system to satisfy the requirement of the  $\Delta E$  resolution, both resolutions of  $E_{p'calc}$  and  $E_{p'measure}$  should be discussed.

At first,  $E_{p'calc}$  is calculated from the energy of the  $\Sigma$  beam and the recoil angle of  $\Sigma p$  scattering. The momentum resolution of the  $\Sigma$  beam reconstructed by the spectrometer system is known to be  $10^{-2}$  as shown in Table 2.1. The recoil angle is obtained from the reconstructed direction of the  $\Sigma$  beam and the measured trajectory of the recoil proton from the  $\Sigma p$  scattering. Because the requirement for the  $\Delta E$  is 7 MeV ( $= \sqrt{\sigma_{E_{p'calc}}^2 + \sigma_{E_{p'measure}}^2}$ ), the resolution of

$E_{p'calc}$  ( $\sigma_{E_{p'calc}}$ ) is required to be about 5 MeV by assuming that  $\sigma_{E_{p'calc}}$  is comparable with  $\sigma_{E_{p'measure}}$ . By calculating the angular resolution that gives  $\sigma_{E_{p'calc}}$  of 5 MeV, the angular resolution  $\sigma_\theta = 2$  degrees was found to be required. The  $\sigma_{E_{p'calc}}$  value assuming this angular resolution of CFT is shown in Figure 2.9.

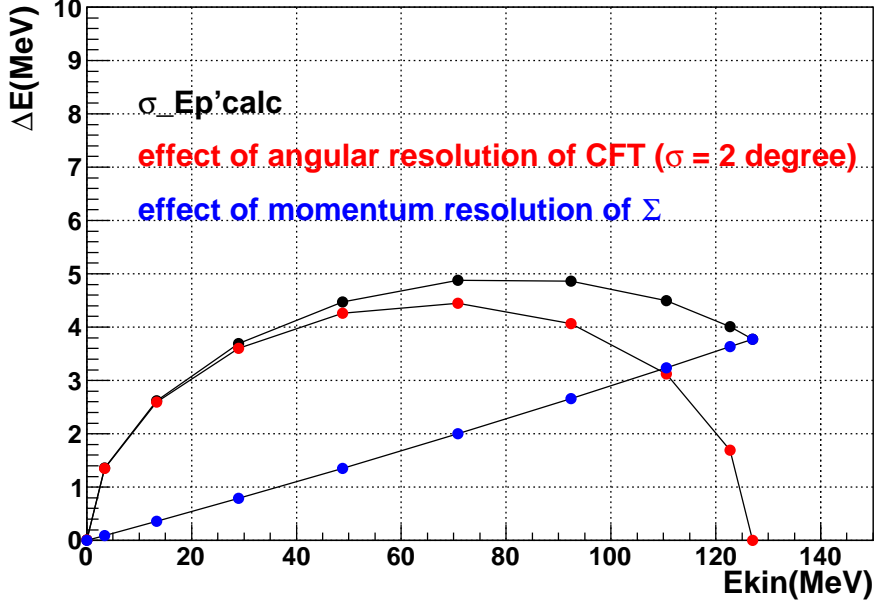


Figure 2.9: The correlation between the energy resolution of  $E_{p'calc}$  ( $\sigma_{E_{p'calc}}$ ) and the energy of the recoil proton from the  $\Sigma p$  scattering. Since the momentum resolution of the  $\Sigma$  beam is determined from the performance of the spectrometer system, in order to make  $\sigma_{E_{p'calc}}$  better than 5 MeV, the angular resolution of CFT ( $\sigma_\theta$ ) is required to be better than 2 degree.

The  $E_{p'measure}$  is obtained by adding the measured energy in CFT and the BGO calorimeter. The energy resolution of the BGO calorimeter is required to be better than 3% ( $\sigma$ ) for 80 MeV proton in order not to make  $\sigma_{\Delta E}$  worse [17].

The energy resolution of CFT also affects  $\sigma_{E_{p'measure}}$ . However, since the energy deposit in CFT is smaller than that in the BGO calorimeter, the influence of CFT is limited. In addition to the  $\Delta E$  method, the energy deposit in CFT is used to discriminate protons from pions, which are emitted from the decay of  $\Sigma$  or the scattered  $\pi$  beam. In order to separate  $\pi$  and proton, the energy resolution of CFT is required to be better than 25% ( $\sigma$ ).

Off course,  $\sigma_{\Delta E}$  should be as good as possible. The typical  $\sigma_{\Delta E}$  was obtained to be about 4 MeV assuming that the angular resolution of CFT ( $\sigma_{\theta}$ ) is  $1.2^\circ$  and the energy resolutions of CFT and the BGO calorimeter are 20% and 1% for 1 MeV and 80 MeV energy deposit, respectively. Even if the performance of each detector is slightly different from the assumed value, it is only necessary to satisfy the requirement of  $\Delta E < 7$  MeV in total.

### **Time resolution and operation under high rate**

Because a high rate  $\pi$  beam of 20 M/spill is used for the  $\Sigma$  production, many particles are incident on the detectors with high rates. The background protons such as those emitted from the  $\pi p$  scattering and others are incident to CATCH with the rate of 80 kHz. The CATCH detectors should be operable under such a high rate environment. The singles rates are estimated to be about 2 MHz and 40 kHz from a simulation for the most inner layer of CFT and one BGO crystals, respectively.

The  $\Sigma p$  scattering event is identified by combining the tagging the  $\Sigma$  production and detection of the recoil proton from the  $\Sigma p$  scattering. Under a high rate background condition, the  $\Sigma$  production event can make an accidental coincidence with a background event in CATCH, and such an accidental event can be a background of the  $\Sigma p$  scattering event. Therefore, in order to reject accidental coincidence background events, a sufficient time resolution is required for CFT to make a time gate narrow enough. In order to reject 99.9% of the accidental background, the width of the time gate is required to be 12 ns, which corresponds to  $\pm 3\sigma$  for the CFT time resolution of 2 ns ( $\sigma_{time}$ ).

For the BGO calorimeter, the singles rate is expected to be 40 kHz for the energy deposit of more than 5 MeV. Under such a high singles rate the pulse from the BGO calorimeter sometimes piles up. Moreover, there is a possibility that the singles rate becomes 5 times higher due to the beam structure. Therefore, the waveform readout of the BGO calorimeter with a flash ADC is adopted in order to decompose pile-up events.

## Acceptance

As the structure of detectors in CATCH, a large acceptance is required to increase the statistics of the yield of scattering events. Therefore, a cylindrical arrangement was adopted for the detectors to cover the target. The requirement for the size of the detector should also be considered. In the  $\Sigma p$  scattering experiment, both of the identification of the  $(\pi, K^+)$  reaction in the spectrometer analysis and the identification of  $\Sigma p$  scattering events must be performed. In order to increase the yield of the scattering events, the spectrometer magnet should be placed just behind the target as close as possible.

On the other hand, the recoil protons from  $\Sigma p$  scattering are more likely be emitted forward. Therefore, in order to realize a wide angular acceptance for the  $\Sigma p$  scattering event, it is important to detect the trajectory in the forward direction.

In order to satisfy these two requirements, the layers of CFT need to be located within the shortest possible space in the radial direction from the beam axis. Because it is possible to make a compact tracking detector with scintillation fibers because of the flexibility of the fiber installation, a scintillation fiber tracking detector was adopted as CFT. Also, the compact structure of CFT reduces the number of readout channels of fibers and the size of the outer calorimeter can be suppressed.

## 2.4 CATCH system

The detectors are designed to satisfy the requirements described above. The CATCH system consists of the Cylindrical Fiber Tracker (CFT) and the BGO calorimeter as shown in Figure 2.10.

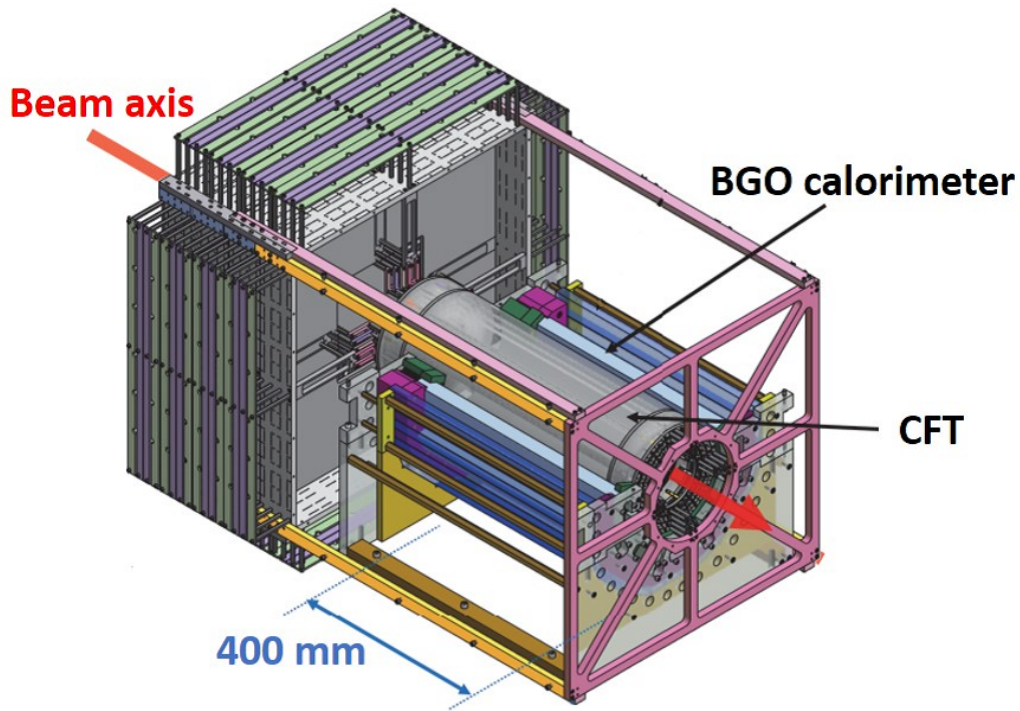


Figure 2.10: A figure of a new detector system called a Cylindrical Active Tracker and Calorimeter system for Hyperon-proton scattering ( “CATCH”). CATCH consists of the Cylindrical Fiber Tracker (CFT) and the BGO calorimeter in order to measure the trajectory and the energy of emitted protons from the target installed inside of CATCH.

The target system consists of a target cell made of  $250 \mu\text{m}$  thick Mylar and cylindrical Carbon Fiber Reinforced Plastics (CFRP) with a thickness of 1 mm. The inside of the target cell is filled with liquid hydrogen, and inside of the CFRP is evacuated for the heat insulation. The CATCH system is installed outside of the CFRP in the air. Figure 2.11 show the side and front views of the CATCH system.

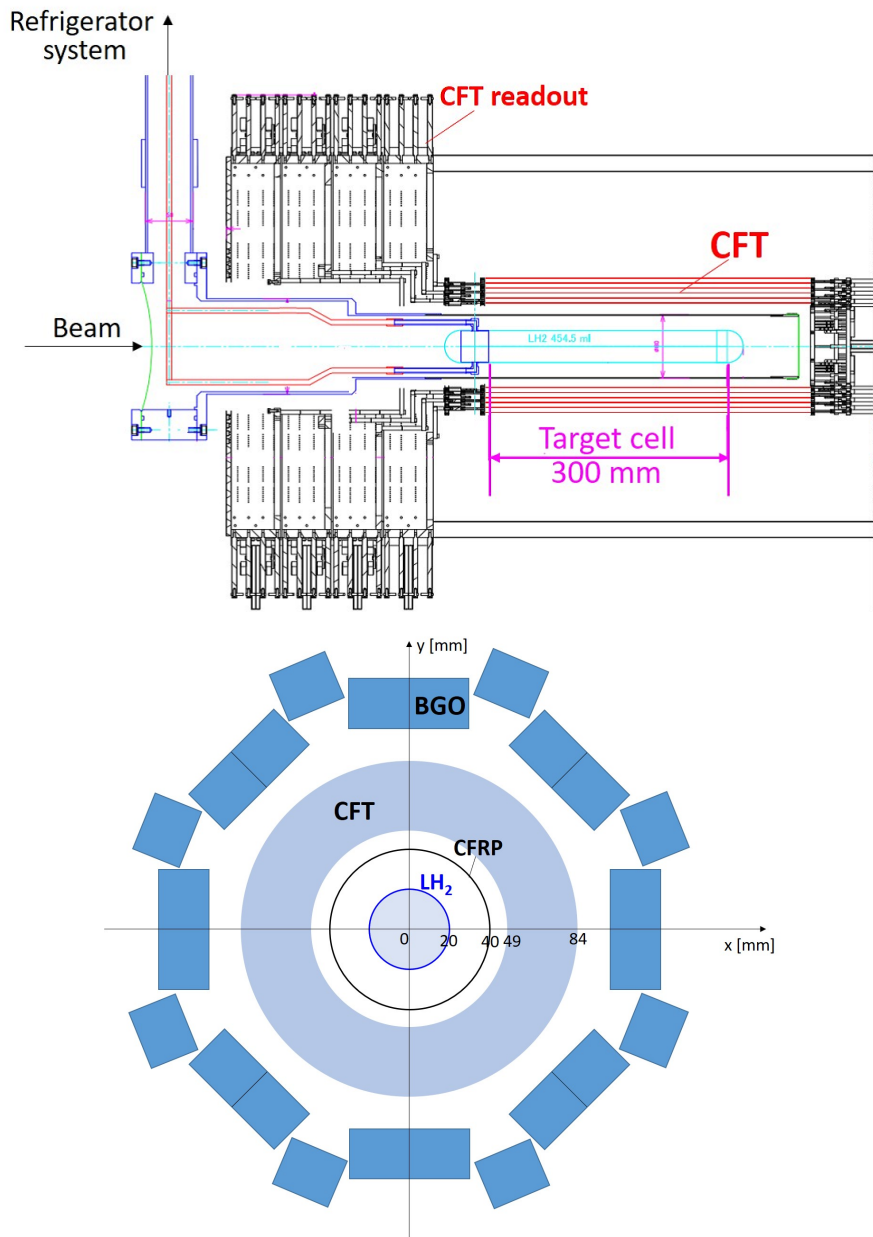


Figure 2.11: Top figure and bottom figures show the side and front views of the CATCH system.

The amount of materials is summarized in Table 2.5. In order to minimize the energy deposit in the CATCH system for the energy acceptance of the recoil proton, the amount of material in the passing area of particles before reaching to the BGO calorimeter was designed to be as small as possible. The BGO calorimeter has a large amount of material for stopping the particles in the

BGO calorimeter. The path length in CFT has an ambiguity due to the shape of the fiber and the layer structure.

Table 2.5: Amount of material in the CATCH system

Material	LH <sub>2</sub>	Target cell	CFRP	CFT	BGO
Amount [g/cm <sup>2</sup> ]	$1.4 \times 10^{-2}$	$3.4 \times 10^{-2}$	0.14	0.65 ~ 0.9	17.8

Figure 2.12 shows a typical relation between the flight distance and the total amount along the particle path. This figure shows the shortest case, which corresponds to  $\theta = 90$  degrees. The total amount of material becomes larger for the other  $\theta$  values.

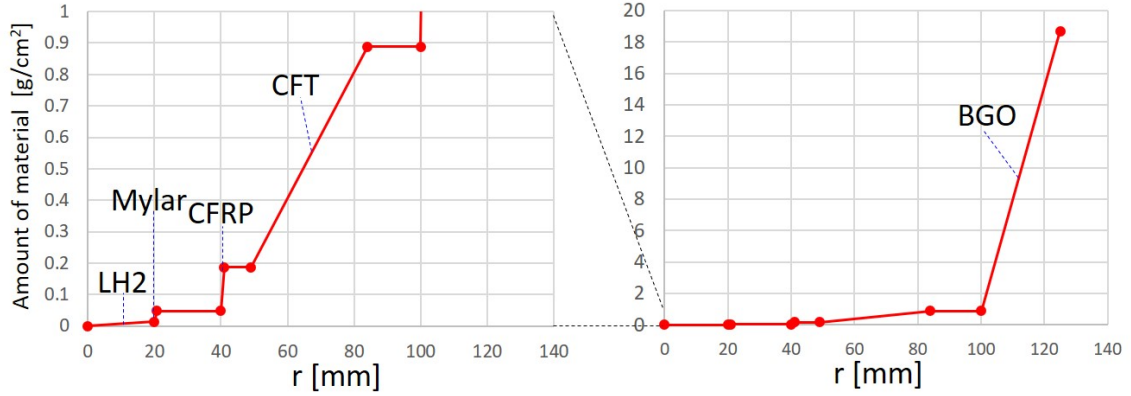


Figure 2.12: A typical relation between the flight distance and the total amount of material along the particle path. This figure shows the case of  $\theta = 90$  degree. The total amount of material becomes larger for the other  $\theta$  values.

The effect of the multiple Coulomb scattering of protons to the incident angle to CFT is estimated to be about 1.0 degree and 0.5 degrees ( $\theta_\theta$ ) from a simulation for 20 MeV and 80 MeV protons, respectively. The certainty of the energy deposit in CFT may affect the contribution of the multiple scattering. These spreads are smaller than the required angular resolution of CFT. However, especially in the low energy protons (lower than  $\sim 20$  MeV), since the fluctuation of the path length in CFT affect the probability of passing through, the detection efficiency should be evaluated carefully. On the other hand, when the energy of proton is sufficiently large, the detection efficiency does not change very much. The angular resolution was evaluated including the effect of the

fluctuation from the multiple scattering described in Chapter 5.

### **Cylindrical Fiber Tracking detector**

In order to obtain the recoil angle of  $\Sigma p$  scattering from the trajectory of recoil protons, it is necessary to measure the track in three dimensions. Amount of material in the tracking detector is required to be minimized to avoid protons from stopping in the detector before obtaining the trajectories. Therefore, it was designed so that basically only fibers exist in the measurement region. In addition, since  $\Delta E$  is obtained by using the scattering angle, a sufficient angular resolution is required. The contribution of the angular resolution of CFT to the  $\Delta E$  value is discussed in the next section.

Also, due to the decay of  $\Sigma$  particles ( $\Sigma^\pm \rightarrow n + \pi^\pm$ ) and  $\pi$  beams,  $\pi$  particles may be detected by the detector at the same time. In order to discriminate between  $\pi$  and protons, a sufficient energy resolution for energy deposit at the fibers is required.

### **BGO calorimeter**

The calorimeter measuring the kinetic energy of recoil protons is required to have a sufficient amount of material to measure the total kinetic energy. It is also required to be long enough to cover the target and the CFT length of 400 mm in the beam direction. We decided to fabricate a calorimeter with BGO scintillator from a viewpoint of energy resolution, density, size of crystal, and easy handling.

As for the BGO calorimeters, 24 BGO crystals are used to surround CFT. The size of one crystal piece is  $30 \times 25 \times 400 \text{ mm}^3$ . The BGO calorimeter is placed at the outer side of CFT.

## Chapter 3

# Structure and Development of CATCH system

The spectrometer systems which will be used for the  $\Sigma p$  scattering experiment have been already in operation at the J-PARC K1.8 beam line.

The detector structures were based on their requirements. Through some prototypes production[17], we completed the actual type of the CATCH system. The structures and fabrications of the CATCH detectors are described in this chapter.

### 3.1 Cylindrical Fiber Tracker

Cylindrical Fiber Tracker (CFT) is a detector that measures the trajectories of recoil protons emitted from  $\Sigma p$  scattering.

#### 3.1.1 Features of a Fiber Tracker

A scintillation fiber tracker is a detector that measures the passing position of the particles. A scintillation fiber is a fiber-shaped plastic scintillator, and emits scintillation photon when charged particles pass through the fiber. Like a optical fiber, the material of the inner core and the material of the outer cladding are different, and the scintillation photon is transmitted to the end by utilizing the total reflection occurring at the boundary surface due to the difference in index of reflection. By detecting scintillation light with a photon detector connected to the fiber end, the particle hit information is obtained.

A scintillation fiber tracker consists of many scintillation fibers, whose positions are well known. Therefore, information on which fiber has a signal provides the position information of incident particle. Tracks are reconstructed by using multiple layers of arranged fibers.

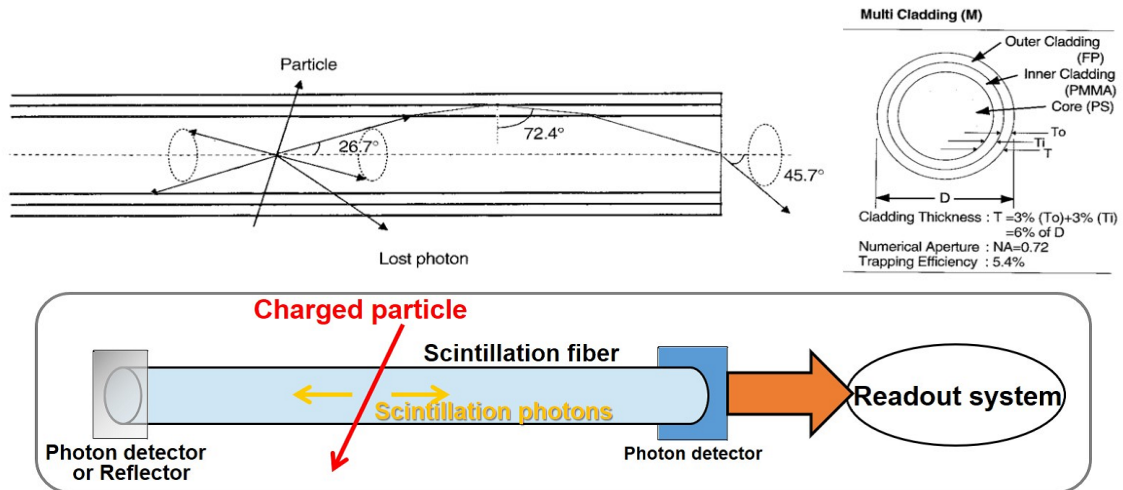


Figure 3.1: These figures show the principle of a scintillation fiber detector. A scintillation fiber emits scintillation photon when charged particles pass through the fiber. The scintillation photon is transmitted to a photon sensor installed at the end of fiber.

The features of scintillation fiber tracker are as follows.

- Flexibility in shape.
- Time response is fast, so that operation in high rate environment is possible.
- Energy deposit in the fiber is measurable.

### 3.1.2 Specification and Structure

Important specifications for the angle measurement by the fiber detector are the fiber diameter and the installation accuracy of the fiber positions. If the diameter of the fiber is reduced, the position resolution is improved, but the number of readouts increases. Insufficient precision of the installation position of the fiber deteriorates not only the position resolution but also the detection efficiency due to the gaps between fibers. On the contrary, if the fiber diameter

is large, the required number of fibers is small, but the position resolution drops down. Furthermore, when fibers are arranged in a spiral shape, its hardness makes it difficult to fabricate a tracker from fibers with a large diameter.

Considering the optimization of the position resolution, the number of read-out, easiness of fabrication, etc., 0.75 mm  $\phi$  was chosen as the fiber diameter(Kuraray SCSF-M78NN[18]).

Since it is necessary to obtain information on a track position in three dimensions, two kinds of position measurement axes are required. In CFT, two types of arrangements were introduced: The straight layer in which fibers are arranged parallel to the beam axis and the spiral layer in which the fibers extends along the side of the cylinder centered on the beam axis as shown Figure 3.2.

In the following, the coordinate axes are defined as in Figure 3.2 for the cylindrical shape of CFT. The  $xy$  plane is taken on the plane perpendicular to the center axis of the cylinder, and the angle of the circular direction is taken as  $\phi$ . The center of the circle is defined as the position of  $(x, y) = (0, 0)$ . Also define the  $z$  axis in the central axis direction.

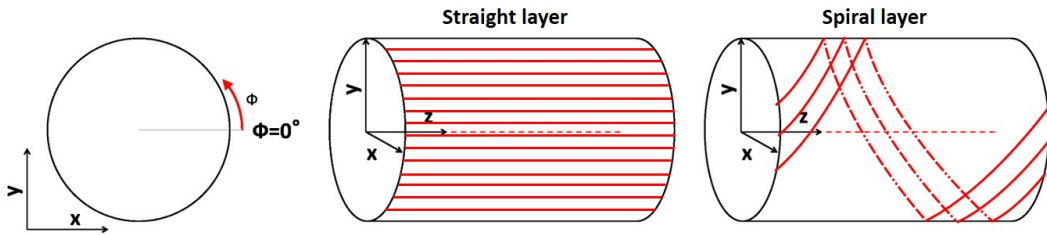


Figure 3.2: These figures show structures of fiber arrangement for straight layer and spiral layer of CFT. A straight layer consists of fibers installed in parallel to the beam axis. A spiral layer consists of fibers installed along the side of the cylinder centered on the beam axis.

An active region of CFT, where the fiber positions are determined is designed to be 400 mm in the beam direction in order to cover for a large acceptance. The spiral layer's fibers are arranged between the both ends of active region and the fibers just rotate 360 degrees around the central axis during one end of active region to another end. This makes a correlation between  $\phi$  and  $z$ , and the position information in the  $z$  direction is obtained by combining the

hits on the straight and spiral layers. By using such a fiber arrangement, three dimensional position can be obtained from each hit information as shown in Figure 3.3

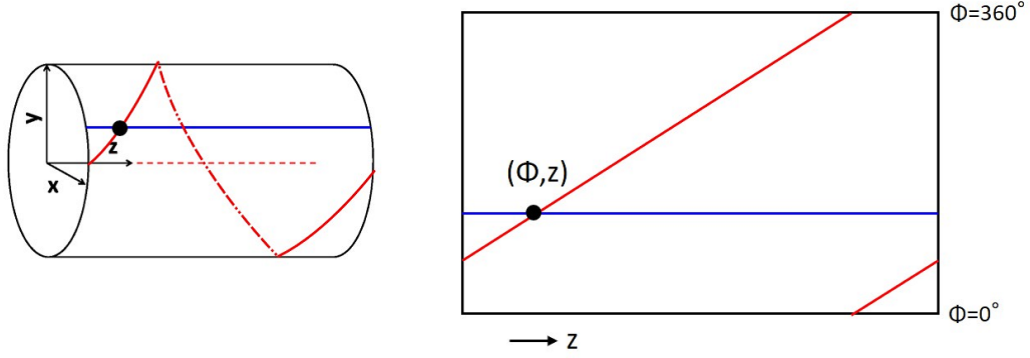


Figure 3.3: Two fiber structure makes a correlation between the angle  $\phi$  and  $z$ . The hit position in the direction of  $\phi$  is obtained from straight layer. And the hit position in the  $z$  direction is obtained by combining the hits of the straight and spiral layers.

Three-dimensional trajectory reconstruction is possible by using combination of these fiber arrangement structures. In order to achieve a wide angular acceptance, a structure was designed to have a total of 8 layers with a length of 400 mm in the  $z$  direction, 4 layers of straight layer and the other 4 spiral layer, located at  $r = 52 \sim 84$  mm in the radial direction. The specifications of each layer are summarized below.

Straight Layer	Layer1	Layer2	Layer3	Layer4
Installation radius [mm]	54	64	74	84
Number of fibers	584	692	800	910

Spiral Layer	Layer1	Layer2	Layer3	Layer4
Installation radius [mm]	49	59	69	79
Number of fibers	426	472	510	538
Tilt angle [degree]	37.6	42.8	47.3	51.1

### 3.1.3 Fabrication

In this section, a fabrication method for realizing the above-described fiber arrangement is described.

In order to realize a compact layer structure, four frames were prepared and fabricated separately, and they were combined later as shown in Figure 3.4. The fourth frame is shown in the Figure as an example. For each frame, one straight layer and one spiral layer are installed together. Scintillation fibers were read by a single side at fiber readout edge and reflector for photons is attached at the another fiber edge.

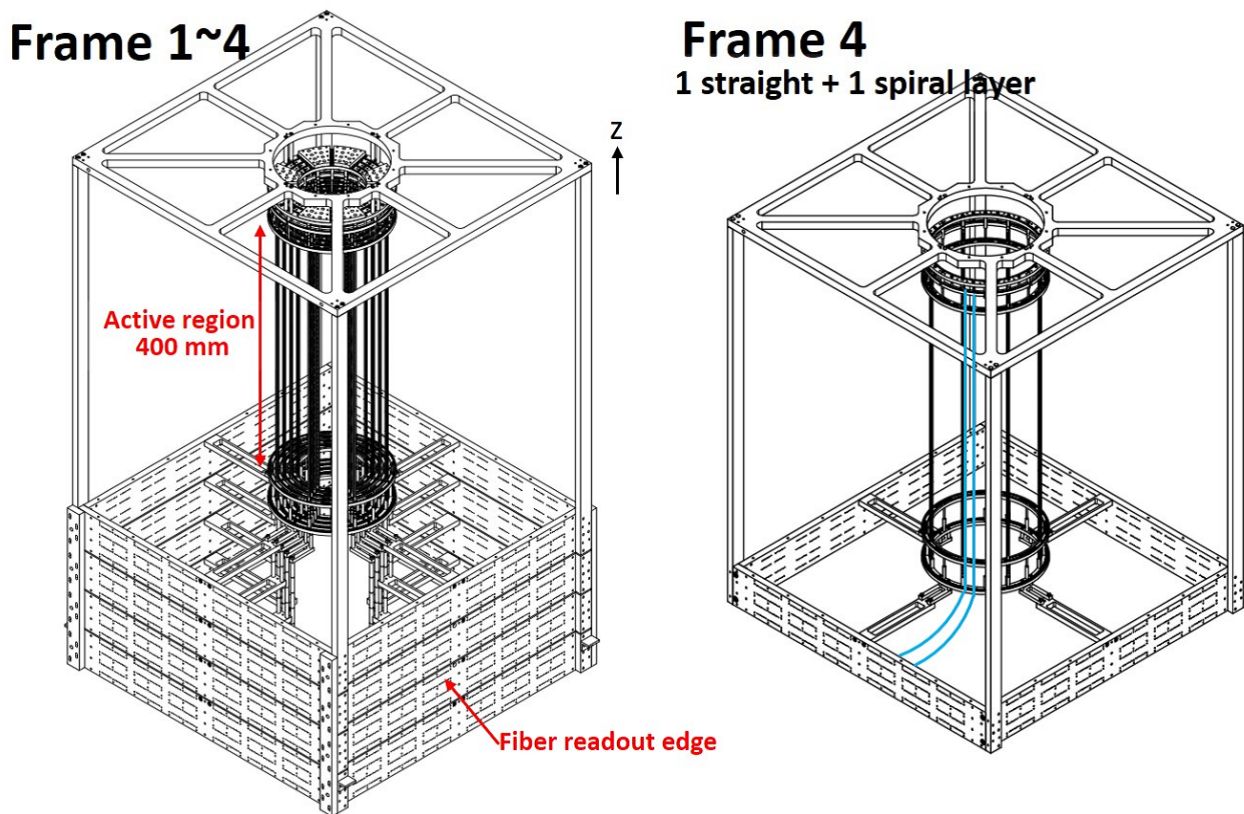


Figure 3.4: CFT consists of 4 frames, which compose 1 straight layer and 1 spiral layer for each frame in order to realize a compact layer structure. Each frame was fabricated separately and combined after fabrication. The fourth frame is shown as an example in the right figure.

- Straight layer

As fiber trackers developed in the past, such as BFT and SFT, etc. are actually used in J-PARC K1.8 beamline. They are the fiber trackers in which fibers are arranged on a plane. For the fabrication of these detectors, we firstly arranged a sheet with fibers side by side, and fixed fibers each seat to a frame. However, the method of arranging fibers in a cylindrical shape by the method of forming the sheet has a difficulty in shaping the sheet into a cylinder and a problem in the accuracy of the fiber position. Therefore, a new method of arranging each fiber one by one on a fiber fix frame was introduced.

In order to enable the fiber arrangement for the straight layer, holes with diameter of 0.80 mm were drilled on the fiber fix frame for a fiber diameter of 0.75 mm. These fiber fix frames were placed at both ends of the active region of the detector. By fixing the fibers through the corresponding holes at both ends, they were stretched in a straight line to obtain accuracy of the position of the fiber. Fibers were arranged with a staggered structure in order to reduce the ineffective area of detection. If the fibers are stretched correctly, position information can be correctly obtained. Figure 3.5 shows the frame with holes for fixing the fibers of the straight layers.

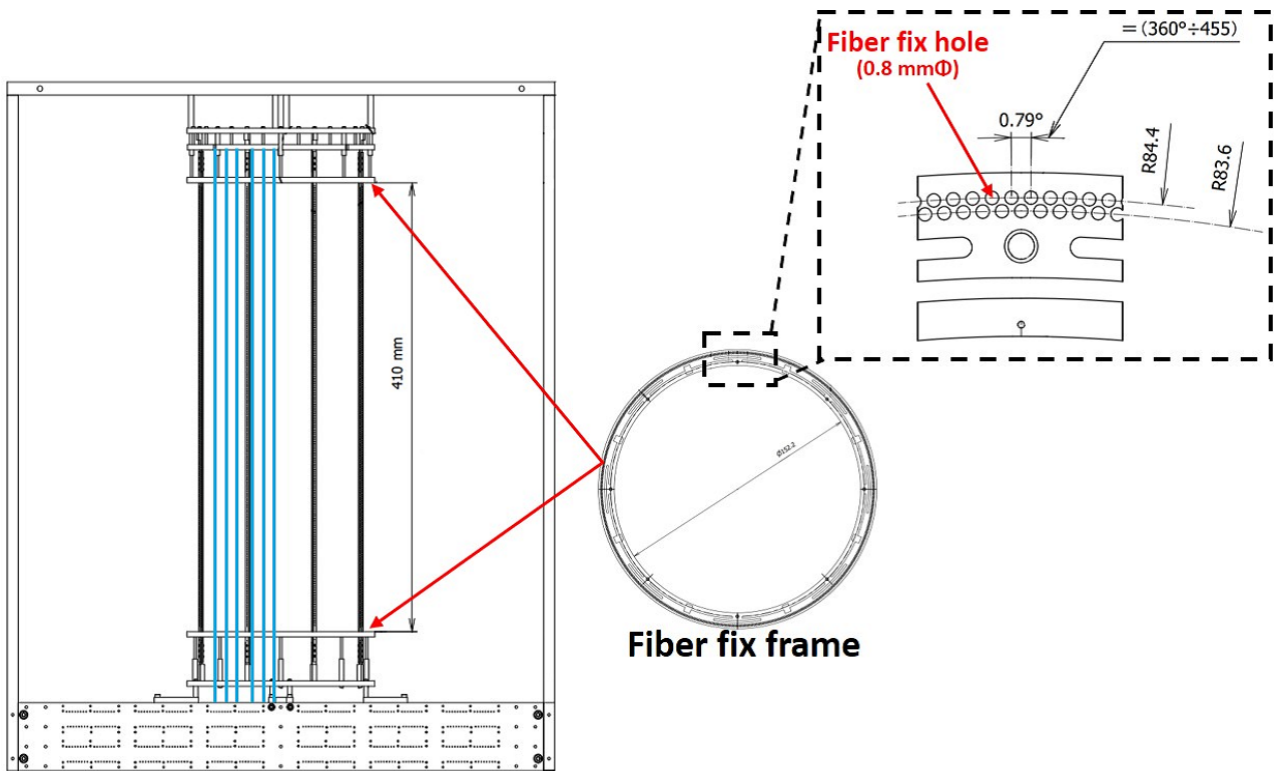


Figure 3.5: The fiber fix frames with holes for fiber by fiber were placed at both ends of the active region. By fixing the fibers through the corresponding holes at both ends, they were stretched in a straight line to obtain accuracy of the position of the fiber. Fibers were arranged with a staggered structure in order to reduce the ineffective area of detection.

Figure 3.6 shows a picture of the fibers actually passing through the holes of the fiber fix frame. After passing the fibers through the fiber fix frame, the fiber position was fixed by gluing the fiber and the frame with optical cement. Figure 3.7 shows a picture of the fibers going to the readout frame after passing through the fix frame.

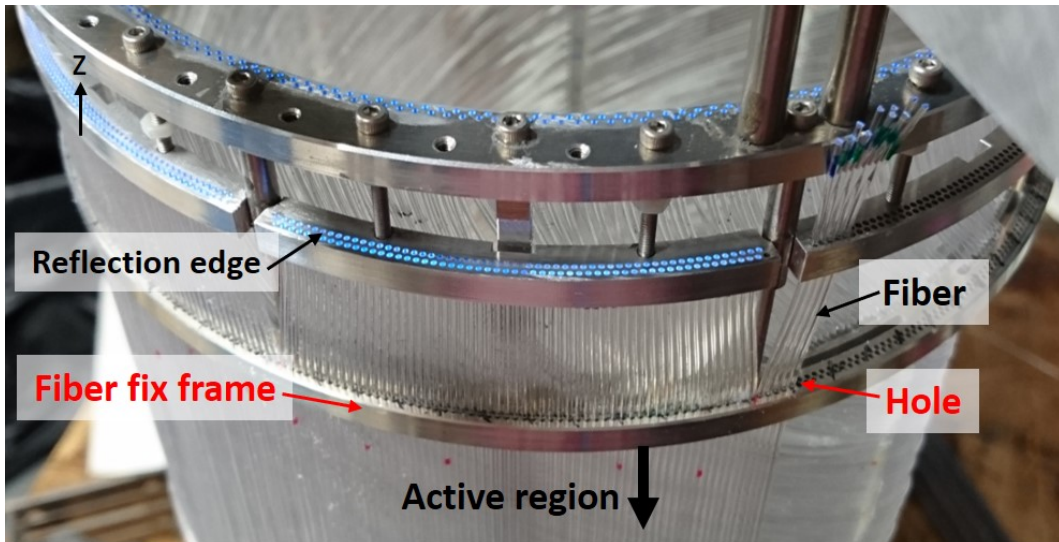


Figure 3.6: A picture of the fibers actually passing through the holes drilled on the fiber fix frame at the reflection side. Reflection edge before attaching the reflector sheet is also shown in this picture.

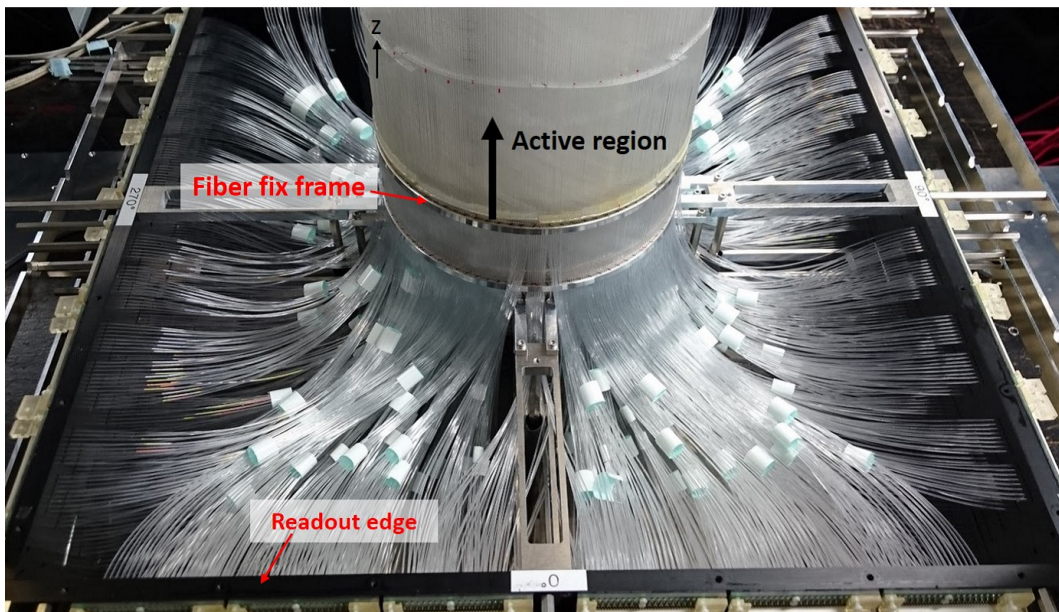


Figure 3.7: A picture shows the fibers going to the readout frame after passing through the holes of the fix frame.

- Spiral layer

The spiral layer has a structure in which fibers are arranged in a spiral shape along the surface of a cylinder centered on the beam axis.

In order to fix the position of the fibers, we introduced a special method described below. Although the amount of material increases, we decided to introduce “fiber position frames” for fixing the fibers at eight circular points with  $45^\circ$  interval in a cylindrical shape through which the fiber passes. The fiber position frame consists of two frames and pins as shown in the right figure of Figure 3.8. The positioning pins of  $400\ \mu\text{m}$  in diameter were used as shown in Figure 3.8. These pins were made of carbon. In this way, the spiral structure of fiber was realized. Eventually, in order to reduce the amount of material, the position frames were removed leaving two of them after being bonded with adhesive.

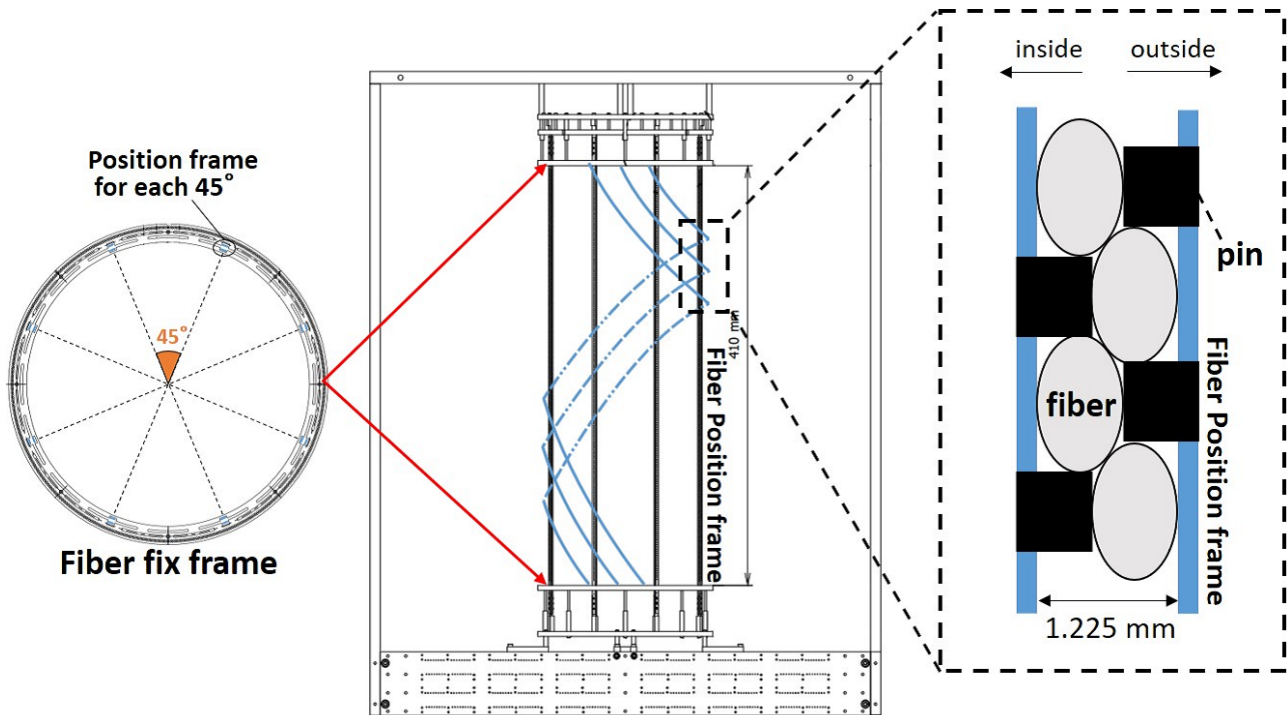


Figure 3.8: By placing the fiber position frames in the  $\phi$  direction at each  $45^\circ$ , the  $z$  position of each fiber at the frame location was determined to realize the spiral structure. The position frame consist of two frames and pins fixing the fibers.

Figure 3.9 shows the fibers of the spiral layer fixed at the fiber position frame with pins viewed from outside and inside.

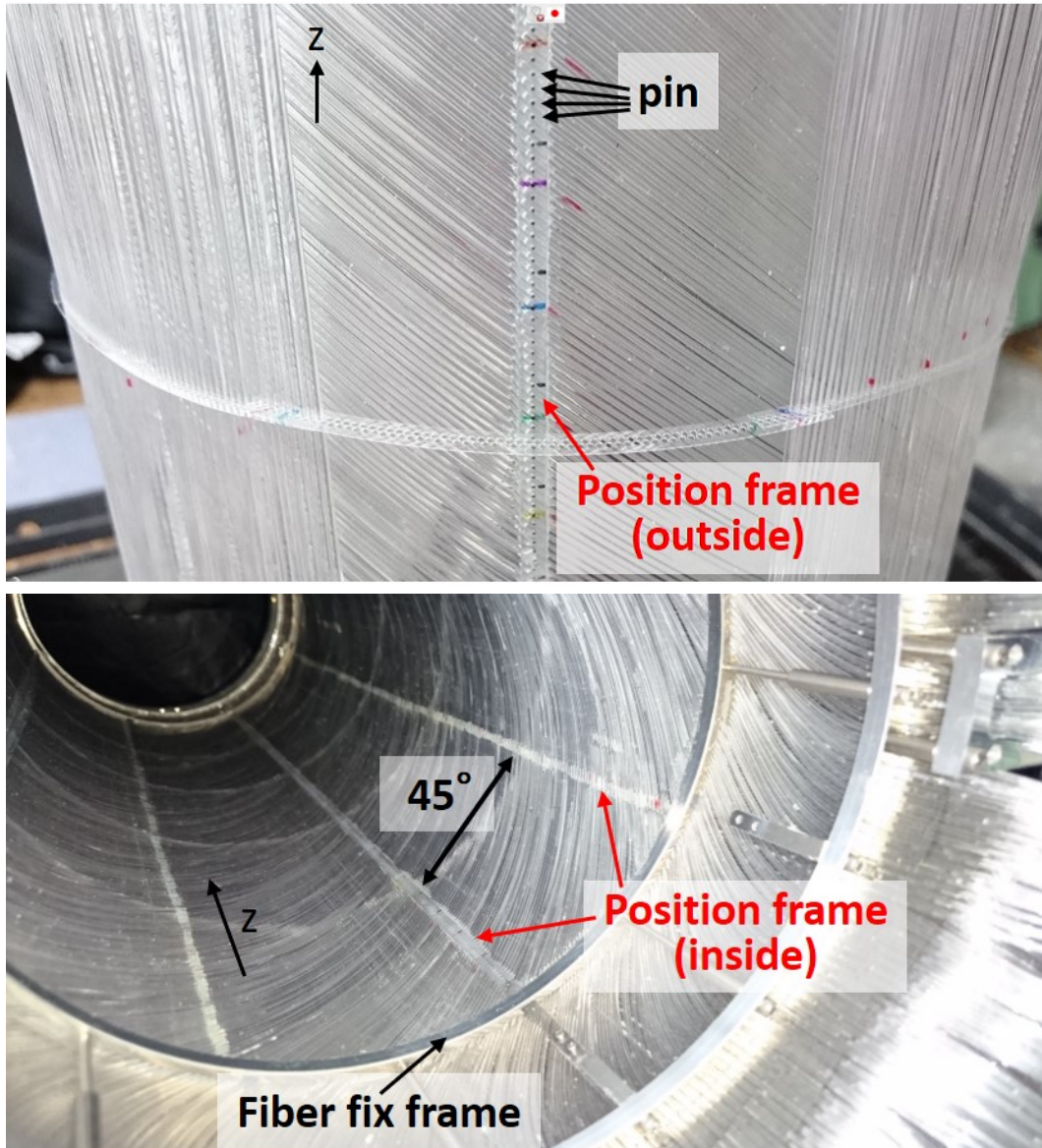


Figure 3.9: Upper and lower pictures show the fibers of the spiral layer fixed at the position frame placed at each  $45^\circ$  with pins seen from outside and inside, respectively.

There were some difficulties on the fabrication of such a special fiber structure. These difficulties and devises to solve them are explained in the appendix

- Docking

In addition, by adopting a structure in which each layer of the straight and the spiral is arranged in the same fixed frame, a compact structure was realized. After fabrication of all layers, they were combined to one detector.

### 3.2 BGO Calorimeter

The BGO calorimeter is a set of scintillation counters which measure the energy of the recoil proton from  $\Sigma p$  scattering. The energy of the proton is estimated to be continuous up to 150 MeV. The energy resolution of the calorimeter is required to be better than 3% ( $\sigma$ ) for 80 MeV proton, which is a typical energy of the recoil protons. Since a high intensity  $\pi$  beam is used in the  $\Sigma p$  scattering experiment, a high singles rate of 40 to 400 kHz is expected for the calorimeter. Therefore, it is required to be operable under such a high rate environment.

In order to satisfy these requirements, the following specifications were adopted. The size of one BGO crystal piece is  $30 \times 25 \times 400 \text{ mm}^3$ , and 24 crystals are used in order to surround CFT. Photomultiplier tubes (Hamamatsu H11934-100) are used as readout sensors.



Figure 3.10: A picture of BGO crystal, whose size is  $30 \times 25 \times 400 \text{ mm}^3$ , for scintillation calorimeter.

We should be careful for its rate tolerance, because the decay time of 300 ns of BGO crystal is rather long. The singles rate of the BGO calorimeter is expected to be 40 kHz for the energy deposit more than 5 MeV. If we consider the time structure of the J-PARC beam, the BGO calorimeter should be stable under 5 times higher singles rate.

Under such singles rate the pulse from BGO calorimeter may pile up. In order to decompose the pile-up events, we selected the waveform readout using a flash ADC. If we take the waveform data of the raw BGO signal, a high

sampling rate is necessary to detect the fast leading edge of the signal. Because the BGO signal is rather long ( $1\mu\text{s}$ ), the data size becomes very large. In order to reduce the data size, the BGO signal is filtered with an integration circuit and the shaped signal is sampled with a low sampling rate. Figure 3.11 shows the readout procedure of BGO calorimeter with Flash ADC.

As a result of our previous research[19] on optimization of the sampling interval and the energy resolution, we adopted a condition of a shaping time of about 100 ns for rise time and a 33 MHz sampling . In order to realize this condition, the time constant of the integration circuit (RC circuit) was set to 39.6 ns ( $R = 120\ \Omega$  and  $C = 330\ \text{pF}$ ) Furthermore, by shortening the fall time by the Pole Zero Cancellation (PZC) circuit, the performance of waveform separation was improved. We have decided to use 33 MHz clock, which corresponds to the slowest clock supported in CAEN V1724 module which will be used in E40. Under this condition it is estimated that the pulse height information can be acquired with an efficiency of 99% at a single rate of 40 kHz. Figure 3.11 shows a procedure of BGO readout.

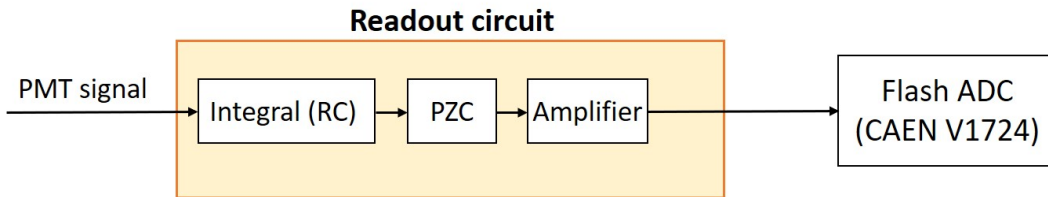


Figure 3.11: This schema show the readout procedure of BGO calorimeter with Flash ADC. In order to reduce the data size, the shaped signal is sampled with a low sampling rate. PMT signal from BGO crystal is filtered with a integral circuit and PZC circuit and amplified.

The right figure in Figure 3.13 shows the template function which is obtained as a mean waveform from a lot of waveform data. By using the waveform readout method, we confirmed that the sufficient energy resolution of 0.8% for 80 MeV proton was obtained with 30 ns sampling.

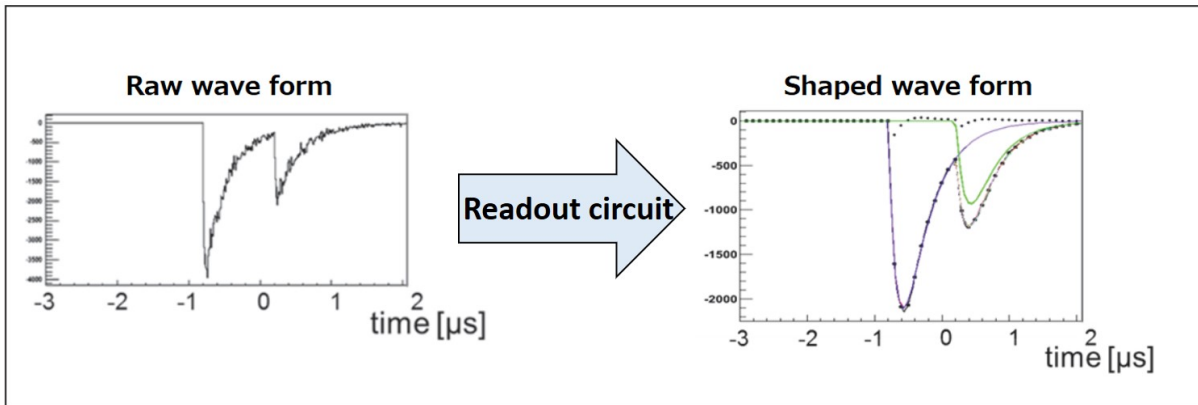


Figure 3.12: These figures show the BGO waveform before and after shaping with the shaping circuit. After shaping, the waveform can be separated with lower sampling points

With this readout method,  $\sigma_{EBGO} = 1.0\%$  was obtained for the 80 MeV proton from the experimental result of a test experiment irradiating the proton beam to one BGO scintillators. This result satisfied well the required performance of 3%.

The detectors of all 24 BGO scintillators and their reading circuits had were constructed. However, the tested scintillators, which were irradiated by proton beam, were only a part of all the scintillators . In the study of this thesis, we read out all BGO scintillators and evaluate their energy measurement performance.

### 3.3 PiID counter

For a good particle identification, we also install a PiID counter, which is a plastic scintillator located at the outside of the BGO calorimeter. Because almost all  $\pi$  particles from hyperon decay penetrate the BGO calorimeter, the hit information of the PiID counter helps the particle identification between  $\pi$  and proton. Basically they are identified with the  $\Delta E - E$  information of the CFT fibers and the BGO calorimeter. We are considering plastic scintillators with a wave length shifting fiber to which a MPPC is attached.

The PiID counter is under production at the time of writing this thesis.

### 3.4 MPPC readout system with EASIROC board

The scintillation light in each CFT fiber is read fiber by fiber with a MPPC (1 mm<sup>2</sup>, 400 pixel). Since we use about 5000 fibers for CFT, we need to handle this large amount of information. Not only CFT, the PiID counter and some other detectors in the spectrometer system also use MPPCs as their readout. An attachment method between the fibers and MPPCs are described in Ref. [17].

MPPCs are operated and readout by the Extended Analogue Silicon Photo-multipliers Integrated ReadOut Chip (EASIROC) boards[20][21] which were developed by our group using an EASIROC chip developed by Omega/IN2P3[22]. The board was specialized for the readout of such a large number of MPPCs

The main features of the EASIROC board are as follows.,

- 64 channels are read out per board,
- MPPC bias voltage is adjustable with accuracy of 20 mV,
- It incorporates Multihit TDC (1 ns/ch),
- It incorporates ADC with two different dynamic ranges (High Gain, Low Gain).

Since we use about 5000 fibers for 8 layer of CFT, 79 EASIROC boards are used for the readout.

Because the gain and dark current of MPPC are sensitive to the operation voltage and the optimal operation voltage of each MPPC is slightly different, a mechanism for adjusting the operation voltage of each MPPC is necessary in order to perform multi-channel MPPC readout. For that purpose, the EASIROC board has a bias voltage adjustment function. The operation voltage is adjusted by adjusting the voltage of GND on the reading side called InputDAC for each MPPC. In this way, the gains of MPPCs can be made uniform to the same detection number of photon.

Furthermore, on the EASIROC board, two kinds of (High gain, Low gain) ADCs are implemented for each readout channel. Two types of ADCs are prepared to measure a wider range of light yield. In addition, it has a discriminator inside and can obtain information on TDC.

### 3.5 Data acquisition system and Data set of CATCH system

Our DAQ system for the CATCH system consists of an Event Builder PC and Frontend PCs including VME Onboard CPU and PCs to collect data from SiTCP modules such as VME-EASIROC and so on. There are Frontend PCs for each detector component. The data are transmitted to Event Builder PC by TCP/IP. In the  $\Sigma p$  scattering experiment, other detector part of the spectrometer system will be added.

One Flash ADC for BGO calorimeter is read by Onboard CPU for synchronization with DAQ and the other two modules are read by optical link.

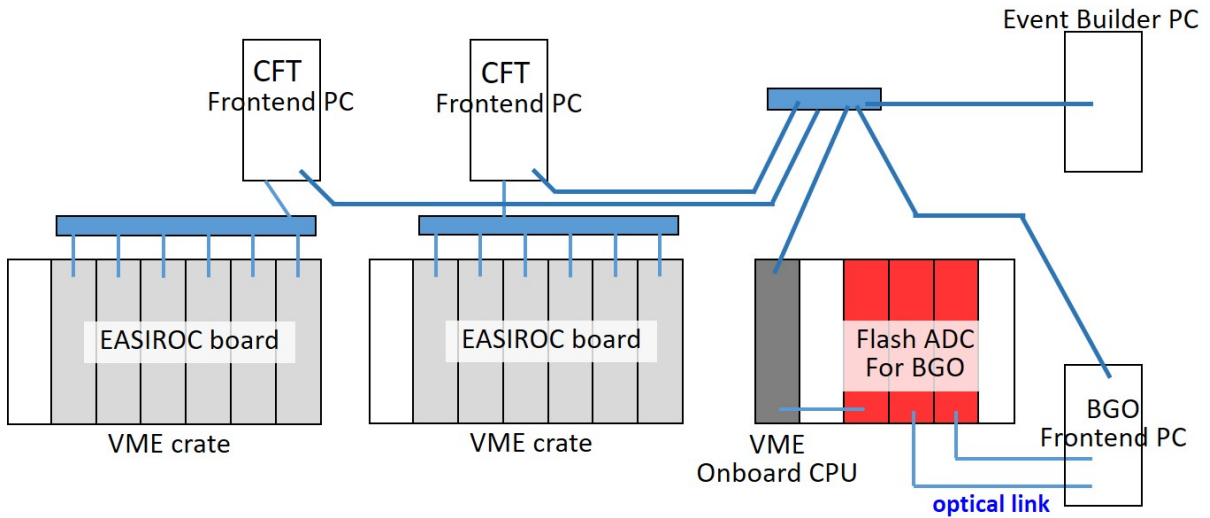


Figure 3.13: Illustration of DAQ system.

Here, the data set to be acquired for CATCH is summarized in the table 3.1. The ADC and TDC data from CFT are read out for each fiber in order to obtain

Table 3.1: Measurement data set of CATCH system

Detector	data	channels	comment
CFT	ADC	5,000	pulse high (high and low gain)
	TDC	5,000	multi hit
BGO	Flash ADC	24	wave form

the hit information and energy information. The waveform data of the BGO calorimeter are read in order to obtain energy information and discriminate

pile-up events.

### 3.6 The process to the application of CATCH system

Detector part and readout system of CATCH system were constructed. In order to evaluate the performance to derive the differential cross section, we measured the  $pp$  and  $pC$  scattering events as a test. This test experiment includes the purpose to establish the analysis method with CATCH system at first time. Before the measurement of the scattering cross section, there were some performances which were need to be corrected or calibrated.

The process to obtaining the scattering cross section is briefly summarized in following,

1. Fiber position correction,
2. Energy calibration,
3. Event identification from  $\Delta E$  distribution,
4. Estimation of the detection efficiency of CATCH system,
5. Derivation of the cross section.

At first, because there was possibility that the fiber position was slightly deviate from the designed position, we performed the cosmic ray measurement experiment in order to correct the fiber position. After that, we performed the  $pp$  and  $pC$  scattering experiment in order to evaluate the performances of CATCH system for deriving the differential cross section which were necessary to estimate the performance in the  $\Sigma p$  scattering experiment.

## Chapter 4

# Commissioning of Cylindrical Fiber Tracker

The Cylindrical Fiber Tracker (CFT) has been constructed. In order to launch the CFT, at first, we measured cosmic ray, and checked ADC and TDC spectra of all the CFT channels. One of the most important purposes of this measurement is to collect calibration data for the CFT fiber positions. Because cosmic rays pass through with the straight line, the cosmic ray data can be used for the evaluation of the uncertainty of the fiber position.

### 4.1 Cosmic ray measurement with CFT

All channels of CFT fibers were connected to the readout MPPCs, and the readout cables with a length of 20 m were used between MPPCs and Easiroc board, which are the same with the  $\Sigma p$  scattering experiment at J-PARC. The CFT was installed so that the  $z$  axis was horizontal, which was also the same installation direction with the  $\Sigma p$  scattering experiment.

In order to measure the cosmic ray with a large acceptance, a coincidence signal of the innermost first and second straight layers was used to make the data taking trigger. Figure 4.1 shows a diagram of a method of trigger generation.

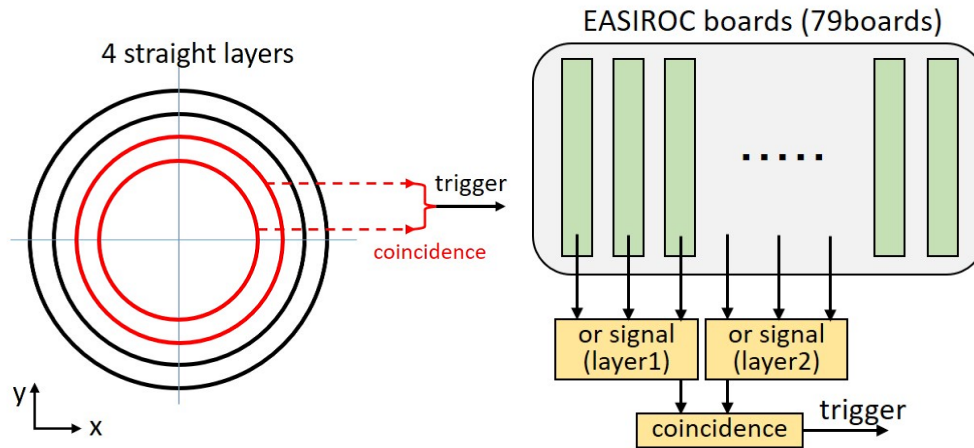


Figure 4.1: A diagram of trigger logic for CATCH measuring cosmic ray and incident particles. A coincidence signal of the innermost first and second straight layers was used to make the data taking trigger.

By using this trigger condition, not only event passing through the center position of the CFT, but also event s passing through the edge region of CFT were measured. Figure 4.2 show the example events measured by this trigger condition.

This measurement was performed in a experimental room at CYRIC ( Cyclotron Radio Isotope Center, Tohoku University) for about 2 days with the same condition of operation. Although there were restrictions on the statistics due to the schedule, the calibration data using cosmic ray can be taken again in the future. Therefore, the result of following analysis is possible to be improved with high statistics.

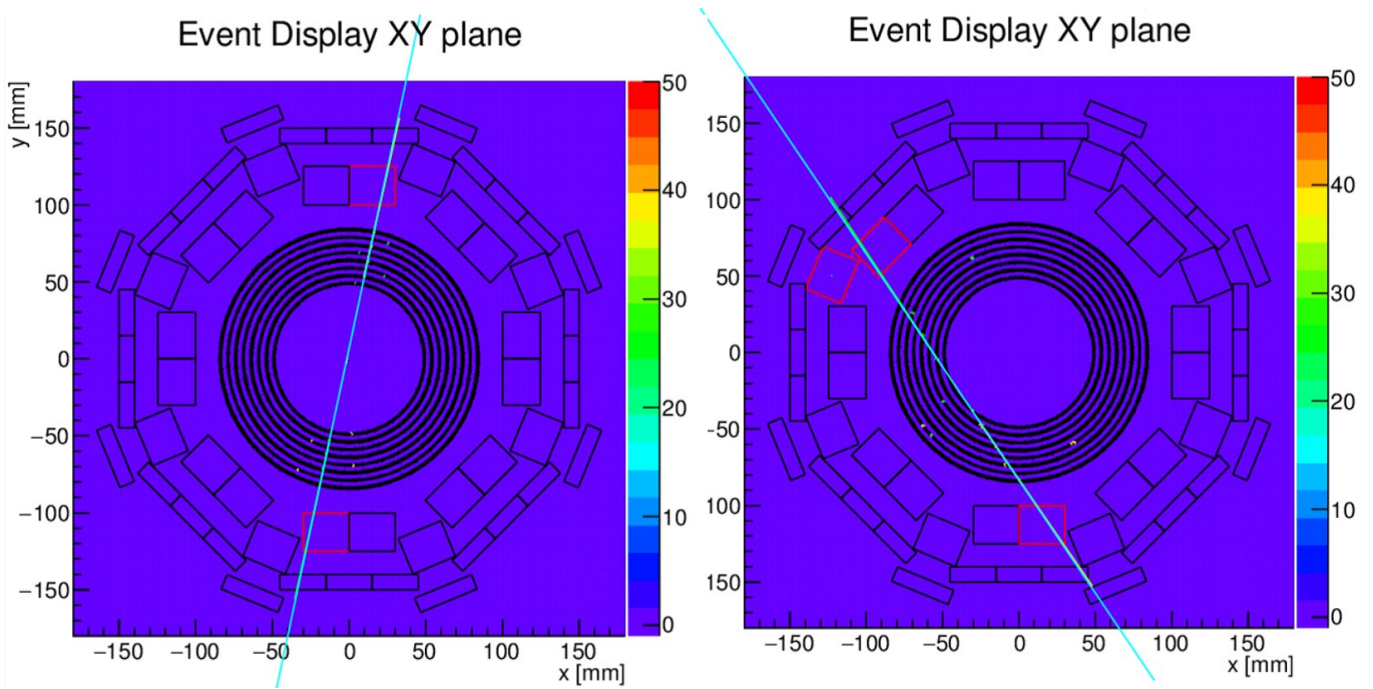


Figure 4.2: The measured cosmic ray data with a coincidence trigger of the innermost first and second straight layers. Not only event passing through the center position of the CFT as shown in left figure, but also event s passing through the edge region of CFT were measured as shown in right figure.

## 4.2 Measured data

Photons from CFT are detected by MPPCs and the signals from MPPC are sent to the EASIROC boards. The measurement condition is summarized in Table 4.1.

Table 4.1: Measurement condition for cosmic ray.

Setup	CFT (+ BGO calorimeter)
Trigger	Coincidence of the CFT 1 <sup>st</sup> and 2 <sup>nd</sup> straight layer
CFT MPPC Threshold	4 ~ 5 p.e.
Measurement period	about 2 days

The ADC and TDC data from CFT are read out for each fiber in order to obtain the hit information to reconstruct trajectories of cosmic rays.

### 4.2.1 CFT ADC

Figure 4.3 shows the scatter plot between the CFT fiber segments and the ADC distributions of the straight first layer for cosmic rays. In this histogram, the TDC hit is required to remove pedestal events. Here, the threshold for the TDC signal was set to 4 ~ 5 p.e.

The right figure of Figure 4.3 shows ADC distribution after subtracting its pedestal.

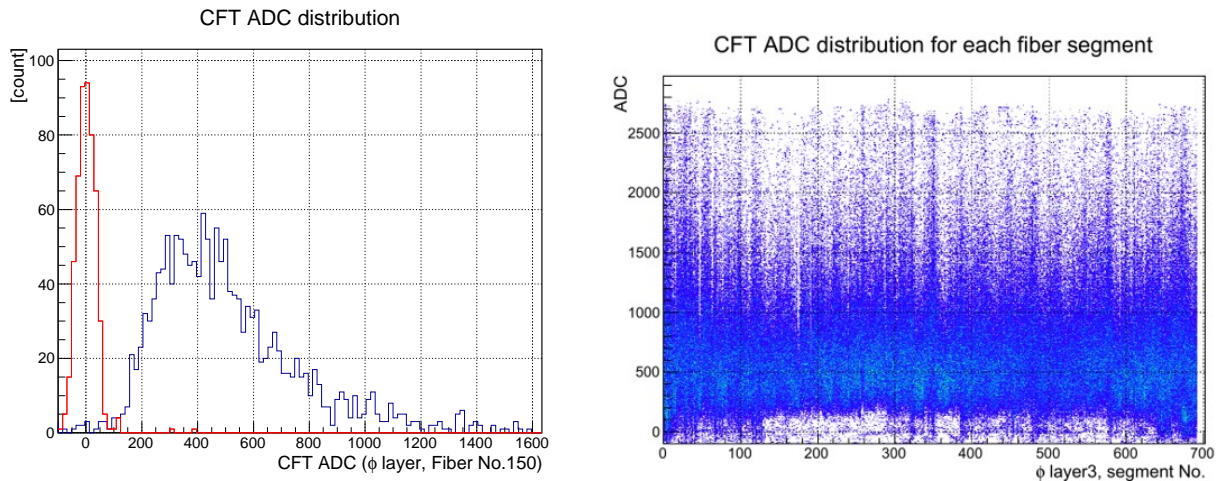


Figure 4.3: Left figure shows ADC spectrum of CFT straight first layer for cosmic ray after subtracting its pedestal shown with red line. Right figure shows a scatter plot between CFT segment and ADC distribution. ADC value of zero corresponds to the peak position of the pedestal.

Although there are some differences in the peak value between the fiber segments, the typical gain is 30 [ADC channel/p.e.]. By using this value, a typical value of the number of photoelectrons is obtained to be 13 p.e.

Calibrations of ADC for the energy deposit in the fiber is discussed in the chapter of *pp* scattering experiment (chapt. 5).

#### 4.2.2 CFT TDC

A typical TDC distribution of CFT is shown in the Figure 4.4, which is taken with a common stop method.

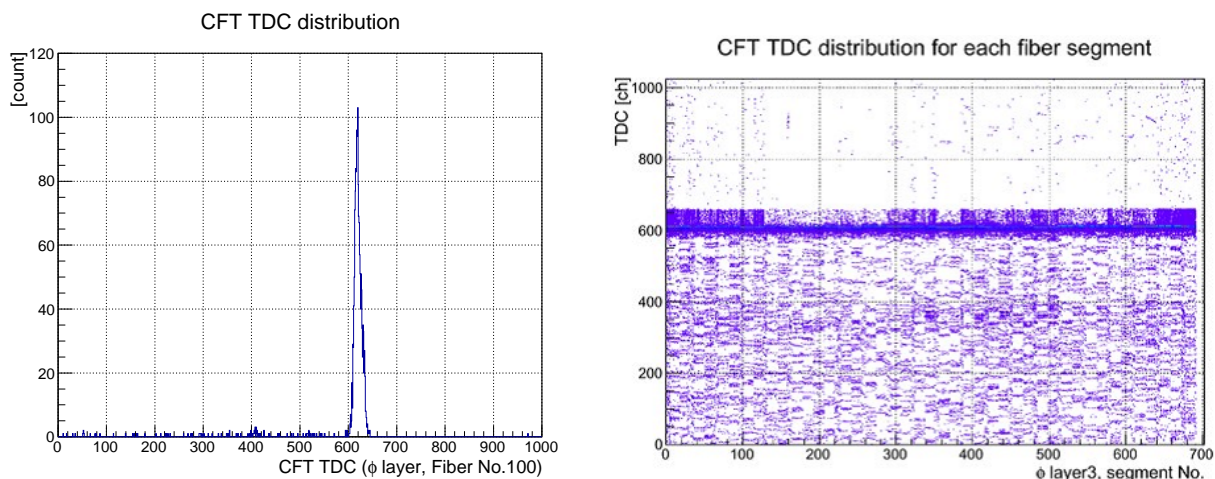


Figure 4.4: Left figure shows the TDC distribution of one fiber segment for cosmic ray. Right figure shows the scatter plot between the CFT segment and the TDC for the straight layer 2.

In the TDC distribution, there are also some events after the main peak, which are caused by after pulse in MPPC, signal reflection in the readout cable, and so on.

The cosmic rays events distribute as a peak around a TDC value of 600 channel. However, each peak value is different due to the cable length of each channel.

Since the number of channels to be handled is large, and their TDC peak values vary channel by channel, “*ctime*” is introduced in order to simplify the operation and analysis. We define the *ctime* as follows.

$$ctime = (TDC - TDC_{peak}) \times 1[ns/TDCch] \quad (4.1)$$

The distribution of *ctime* is shown in Figure 4.5.

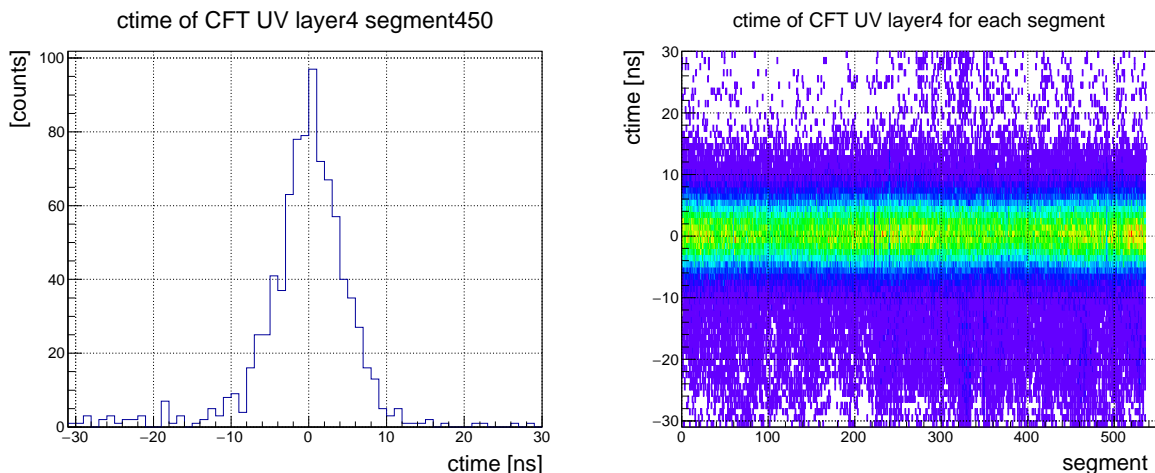


Figure 4.5: Left figure shows a scatter plot between CFT segment and  $ctime$  for the spiral layer 4. In order to identify the fiber hit event, the  $ctime$  is required to be within  $\pm 20$  ns as shown in the right figure.

In order to identify the fiber hit event, the  $ctime$  is required to be within  $\pm 20$  ns in the following analysis. The time resolution of CFT is discussed later in chapter 5.

### 4.2.3 CFT hit pattern

As shown in Figure 4.3 and 4.4, data from almost all the fibers were taken correctly. In order to evaluate the efficiency of the fiber readout quantitatively, we checked the hit pattern distribution of each layer using cosmic rays.

Figure 4.6 shows the hit pattern distributions of the CFT straight layers for cosmic rays, after selecting the events with TDC values around the peak within  $\pm 20$  ns. The hit pattern distributions corresponding to the cosmic ray distribution, which depends on  $\cos^2\theta$ , was observed. The hit pattern distributions for the spiral layers are also shown in Figure 4.7. It is uniformly distributed because the hit segment changes in the  $z$  direction. Therefore, the number of counts became slightly smaller at both ends of  $z$ .

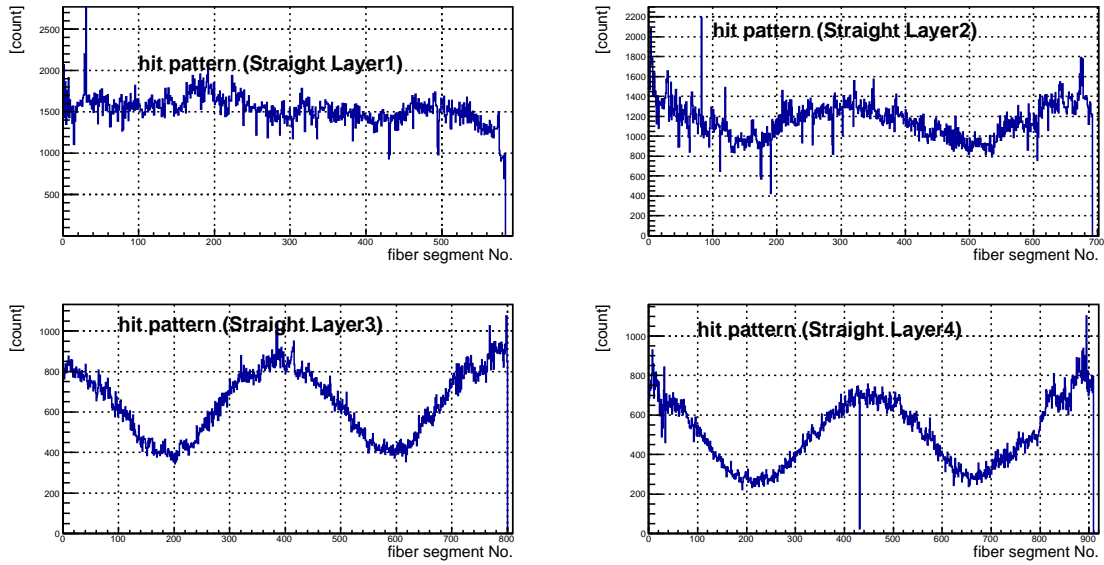


Figure 4.6: Hit pattern distributions of the CFT straight layers for cosmic rays. Cosmic ray distribution was confirmed from the hit pattern of straight layers.

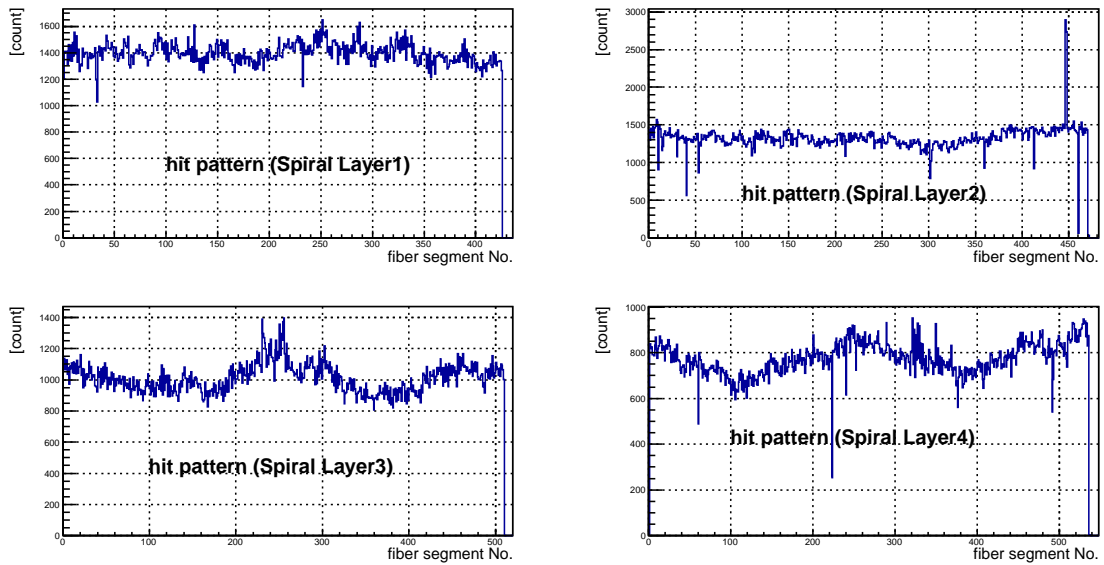


Figure 4.7: Hit pattern distributions of the CFT spiral layers for cosmic rays. It is uniformly distributed because the hit segment changes in the  $z$  direction. Therefore, the number of counts became slightly smaller at both ends of  $z$ .

Locally, there were some segments with a small number of counts. The main reasons for this inefficiency are as follows,

- problems with the MPPC signal,
- problems with the scintillation fiber.

In the case of the MPPC, there was no MPPC signal due to a low operation voltage for. or some troubles in the MPPC, the readout cable or the circuit happened. There is a possibility of recovering if the cause is identified and resolved.

In the case of the fiber, scintillation photons in the fiber can not reach the MPPC. This may be caused by broken or cracked fibers. In order to solve this problem, it is necessary to remake the detector itself. However, it is practically difficult.

The table below shows the number of channels with these problems.

Table 4.2: CFT missing channels

	Total fibers	MPPC trouble	Fiber trouble	small gain	readable
cosmic ray test	4932	10	10	36	4884 (99.0%)
After gain readjustment	4932	10	10	2	4919 (99.7%)

It was found that 99 % of the fibers are correctly read out. Even if there are some fibers which can not be read out, a track can be reconstructed by using other layers.

These missing channels are considered to affect the detection efficiency of CFT. The evaluation of detection efficiency will be discussed later.

### 4.3 CFT Fiber position correction

As mentioned in the fabrication of CFT, there is a deviation between the designed position of the fiber and the actual position. This misalignment causes deterioration of tracking performance. However, by using the actual position of the fibers, tracking performance could be improved. Therefore, we have to know the deviation from the designed position and use the actual position in the offline analysis.

We estimated the actual fiber position from reconstructed cosmic ray track which penetrated all the 16 layers in total. By using the 16 layers, the accuracy of the position estimation at each layer can be improved. In order to correct the fiber position, its designed position was compared with the obtained position from tracking.

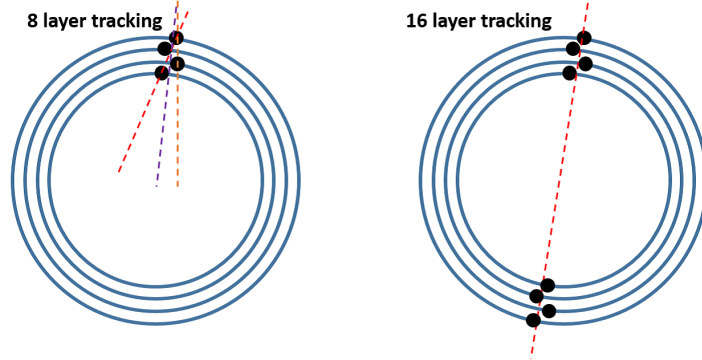


Figure 4.8: By using the 16 layers, the accuracy of the position estimation at each layer can be improved than the tracking using only one side.

The deviation of the fiber position is caused by misalignment of each fiber in the fabrication. Therefore, the correction should be performed fiber by fiber, and also  $z$  dependence should be considered.

#### 4.3.1 CFT Tracking procedure

In order to obtain trajectories with CFT, two stages of tracking are performed as shown in Figure 4.9. At first, a tracking on the  $xy$  plane is performed by using the straight layers. By fitting the hit point of each straight layer with a straight line, the trajectory of the  $xy$  plane can be obtained. From this straight line, the intersection  $\phi(r)$  of the straight line and the CFT layer is obtained. Here,  $\phi(r)$  is the position of the angle  $\phi$  on a circle of radius  $r$ .

As a next step, a tracking on the  $xy - z$  plane is performed by using the spiral layers. The  $xy$  axis is the axis along the trajectory obtained in the  $xy$  plane before. The  $z$  position of each layer is obtained by the hit segment number of the fiber and  $\phi(r)$  as shown in Figure 3.3. The trajectory of the  $xy - z$  plane is also obtained by fitting the hit point of each spiral layer.

In this way, a three dimensional trajectory can be obtained by CFT.

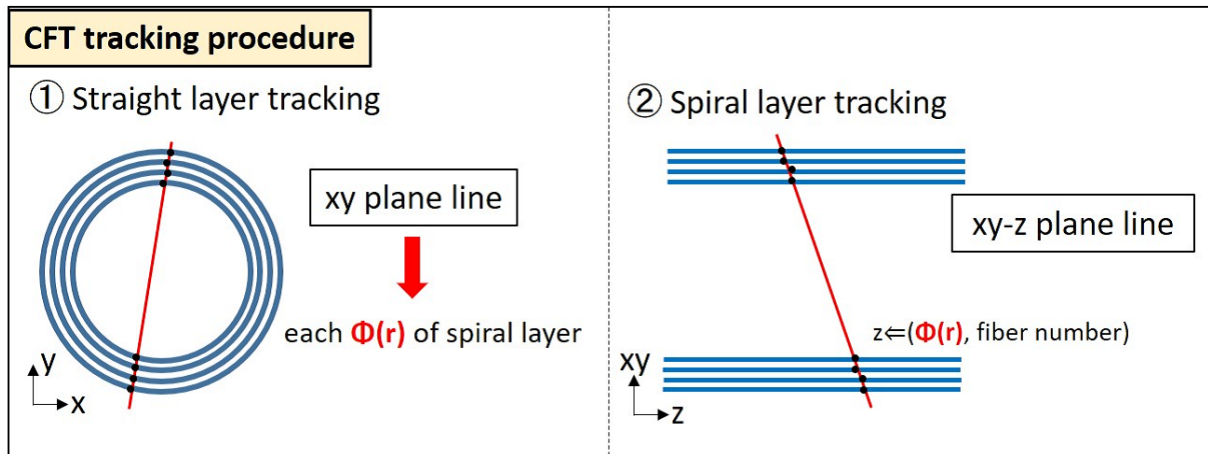


Figure 4.9: In order to obtain trajectories with CFT, two stages of tracking are performed.

As mentioned in the previous section, it is necessary to know the actual fiber position deviated from the design position. Therefore, the residual of each fiber position from the trajectory is obtained using the trajectory obtained with the design position. By changing the fiber positions according to the residuals, we aim to reproduce the actual fiber position. This process was repeated several times to reduce the residuals because the tracking of straight layer and spiral layer is related with each other as shown in Figure 4.10.

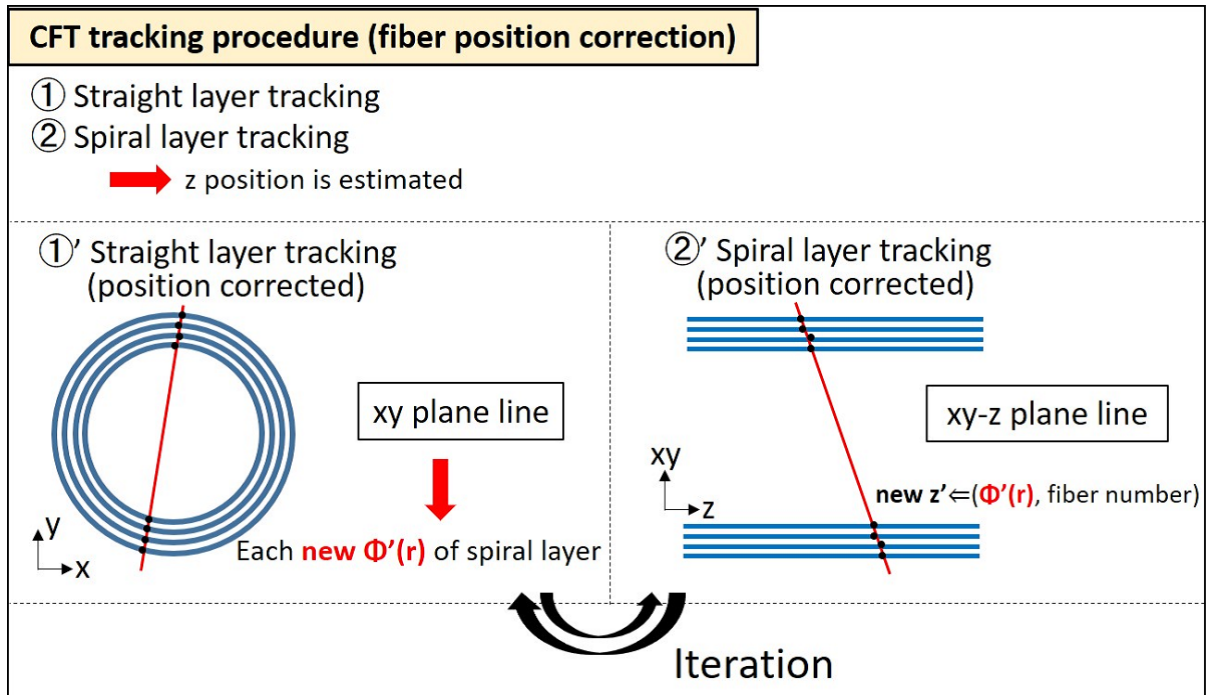


Figure 4.10: In order to reproduce the actual fiber position, the position correction was iterated because the tracking of straight layer and spiral layer is related with each other.

#### 4.3.2 Position correction in Straight layers

The straight layer determines the azimuthal angle ( $\phi$ ). In order to represent the deviation of the fiber position, the azimuthal angle difference ( $d\phi$ ) between the original designed value and the reconstructed value from the tracking as shown in Figure 4.11 is introduced.

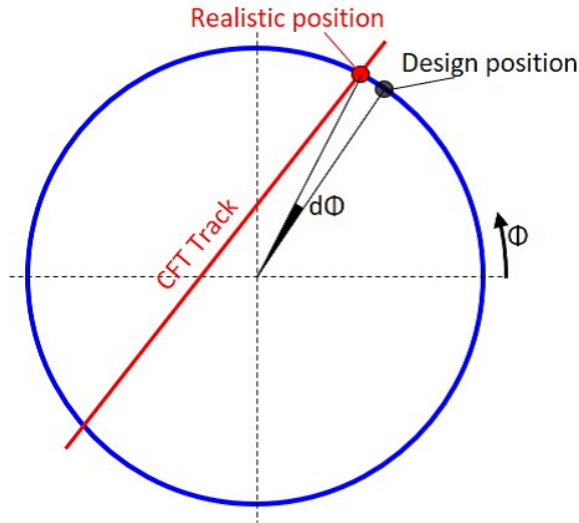


Figure 4.11: This illustration shows the definition of  $d\phi$  in the  $xy$  plane, where  $d\phi$  represents the difference between the  $\phi$  of designed position and the  $\phi$  estimated from tracking.

Figure 4.12 shows the  $z$  dependence of  $d\phi$  for each straight layer, where  $z$  is the position in the  $z$  direction. The position of  $z = 0$  corresponds to the start position of the active region in the upstream point of CFT.

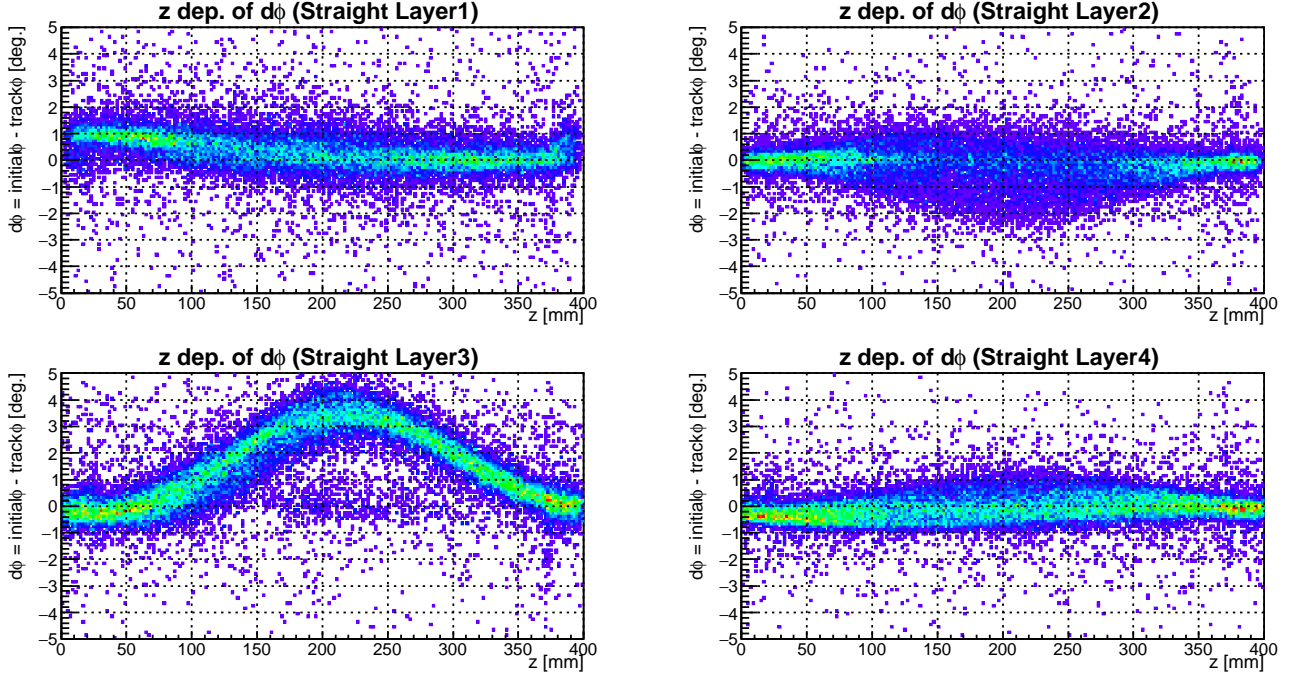


Figure 4.12: Scatter plots between  $d\phi$  defined in the Figure 4.11 and  $z$  position for each straight layer. The  $d\phi$  of all segments are filled in these figures.  $z$  is the position in the  $z$  direction obtained from the track.

If the fiber position in analysis matches the actual fiber position,  $d\phi$  should be 0.

From Figure 4.12, it is seen that the deviation is small at the both edges of the active region in  $z$  direction, where the fibers are fixed to the frames ( $z = 0$  and 400 mm). On the other hand, it becomes large at the center region.

In the straight third layer, the deviation became maximum at the center among all the fibers. However, the width of the  $d\phi$  does not change with the  $z$  position very much. This means that the fibers are shifted to the same direction as shown in Figure 4.13. The size of the deviation is rather large. The deviation of 4 degrees corresponds to 5 mm considering its radius.

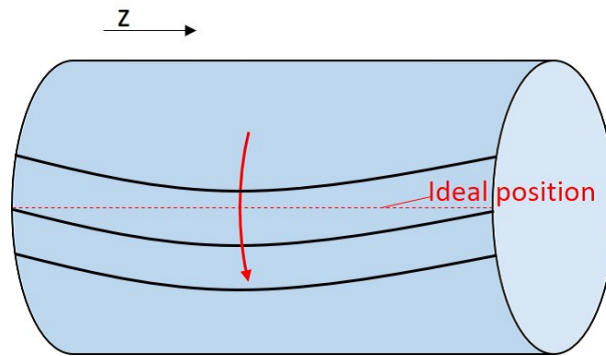


Figure 4.13: This illustration explains the result of the residual of the straight third layer shown in Figure 4.12. The deviation became maximum at the center region in  $z$  direction. This result means that the fibers are shifted to the same direction for this layer.

On the other hand, Layer 2 and Layer 4 appear to have some components. Actually, since each fiber was assembled on by one by hand, the fiber positions may vary randomly. Figure 4.14 shows  $d\phi$  distribution for the function of  $z$  for straight layer 2 selecting the fiber segments. The shape of deviation depends on the fiber segment even in the same layer.

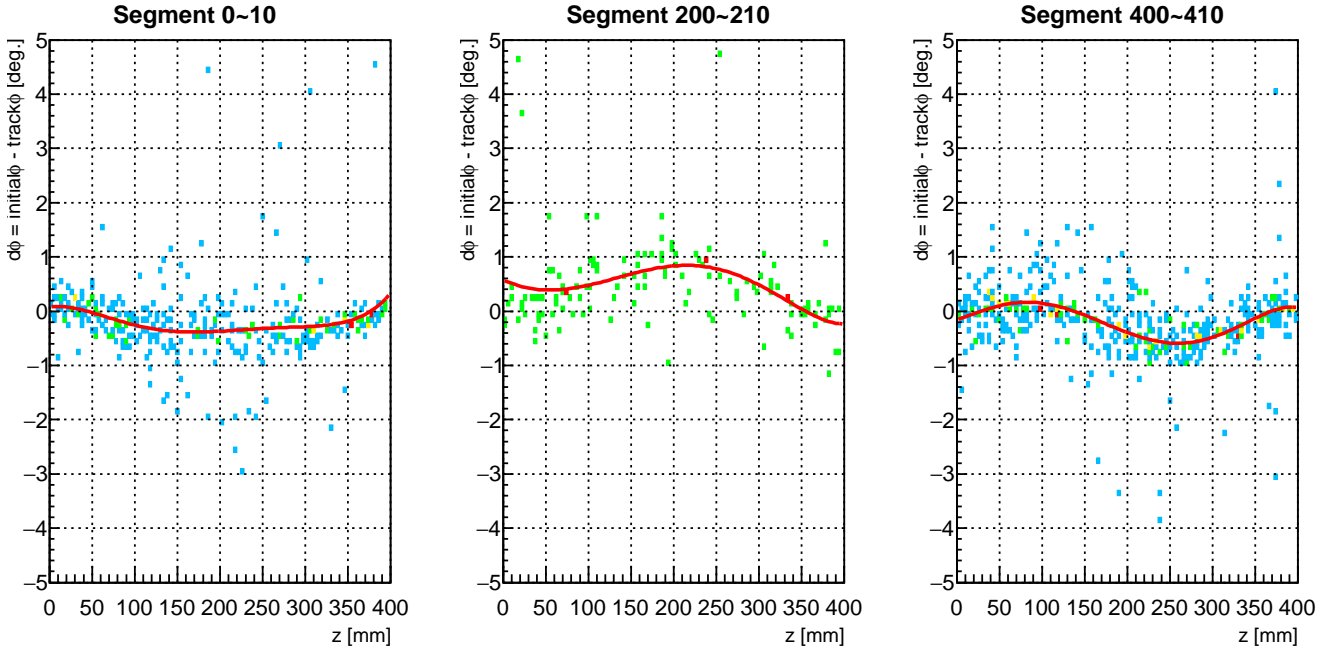


Figure 4.14: Scatter plots between  $d\phi$  and  $z$  position for straight layer 2 selecting the fiber segment number. The shape of deviation depends on the fiber segment even in the same layer.

It is the important point in analysis of this measurement that the position correction of the fibers were performed for several fibers together due to the small statistics. Here, the residual for each 10 segments of fibers were treated together. In the future, a sufficient statistics of cosmic ray measurement is estimated to resolve this problem.

By fitting the scatter plot with a certain function as shown in the Figure 4.12 for each segment, the position deviation is corrected according to  $d\phi$  as a function of the  $z$  position. Here, a fifth-order polynomial function is adopted to reproduce the  $z$  dependence reasonably.

Figure 4.15 shows the  $z$  dependence of  $d\phi$  after the position correction. From this figure, the position correction was successful and  $d\phi$  distributes around zero.

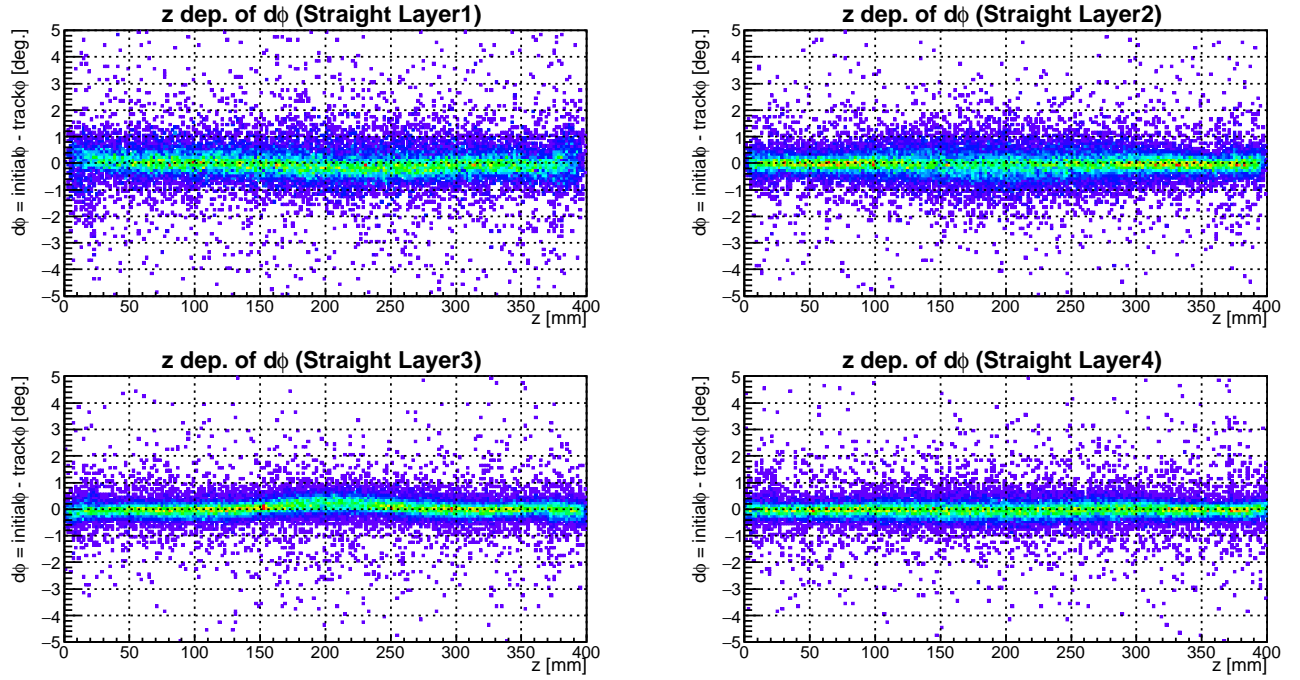


Figure 4.15: Scatter plots between  $d\phi$  and  $z$  position for each straight layer after position correction of straight layer. The position correction was succeed and  $d\phi$  distribute around zero.

As shown in Figure 4.15, the big deviation disappears. This means that the actual fiber position was reproduced. Furthermore, I also checked segment dependence of  $d\phi$ . In the straight layer, the segment number corresponds to the  $\phi$ . Figure 4.16 shows the  $\phi$  dependence of the deviation, which corresponds to the segment dependence of the fiber . Figure 4.16 shows the  $\phi$  dependence of  $d\phi$  after correction.

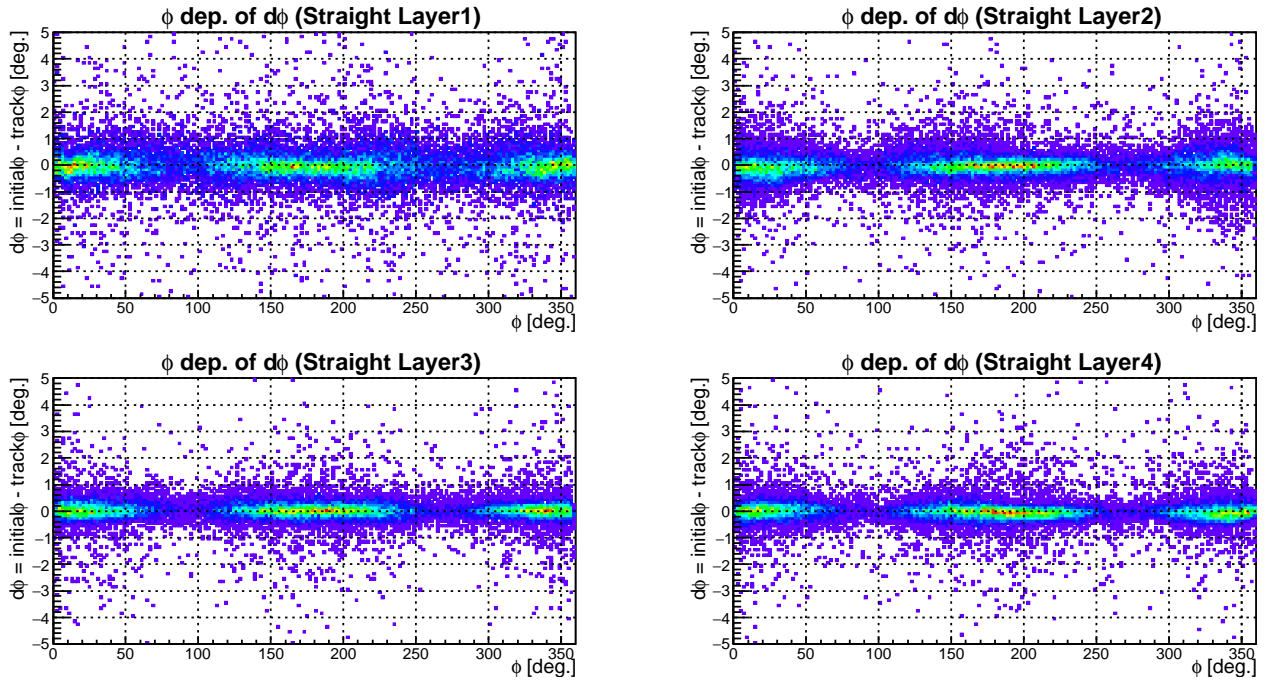


Figure 4.16: Scatter plots between  $d\phi$  and  $\phi$  position for each straight layer after position correction of straight layer. In addition to the  $z$  dependence, the  $\phi$  dependence was also corrected.

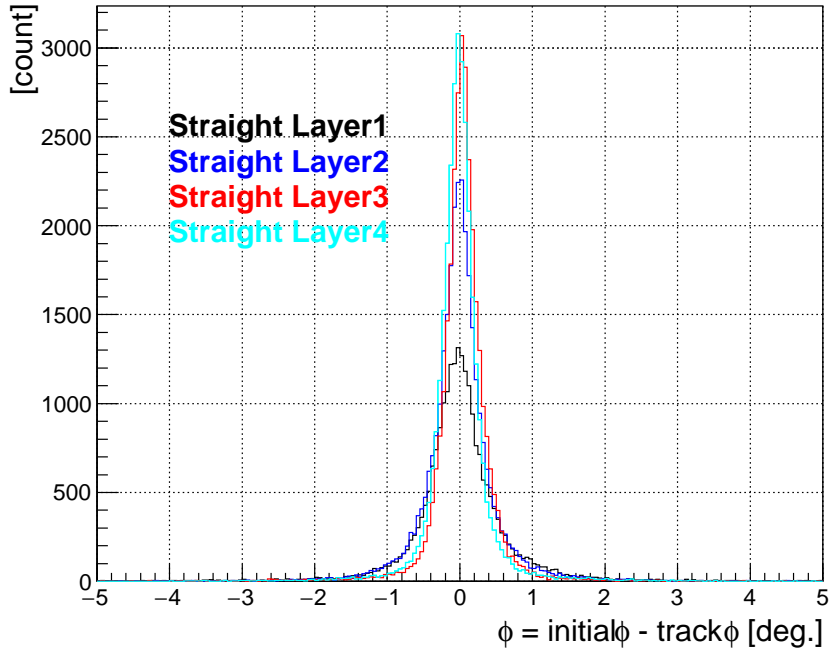


Figure 4.17: Residual distribution of  $d\phi$  in CFT straight layer.

Since the fiber position was performed fiber by fiber, the  $\phi$  dependence was also corrected.

### 4.3.3 Spiral layer position correction

The fiber position correction was performed similarly for the spiral layer.

Like the straight layers, the position deviation should also be obtained fiber by fiber for the spiral layers. We define  $dz$  as the deviation of fiber position in  $z$  direction as follows,

$$dz = z_{design}(\phi) - z_{track}(\phi). \quad (4.2)$$

Each  $z$  can be calculated from the azimuthal angle  $\phi$  obtained from the tracking with the straight layers and the hit segment number of the spiral hit fiber as shown in Figure 3.2.  $z_{track}$  is a position obtained from the CFT tracking, and  $z_{design}$  is a designed position.

Figure 4.18 is the  $dz$  distribution obtained by using cosmic ray data.

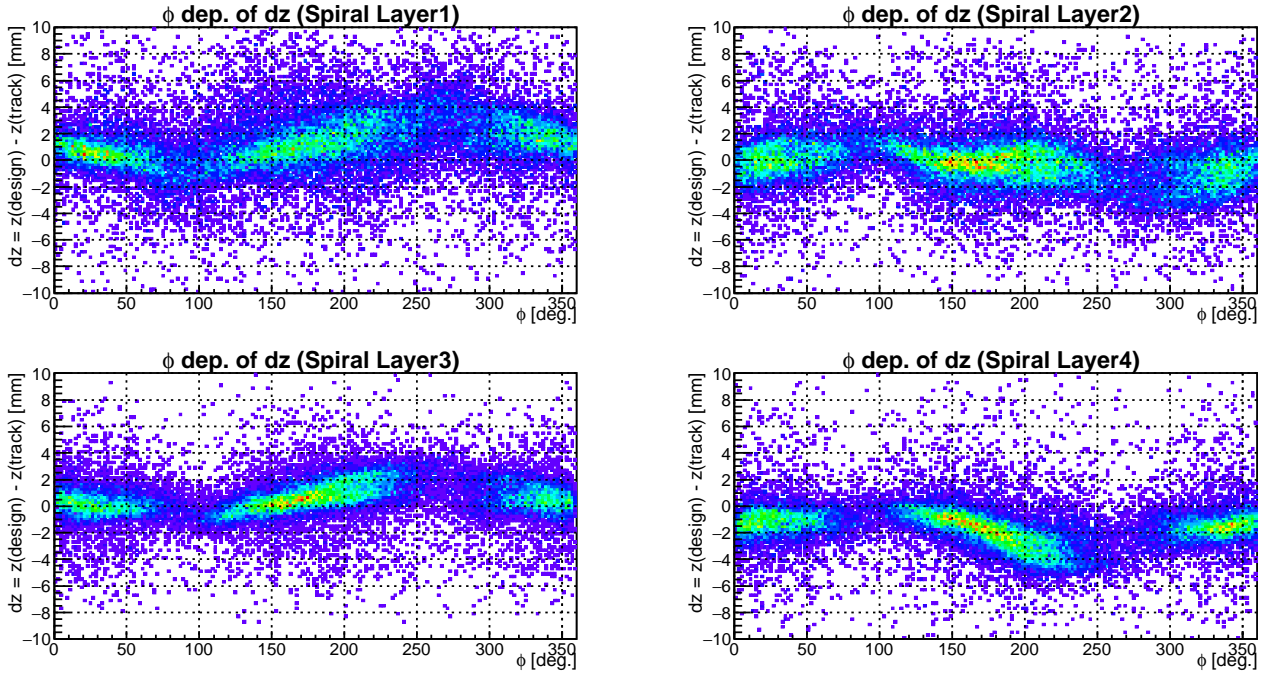


Figure 4.18: Difference between the design and the actual  $z$  position in each CFT spiral layers. The straight layer is used after fiber position correction by cosmic ray data, and the  $\phi$  position is determined. Fitting was performed with fifth-order polynomial functions in the figures.

We fitted this  $\phi$  dependence of  $dz$  with a fifth-order polynomial function. The design position was modified according to the fitting result, and the fiber position was corrected so as to reproduce the actual position.

Here, the residual for each 10 segments of fibers were treated together like the correction of straight layer.

The corrected  $\Delta z$  distribution is shown in Figure 4.19.

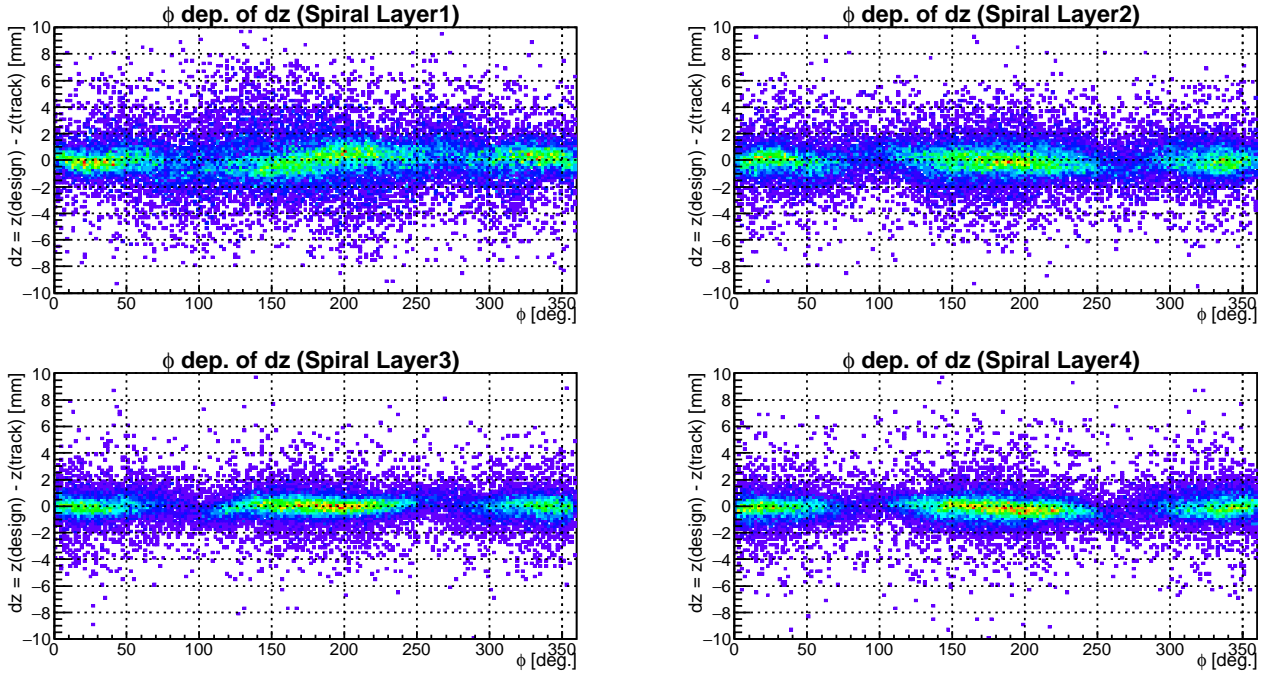


Figure 4.19: Scatter plots between  $\phi$  position and  $dz$  after fiber position correction. The position correction was succeed and  $dz$  distribute around zero.

Figure 4.20 shows the dependence of the corrected  $dz$  distribution as a function of  $z$ . It was confirmed that there is no dependence on the  $z$  direction and the residuals distribute around 0.

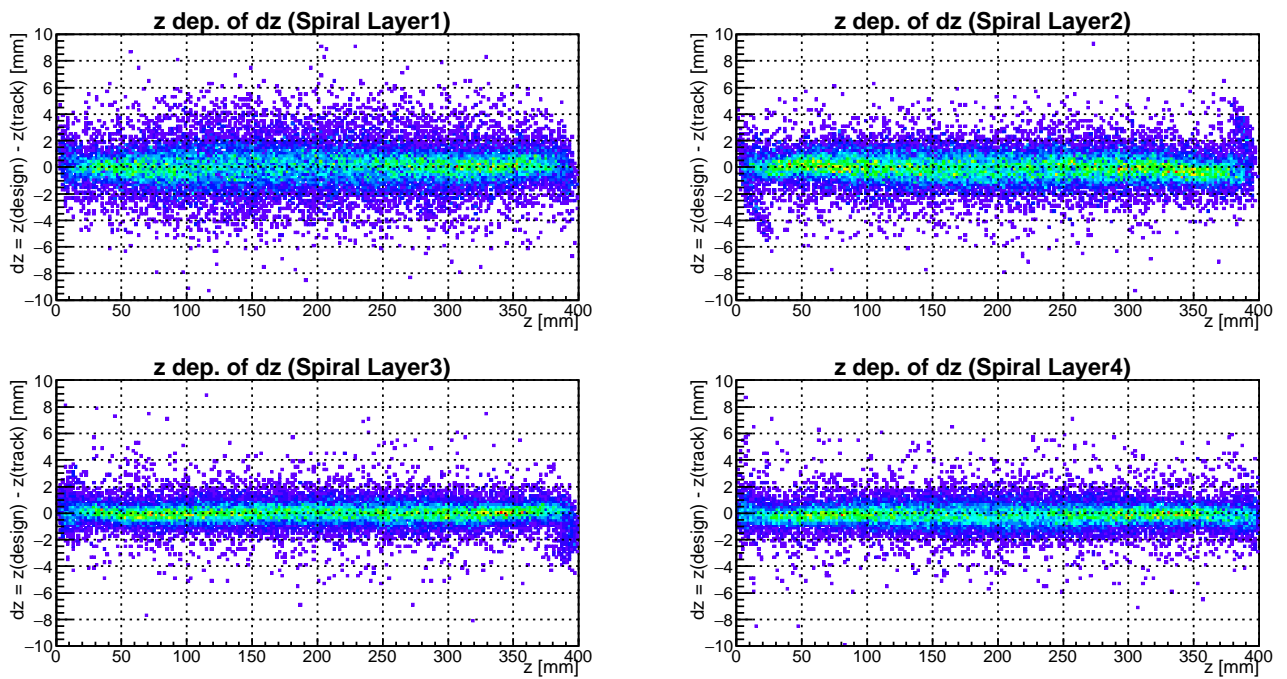


Figure 4.20: The  $z$  dependence of  $dz$  distribution after fiber position correction.

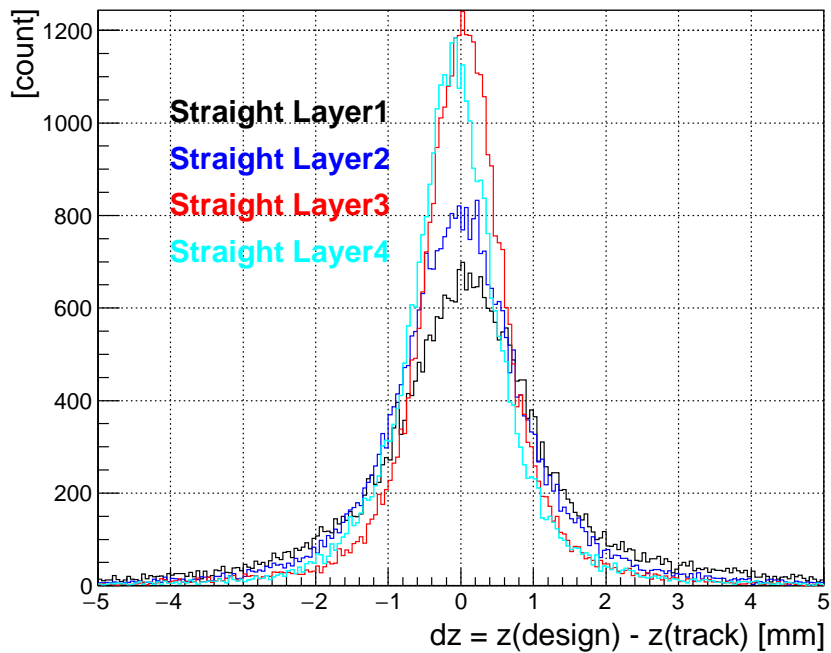


Figure 4.21: Residual distribution of  $dz$  in CFT spiral layer.

#### 4.3.4 Results of position correction

As an index showing the result of fiber position correction, the  $\chi^2$  distribution and the spread of residuals are discussed in this section.

Figure 4.22 shows the  $\chi^2$  distributions of the CFT tracking with the straight layers and the spiral layers. Each figure shows the distributions before and after the fiber position correction.

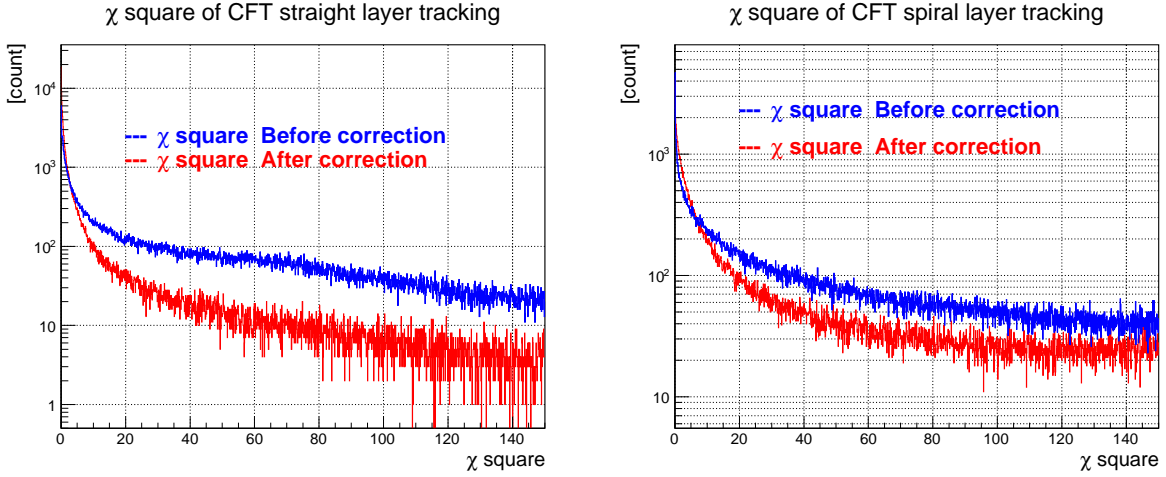


Figure 4.22: Left and right figures show  $\chi^2$  distribution of CFT tracking of the straight layer and the spiral layer, respectively. Each figure shows the distribution before and after the fiber position correction.

The spreads of  $d\phi$  and  $dz$  after  $z$  position correction were obtained as Table 4.3.

The spreads of  $d\phi$  and  $dz$  were also calculated by considering the size of the fiber. From the fiber diameter of 0.75 mm, the size along the  $\phi$  direction of one fiber can be calculated as  $\frac{0.75}{2\pi r} \times 360$  [degree]. The position resolution corresponds to this value divided by  $\sqrt{12}$ . The spread of  $z$  by one fiber in the spiral layer is obtained to be  $\frac{0.75}{\sin(\text{tilt angle})}$  [mm].

The spread of  $z$  expected by the above calculation is summarized in Table 4.3.

Table 4.3: The spreads of  $d\phi$  and  $dz$  of CFT tracking

Position resolution of Straight layer	Layer1	Layer2	Layer3	Layer4
Calculated $\sigma_{d\phi}$ [degree]	0.24	0.21	0.18	0.16
Measured $\sigma_{d\phi}$ [degree]	0.38	0.33	0.24	0.23

Position resolution of Spiral layer	Layer1	Layer2	Layer3	Layer4
Calculated $\sigma_{dz}$ [mm] (Spiral layer)	0.46	0.51	0.55	0.59
Measured $\sigma_{dz}$ [mm] (Spiral layer)	0.96	0.86	0.59	0.68

By comparing these, the actual spreads were generally larger, although these values were roughly of the same order. The reasons for this difference is considered to be that the position correction of the fibers were performed for several fibers (10 fibers in the correction of spiral layer) together due to the small statistics. In addition, it may also be considered that the displacement in the direction of the radius  $r$  was not considered in this position corrections. Especially in the spiral layer, the structure tends to be deformed in the  $r$  direction.

#### 4.4 Angular resolution for cosmic ray

The angular resolution of CFT for cosmic ray is evaluated in this section. However, an evaluable angular region was limited due to the cosmic ray distribution in which the vertical direction is dominated. Figure 4.23 shows the  $\theta$  distribution obtained from the CFT tracking in the cosmic ray measurement. The  $\theta$  of 90 degrees corresponds to the vertical direction in the laboratory frame.

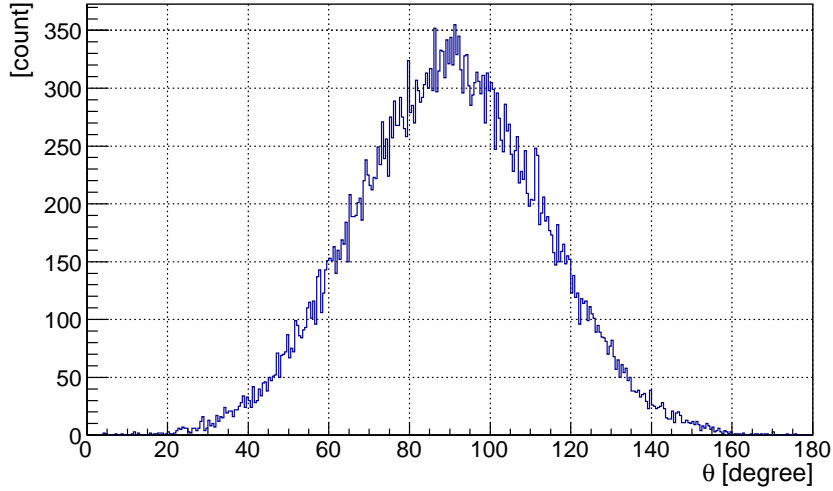


Figure 4.23: Tracked  $\theta$  distribution for cosmic ray. It concentrates the vertical direction due to the cosmic ray distribution. The  $\theta$  of 90 degrees corresponds to the vertical direction in the laboratory frame.

For the evaluation of the angular resolution of the CFT tracking, we used the sum of the two angles ( $\theta_1 + \theta_2$ ), where  $\theta_1$  is the angle of the cosmic ray track measured only by the upper part of CFT, and  $\theta_2$  only by the lower part of CFT. respectively. The sum  $\theta_1 + \theta_2$  should be 180 degree. Figure 4.24 shows the  $\theta_1 + \theta_2$  distribution for cosmic ray. In order to evaluate the angular resolution with the close condition with the  $\Sigma p$  scattering experiment, we selected only the trajectories passing through the inside of a circle with a radius of 20 mm centered at  $(x, y) = (0, 0)$  in  $x$ - $y$  plane corresponding to the target size of the  $\Sigma p$  scattering experiment.

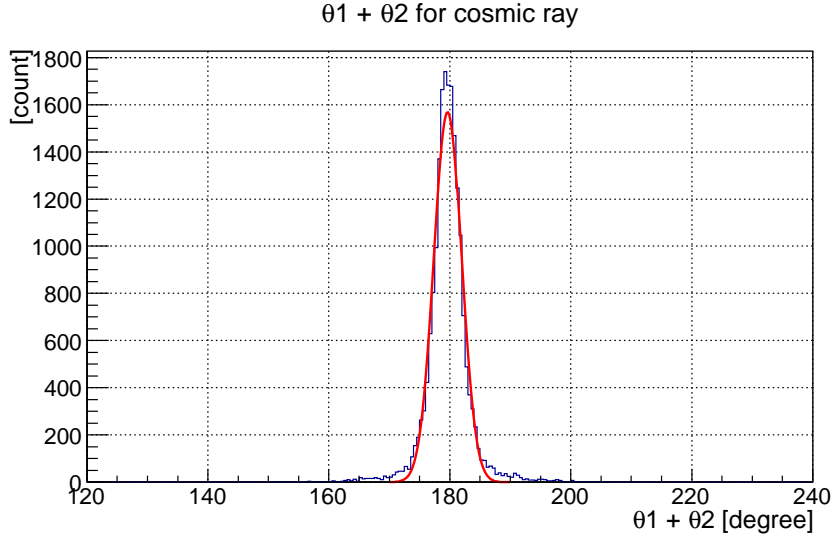


Figure 4.24: The  $\theta_1 + \theta_2$  distribution for cosmic ray. Because the same straight trajectory is tracked at different two points, the  $\theta_1 + \theta_2$  should be 180 degree. It concentrates the vertical direction due to the cosmic ray distribution. The  $\theta$  of 90 degrees corresponds to the vertical direction in the laboratory frame.

The spread of the  $\theta_1 + \theta_2$  was obtained to be 2.30 degrees ( $\sigma_{\theta_1+\theta_2}$ ). Assuming that the angular resolution is the same for both tracks, that is  $\sigma_{\theta_1} = \sigma_{\theta_2} = \sigma_\theta$ , the spread of the  $\theta_1 + \theta_2$  should be  $\sqrt{2}\sigma_\theta$ , where  $\sigma_{\theta_1}$  and  $\sigma_{\theta_2}$  are the angular resolutions of  $\theta_1$  and  $\theta_2$ , respectively. From this calculation,  $\sigma_\theta$  was obtained to be 1.63 degree. This result satisfies the requirement of 2 degrees ( $\sigma_\theta$ ) for the  $\Sigma p$  scattering experiment.

The center position of the  $\theta_1 + \theta_2$  peak was 179.6 degree, which almost agreed with 180 degree. However, the systematic error of  $\theta$  could not be discussed with only this cosmic ray data. The systematic error of  $\theta$  is discussed in the next chapter together with the evaluation for the tracking of protons. Since the main measuring object of CFT in the  $\Sigma p$  scattering experiment is the proton, the angular resolution should be evaluated with protons taking into account the effect of multiple scattering. Therefore we also evaluated the angular performance for protons in a test experiment discussed in the next chapter.

## 4.5 Operation procedure

Based on the calibration method performed above, I considered the procedure for the operation in the measurement experiments such as the  $\Sigma p$  scattering experiment.

Because the CFT has the adjustment mechanism of the fiber's tension, the behavior of the deviation of the fiber position is possible to be change for each adjustment or installation. Therefore, the commissioning data is necessary for each measurement condition like this cosmic ray measurement.

## Chapter 5

# Performance evaluation of CATCH by a beam experiment

### 5.1 Overview

In order to evaluate the performance of CATCH, proton-proton ( $pp$ ) and proton-carbon ( $pC$ ) scattering experiment was performed in January 2017, at Tohoku University Cyclotron Radio Isotope Center (CYRIC). In order to make the experimental condition as equivalent as possible to the  $\Sigma p$  scattering experiment, an 80 MeV proton beam is irradiated on a polyethylene ( $\text{CH}_2$ ) target and a hydrogen gas target installed inside CATCH, and the emitted protons were measured with CATCH.

### 5.2 Experimental setup and conditions

The experimental setup is shown in Figure 5.1

Since the sensitive area of CATCH is 400 mm long in the beam direction, it is to be checked whether there is any difference in performance for different  $z$  positions. Therefore, the measurements were performed at three target positions ( $z = 54, 126, 208$  mm) in the  $z$  direction. Here, the upstream end of the CFT active region is at  $z = 0$ , and the downstream end is at  $z = 400$ . The target was 800  $\mu\text{m}$  thick, sufficiently thin for evaluating the tracking performance of CFT.

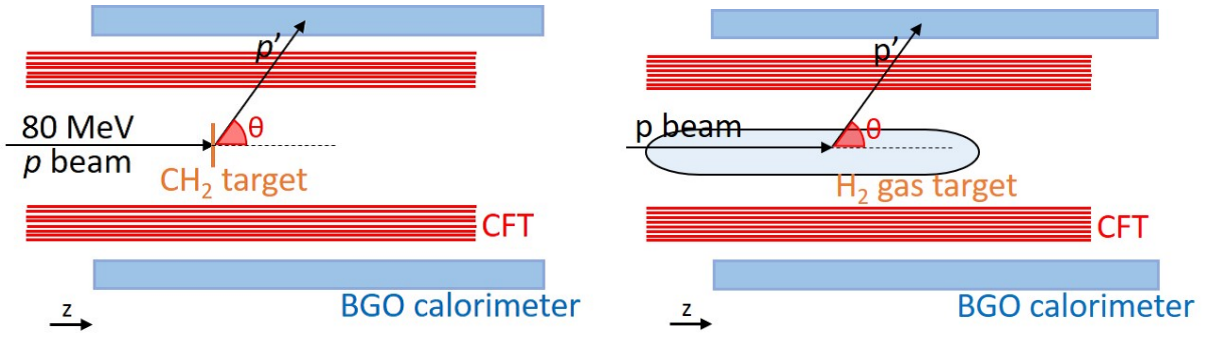


Figure 5.1: Setup for the  $pp$  and  $pC$  scattering experiment with  $\text{CH}_2$  target and CATCH system is shown in the left figure. The one with  $\text{H}_2$  gas target is shown in the right figure.

The energy of the proton beam we used was the maximum energy available for CYRIC. In the  $\Sigma p$  scattering experiment, it is estimated that CATCH detects protons with continuous energies up to about 150 MeV, but we first evaluated it with proton energies in the usable range.

The trigger signal is basically the same as the one for the cosmic ray measurement described above. The difference from the cosmic ray measurement was that we used the RF signal which synchronized with the beam incident timing.

As an additional point, the RF signal was used to select the event caused by irradiating beam.

Before the data taking, the Beam size was checked to be  $5 \times 10 \text{ mm}^2$  by using a ZnS plate which shows a beam profile by emitting light from beam irradiation.

The experimental conditions are summarized in Table 5.1.

Table 5.1: Experimental condition of CATCH test measuring protons

setup and conditions	Polyethylene ( $\text{CH}_2$ ) target	Hydrogen gas ( $\text{H}_2$ ) target
Target Position	$z = 54, 126, 208 \text{ mm}$ change position with one target	$z = 0 \sim 300 \text{ mm}$ continuously distributed
Target Thickness	$800 \mu\text{m}$	$300 \text{ mm}$
Beam Energy	$78.5 \text{ MeV}$	
Beam Size	About $5(x) \times 10(y) \text{ mm}^2$	
Beam Intensity	About $0.05 \text{ nA}$	
Trigger	CFT $1^{\text{st}} \times 2^{\text{nd}}$ straight layer $\times$ RF signal	
Beam time	$3.5 \text{ days}$	

### 5.3 Analysis and evaluation procedure

Figure 5.2 shows the procedure for deriving the scattering cross section. The scattering angle  $\theta$  of the scattered protons was obtained from the trajectory measured by CFT, and its kinetic energy was measured by CFT and the BGO calorimeter.  $\Delta E$  is obtained by using the scattering angle  $\theta$  and the kinetic energy  $E_{p'}$ , then the reaction was identified.

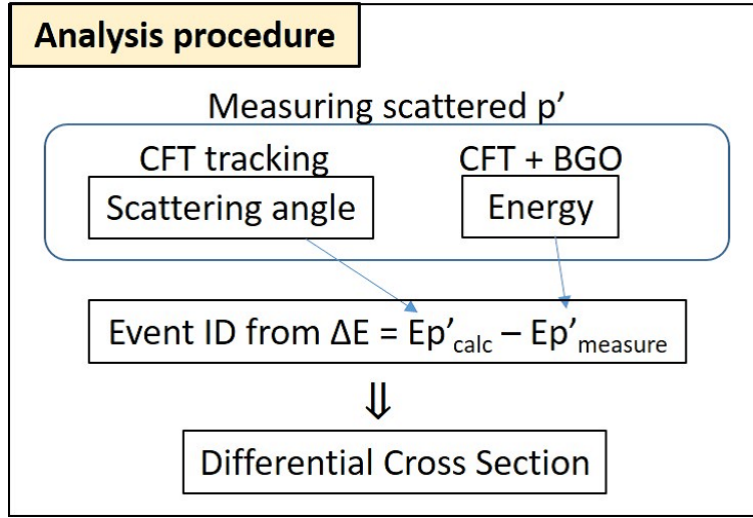


Figure 5.2: Analysis procedure to derive the scattering cross section with CATCH.

The emitted protons from  $pp$  and  $pC$  scatterings were used for energy calibration of CFT and the BGO calorimeter. The energy calibration was performed by comparing the energy of the scattered proton calculated from  $\theta$  obtained by CFT tracking and the measured proton energy corresponding to the energy deposit on the detector. For this purpose, CFT tracking is necessary and it also directly affects the calibration accuracy. Therefore, tracking performance of CFT was evaluated at first. After the energy calibration, the energy resolution of BGO and CFT was evaluated.

From the  $\Delta E$  distribution, the reaction identification was performed. In order to derive the scattering cross section from the number of the identified events, the detection efficiency and the acceptance of CATCH were necessary. These efficiencies were obtained from data analysis and simulation.

In the data analysis, the following items are examined:

- CFT tracking performance,
- Energy calibration and resolution,
- $\Delta E$  resolution,
- Efficiency of the CATCH system,
- Systematic error in the cross section.

The analysis methods and results of each item will also be described in the following sections. By evaluating the above performances, it is sufficient to evaluate the  $\Sigma p$  scattering experiment.

## 5.4 CFT tracking performance

The tracking performance of CFT for protons is evaluated by using in this section. The method of the tracking is described in section 3.3.1.

### 5.4.1 angular resolution

We have mentioned that the CFT fiber positions were corrected with the analysis of the cosmic ray data. In this section, the angular resolution after the position correction was evaluated with  $pp$  scattering events.

In the  $pp$  scattering events, two protons are emitted from the target. The sum of the two emission angles is 90 degrees in the non-relativistic kinematics.

The evaluable angular region was limited by the energy of two emitted protons depending on the scattering angle strongly. Both energies were required to be large enough to pass through the CFT layers. Figure 5.3 shows a  $\theta$  distribution of  $pp$  scattering when CFT detected two trajectories.

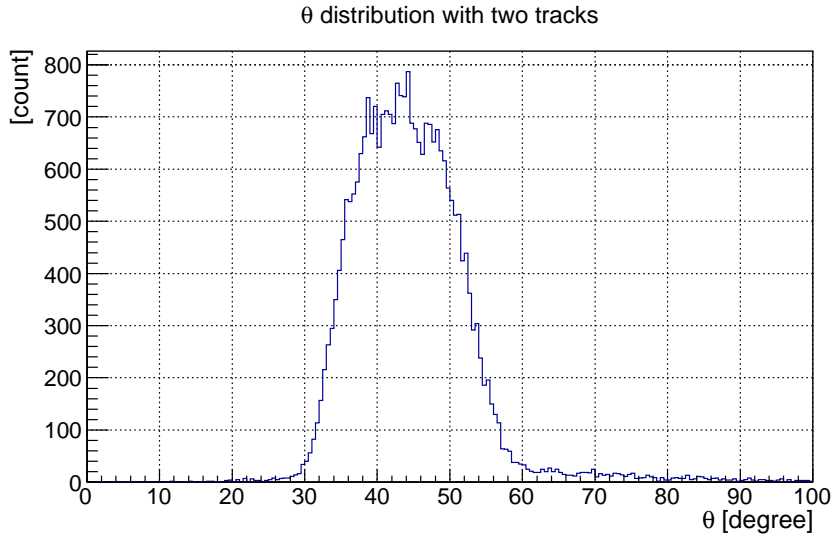


Figure 5.3: The  $\theta$  distribution of  $pp$  scattering when CFT detected two trajectories. The evaluable angular region was limited by the energy of two emitted protons.

Figure 5.4 shows a schematic drawing of  $pp$  scattering. In this figure,  $\theta_1, \theta_2$  represent the emission angles of the two protons.

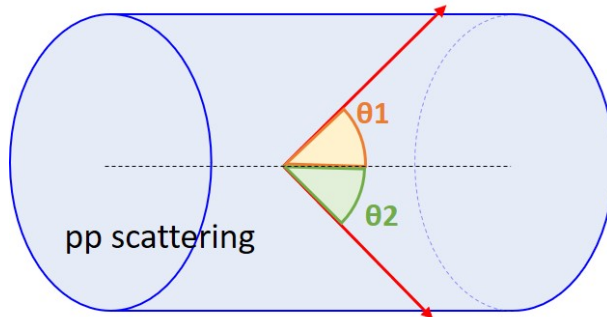


Figure 5.4: The sum of the two emission angles is 90 degrees in the non-relativistic kinematics.  $\theta_1, \theta_2$  represent the emission angles of two protons.

Left figure in Figure 5.5 shows the opening angle obtained from the experimental data. In addition, for the purpose of comparison, a simulation result is also shown in the right figure of Figure 5.5. In the simulation, the material of the CFT fiber was taken into account. The wider distribution of the measurement is considered to be caused by imperfect fiber alignment as described in the followings.

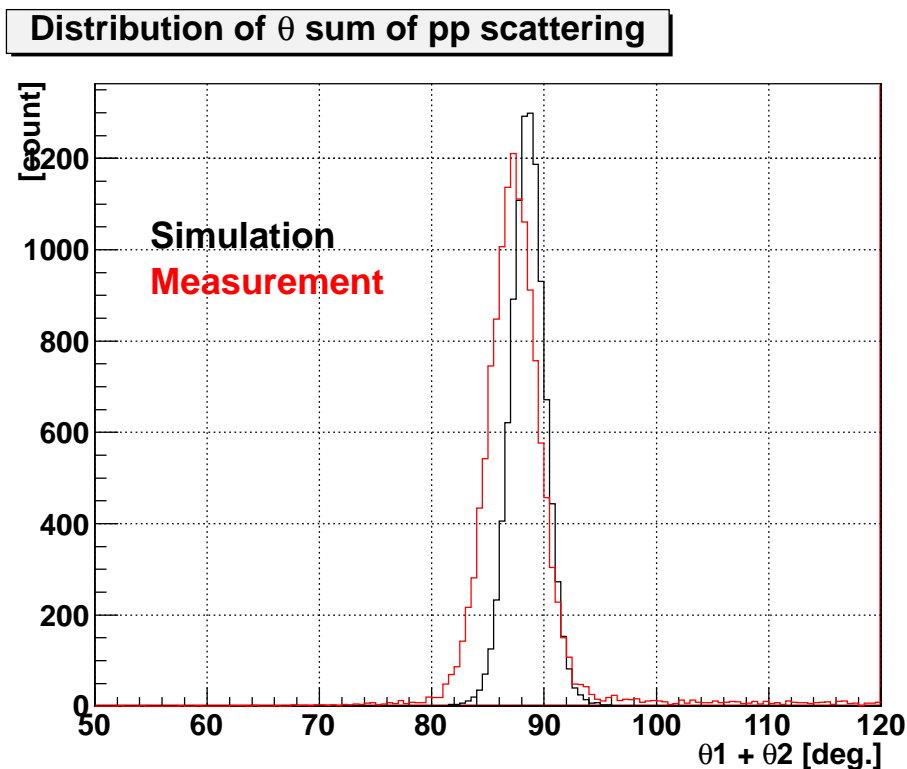


Figure 5.5: The distributions with a red line and a black line show the opening angles of the  $pp$  scattering from the experimental data and the simulated result, respectively.

Assuming that the angular resolution is the same for both tracks, which is the same assumption with the evaluation in the cosmic ray measurement, the spread of the opening angle ( $\theta_1 + \theta_2$ ) should be  $\sqrt{2}\sigma_\theta$ . Where  $\sigma_{\theta_1}$  and  $\sigma_{\theta_2}$  are the angular resolutions of  $\theta_1$  and  $\theta_2$ , respectively.  $\sigma_\theta$  is the angular resolution of the CFT tracking. The angular resolution of CFT was obtained to be  $1.63 \pm 0.01$  degrees. From the simulation which does not consider the fiber position deviation, the angular resolution was obtained to be  $\sigma_\theta = 1.04$  degrees as a result of the same evaluation. The angular resolution is affected by the size of the fiber and its structure, and multiple scattering in the fiber. As for the actual measured value, the fiber position was not corrected completely. We considered that the deterioration came mainly from the fiber position alignment. Although there is a difference, the obtained angular resolution satisfied the requirement of  $\sigma_\theta = 2$  degree.

This result was consistent with the one for the cosmic ray data. The forward

angle less than  $\theta \sim 60$  degrees was dominated in the  $pp$  scattering and  $\theta$  around 90 degrees was evaluated in the cosmic rays concentrating. Together with these two evaluations, it was confirmed that the angular resolution satisfied the requirement for almost whole measurable angular region of CFT.

For the absolute value of the opening angle, 88.5 and 87.3 degrees were obtained in the simulation and in the actual measurement, respectively. The difference of these values was  $\Delta\theta_{sum} = 1.3$  degree, which is treated as a systematic error. For one proton track, the systematic error of the angle  $\Delta\theta(\text{systematic})$  is estimated to be about 0.9 degree. This systematic shift of  $\theta$  is considered to cause a peak shift in the  $\Delta E$  distribution for the event identification. However, the magnitude of the  $\Delta E$  shift is estimated to be less than 1.5 MeV, which is sufficiently smaller than the  $\Delta E$  resolution coming from the other parts. Furthermore, because the  $\Delta E$  is evaluated for each angular region, the peak shift does not affect the counting of the scattered events so much. The influence of the CFT tracking accuracy on  $\Delta E$  in the  $\Sigma p$  scattering experiment is discussed again in Chapter 6.

As discussed in chapter 4, the systematic shift of the  $\theta_1 + \theta_2$  was 0.4 degrees for the cosmic ray data. For one track, the systematic errors of  $\theta$  was estimated to be about 0.3 degree. This shift was very small compared to one of the scattering angles of the  $pp$  scattering event. These results suggest that the angles measured by CFT shifted a little to the radial inner direction of CFT as shown in Figure 5.6.

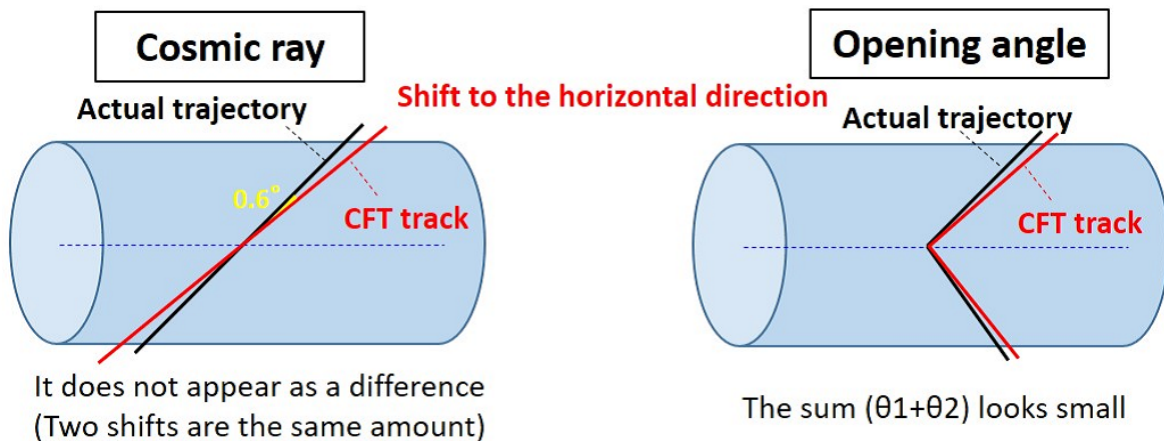


Figure 5.6: The images of the shift of the CFT tracking. The angle seemed to shift a little to the radial inner direction of CFT.

One of the origins of this systematic error is considered to be that the fiber position correction of CFT in the radial direction was not performed. It was found that there was a deviation in the radial direction of the fiber position of about  $\pm 0.5$  mm from the measurement after the fabrication. For example, if the fiber position of all of the CFT layers come 1 mm inside,  $\theta$  of 45 degrees is incorrectly measured to be 44.5 degree. This value is roughly consistent with the obtained systematic error. There is a possibility that it is simply due to the insufficient position correction.

The angular resolution  $\sigma_\theta$  already satisfies our requirement of  $\sigma_\theta < 2$  degree, in future, if the fiber positions could be corrected for each fiber more accurately by taking the cosmic ray data or test beam data, the angular resolution would be further improved.

#### 5.4.2 CFT Time resolution

The time resolution of CFT should be evaluated as one of the most important performances of CFT. Because the time resolution determines the minimum time interval with which events can be separated, it is an important performance especially for the operation under high counting rate environment.

In chapter 3, the CFT time response for cosmic rays was confirmed, but here it will be evaluated for protons. In order to reproduce the situation of the  $\Sigma p$  scattering experiment in this energy range, H<sub>2</sub> gas target data were used. In this condition, protons with continuous energies are incident on a wide region in the z direction of CFT. ( $\phi_1 \times \phi_2 \times \text{RF}$  signal) was used as trigger which also decides stop timing of CFT TDC. The peak width in the CFT TDC is caused by the flight time of protons as well as the time resolution of CFT.

The time distribution of protons from the H<sub>2</sub> gas target detected by CFT for a certain segment was shown in Figure 5.7. The *ctime* is obtained in the same method as the cosmic ray analysis. In this figure, the time distributions before and after the tracking are shown.

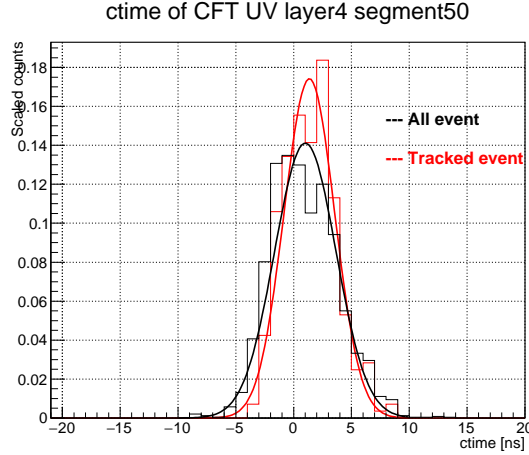


Figure 5.7: Time distribution of protons detected by CFT for a certain segment (segment 50). The black line shows the one before tracking, and the red line shows the only tracked events. These distributions are scaled by the total number of events in order to make the comparison easier.

As an example, in this segment the spread when fitting with a Gaussian function is  $\sigma_t = 2.65$  ns for all events and  $\sigma_t = 2.19$  ns for only tracked events. The tendency that the spread of the time distribution becomes smaller for tracked events are found for all the CFT segments.

As a cause of the tendency, the following can be considered. By selecting only tracked events, low energy protons stopping in the middle of CFT and particles going out of the CFT active region ( $z = 0 \sim 400$  mm) near the MPPC are considered to be excluded.

For the tracked event, the spread of the time distribution is obtained for each segment of each layer, and the averaged value of the spread is shown in Table 5.2.

Table 5.2: Time spread of CFT TDC for tracked protons

$\sigma_{time}$ [ns] of CFT	layer1	layer2	layer3	layer4
Straight layer	1.64	1.74	1.72	1.71
Spiral layer	2.01	1.94	2.03	2.27

At this point, sufficient performance is obtained. Comparing the values in this table, it is found that the spiral layers have larger spread than the straight

layers. Possible reason for this difference is the path length of scintillation light from the hit position to the readout. Between the straight layer and the spiral layer, the path length of light is different due to the fiber arrangement even if the particles hit at almost the same position as shown in Figure 5.8.

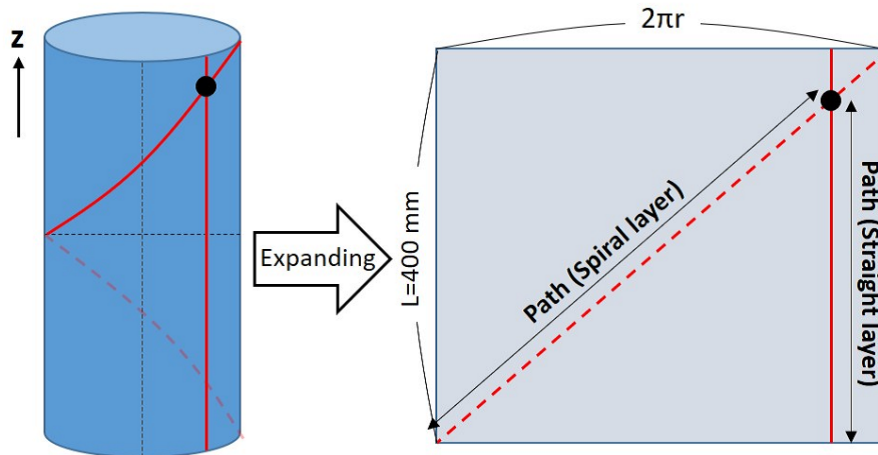


Figure 5.8: Difference between straight and spiral layer of CFT. The black point corresponds to the hit position and the lower side of the figure corresponds to the readout points.

As shown in Figure 5.8, the difference in path length between the straight and the spiral layer depends on the radius of each layer. The ratio of the path length of each spiral layer and the straight layer from the same  $z$  position is summarized in Table 5.3.

Table 5.3: Ratio of the flight path of light between the straight and spiral layers

Path length ratio	layer1	layer2	layer3	layer4
$(\text{Path}_{\text{Spiral}}/\text{Path}_{\text{Straight}})$	1.29	1.39	1.50	1.62

In order to check whether the difference in path length affects the time response, the correlations between the  $z$  position and the time response was plotted as shown in Figure 5.9. The  $z$  position was obtained from the CFT tracking.

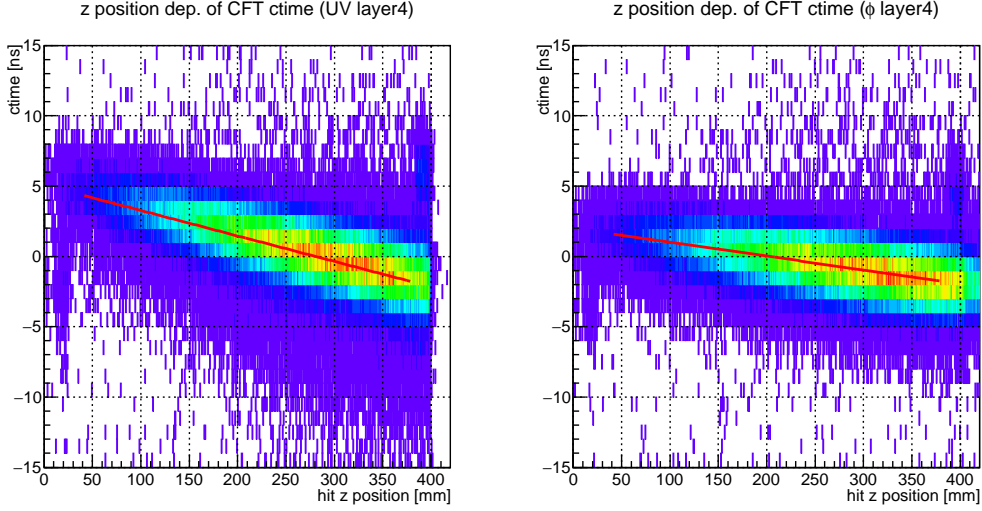


Figure 5.9: Left figure shows the hit  $z$  position dependence of CFT time distribution of a spiral layer(V4 layer) and the right figure shows the one of a straight layer( $\phi$ 4 layer).

Here, the slope obtained by straight-line fitting of Figure 5.9 corresponds to the propagation speed of light in the fiber. They were obtained to be  $1.8 \times 10^{-2}$  [ns/mm] (Spiral layer4) and  $9.8 \times 10^{-3}$  [ns/mm] (Straight layer4).

Regarding the slope corresponding to the strength of path length dependence, the ratio of the spiral layer and the straight layer is obtained to be Spiral / Straight = 1.83. This ratio roughly matches the one considering only the fiber structure calculated in Table 5.3, but it is slightly larger. Not only the path length by the structure but also the bending angle of the fiber are different between the straight and the spiral layer. In any case, since there is a clear correlation with  $z$ , it is possible to perform time correction according to this straight line. Figure 5.10 shows the ctime distribution corrected by subtracting the value of the straight line determined by Figure 5.9.

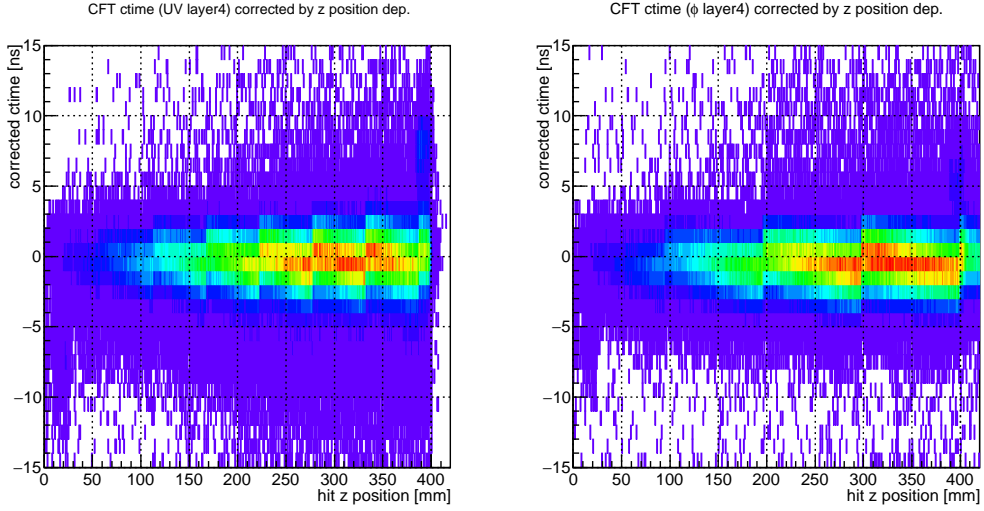


Figure 5.10: Left figure shows the hit  $z$  position dependence of CFT time distribution for a spiral layer(V4 layer) after  $z$  position correction and the right figure shows the one for a straight layer( $\phi$ 4 layer).

Figure 5.11 shows the  $ctime$  distribution after correction. It is found that the spread of the time response is reduced by the correction.

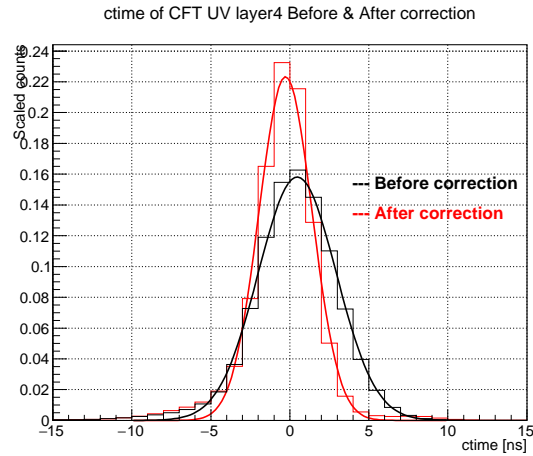


Figure 5.11: Time distribution of protons detected by CFT for a spiral layer. The red line shows the one before  $z$  position correction, and the blue line shows the one after the correction.

As a result of the above analysis, the spreads of the time response after the  $z$  position correction are summarized in the Table 5.4. Here, the error for each

$\sigma$  value was sufficiently small, less than  $3 \times 10^{-3}$  ns.

Table 5.4: Summary of CFT time resolution (rms) for each layer in the units of ns

Path length ratio	UV1	UV2	UV3	UV4	$\phi 1$	$\phi 2$	$\phi 3$	$\phi 4$
Before correction	2.02	2.24	2.39	2.47	1.98	1.98	1.86	1.83
After correction	1.57	1.68	1.63	1.68	1.76	1.72	1.54	1.56

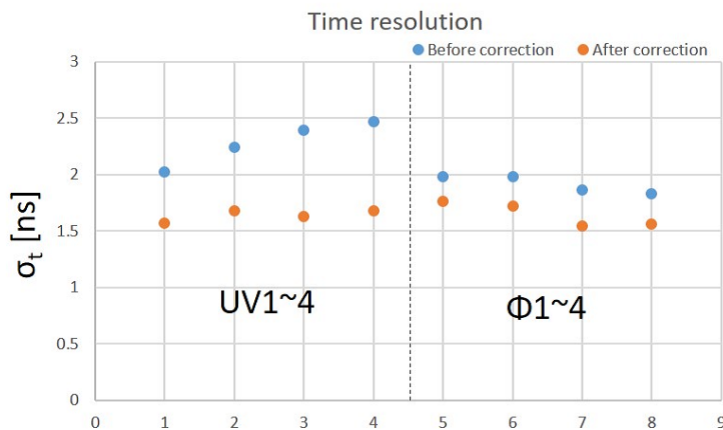


Figure 5.12: Time resolution of CFT for a spiral and straight layers. Each resolution before and after the  $z$  position correction for each layer is shown.

The radial dependence of the spiral layer resolution before correction is consistent with the relation of the path length indicated by Table 5.3.

The time resolution  $\sigma_{time}$  less than 1.8 ns has been achieved for all the layers.

Assuming that the event time separation is done in the  $\Sigma p$  scattering experiment with the probability of 99.9% from the background events of 2 MHz for the innermost layer, the time gate of CFT is required to be 12 ns, which corresponds to the time resolution of 2 ns ( $\sigma_{time}$ ), as discussed in Chapter 2. As a result, the time resolution of CFT was obtained to be  $\sigma_{time} < 1.8$  ns and it satisfies the requirement of 2 ns ( $\sigma_{time}$ ) for the  $\Sigma p$  scattering experiment.

## 5.5 Energy calibration

The energy information of the proton is obtained by measuring the energy losses in CFT and the BGO calorimeter. In this section, the energy calibration of the BGO calorimeter and CFT were performed, and then the energy resolutions are evaluated. Both detectors were calibrated using the correlation between the energy and the scattering angle of  $pp$  and  $pC$  scattering events.

## 5.6 Energy calibration of BGO calorimeter

In this test experiment, the BGO calorimeter is read by Flash ADC which is the same method with E40 experiment. The conversion from waveform to the energy deposit in BGO is performed in this section.

### Waveform analysis

The BGO signal was filtered with an integration circuit and the shaped signal was sampled with a sampling rate of 33 MHz. Figure 5.13 shows the waveform obtained when the BGO calorimeter detects a scattered proton in this experiment.

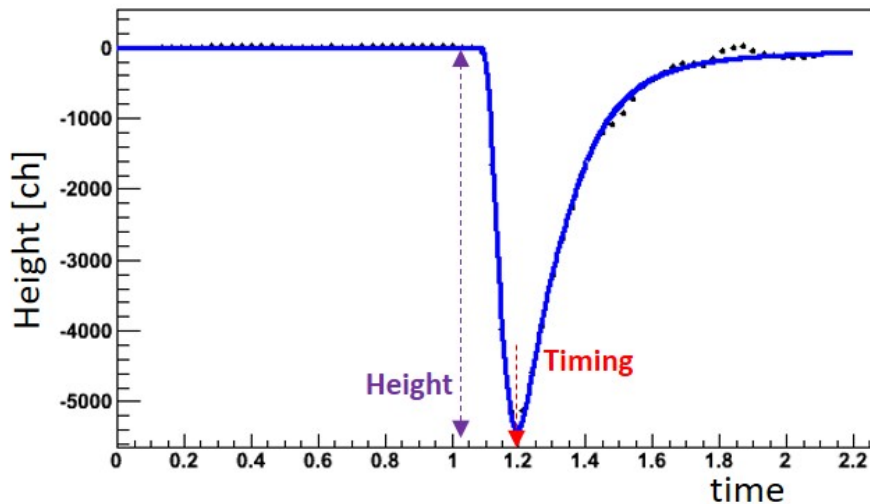


Figure 5.13: A waveform of the BGO calorimeter for the emitted proton from the target. The BGO signal was acquired with Flash ADC after being filtered with an integration circuit.

As described in Chapter 2, a template waveform was obtained by averaging the measured data, and the pulse height and the timing of each waveform were obtained by using the template Fitting method. This pulse height corresponds to the energy deposit of protons detected by the BGO calorimeter.

### Scattering angle correlation of proton energy

The energy of protons incident on the BGO calorimeter has a correlation with the scattering angle  $\theta$ . Since  $pp$  and  $pC$  scatterings are two-body reactions, there are one-to-one correlations between  $\theta$  and scattered proton's energy. However, protons pass through CFT before they are injected into BGO. It is necessary to consider the energy loss in CFT to obtain the incident energy.

Figure 5.14 shows the correlation between the scattering angle  $\theta$  and the BGO pulse height for proton detection, where  $\theta$  was obtained by CFT tracking. The loci corresponding to the  $pp$  and  $pC$  scattering are confirmed in this figure.

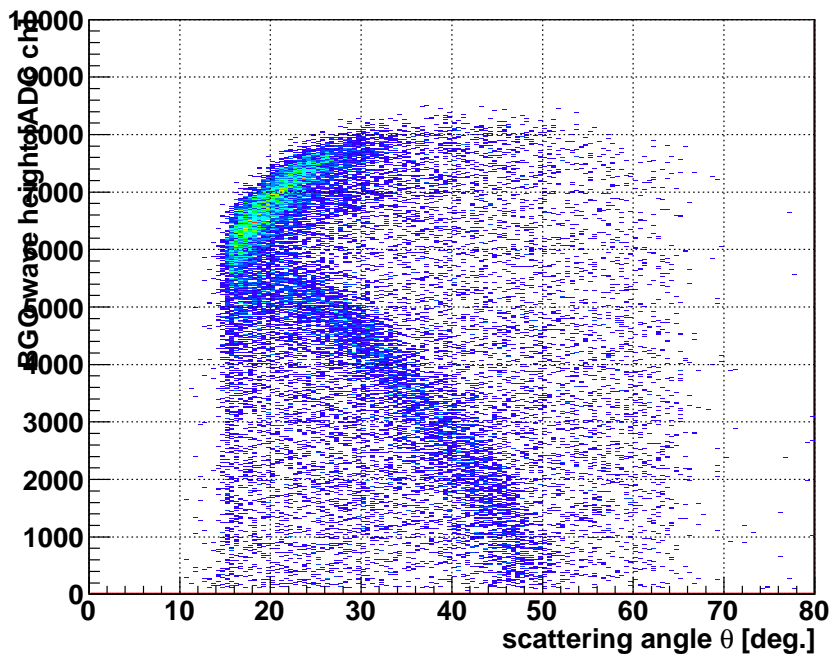


Figure 5.14: Correlation between the pulse height of BGO (segment8) and  $\theta$  for protons from  $pp$  and  $pC$  scatterings.

We have to separate  $pp$  scattering events from  $pC$  scattering events for the

energy calibration. We first find one track with hits in (all) the straight layers and the BGO calorimeter, and then request a hit in the straight layer 1 at the opposite position of the first track, as shown in Figure 5.15. Because most of the recoil carbon nuclei are stopped in the target in  $pC$  scattering events,  $pp$  scattering events are selected by requiring two particle detection in CFT.

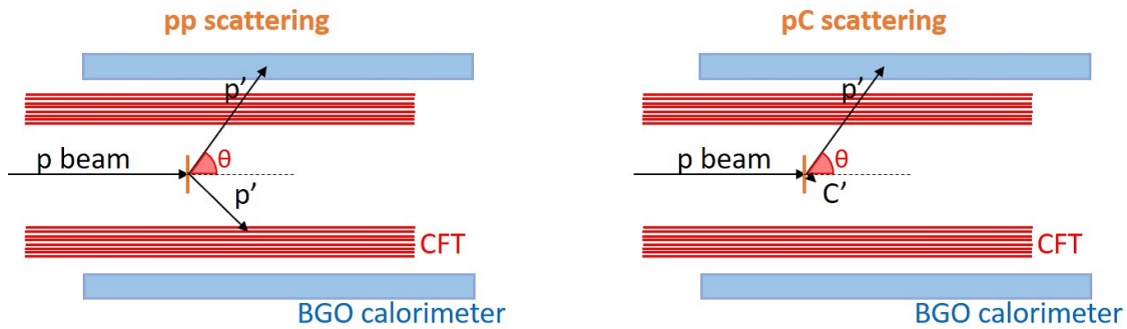


Figure 5.15: In order to select  $pp$  scattering events, we requested a hit in CFT straight layer 1 at the opposite position of the obtained track. On the other hand, a recoil carbon from  $pC$  scattering stops before reaching to CFT.

The selection of  $pC$  scattering events is performed by selecting a large pulse height region in the BGO calorimeter. This event selection is shown in Figure 5.17.

In the simulation the experimental setup was reproduced, in which the energy deposit in the CFT was also taken into account. Figure 5.17 shows the response of the BGO calorimeter for the scattered proton from  $pp$  scattering obtained from the measurement and the simulation. In the same way, Figure 5.16 shows those for the  $pC$  scattering.

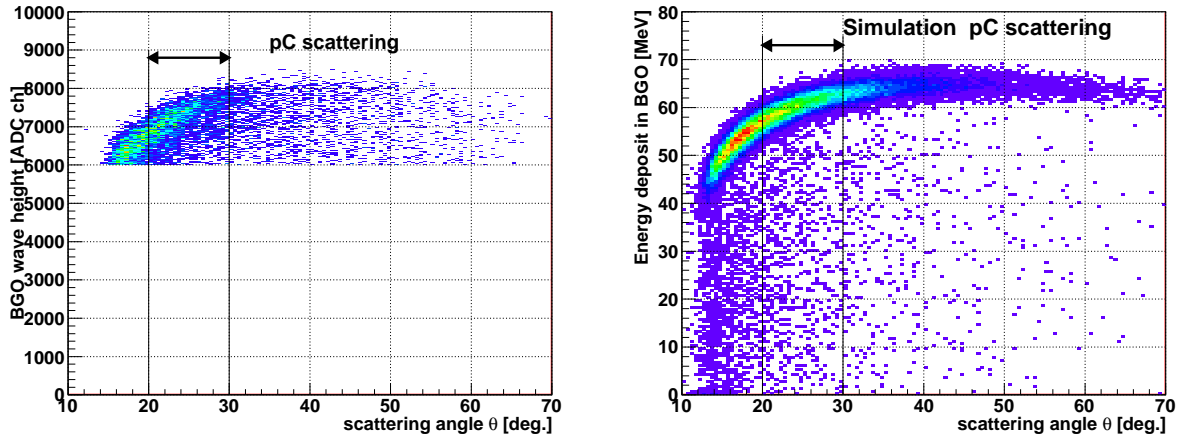


Figure 5.16: Left figure shows the correlation between the pulse height of BGO (segment8) and  $\theta$  for protons from  $pC$  scatterings. By selecting a large pulse height region of the BGO calorimeter,  $pC$  scattering events were selected. The right figure shows the simulated energy deposit of the scattered proton from  $pC$  scattering.

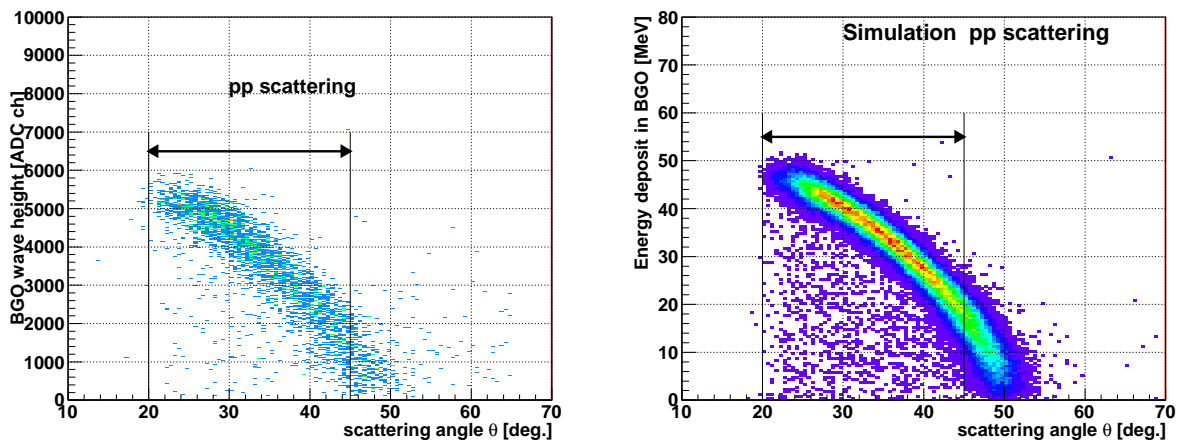


Figure 5.17: Left figure shows the correlation between the pulse height of BGO (segment8) and  $\theta$  for protons from  $pp$  scatterings. In the left figure, the opposite side hit of CFT is required in order to select only  $pp$  scattering event. The right figure shows the simulated energy deposit in the BGO calorimeter.

By comparing the measured pulse height of BGO and the simulated energy in the same scattering angle  $\theta$ , a function for energy calibration was obtained. In

order to avoid ambiguity due to a large fluctuation depending on low statistics, the angular regions were selected to be 20-45 degrees and 20-30 degrees for  $pp$  and  $pC$  scattering, respectively. This comparison between the BGO pulse height and the simulated energy is shown in Figure 5.18.

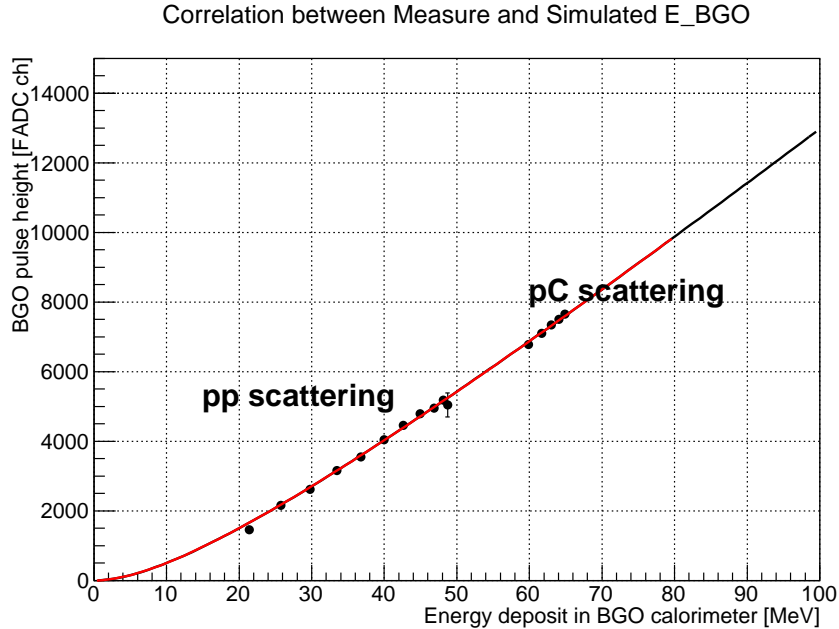


Figure 5.18: Correlation between the measured BGO (segment8) wave height and the simulated energy for  $pp$  and  $pC$  scattering.

This calibration function is expressed by the following equation phenomenologically [19].

$$\text{BGO pulse height[ch]} = a \times \text{Energy[MeV]} - b \times \ln \left( \frac{\text{Energy[MeV]} + b}{b} \right) \quad (5.1)$$

The parameters  $a$  and  $b$  were obtained by fitting the data points in Figure 5.18 with this equation.

The correlation between the BGO energy and scattering angle  $\theta$  after the above energy calibration is shown in Figure 5.19.

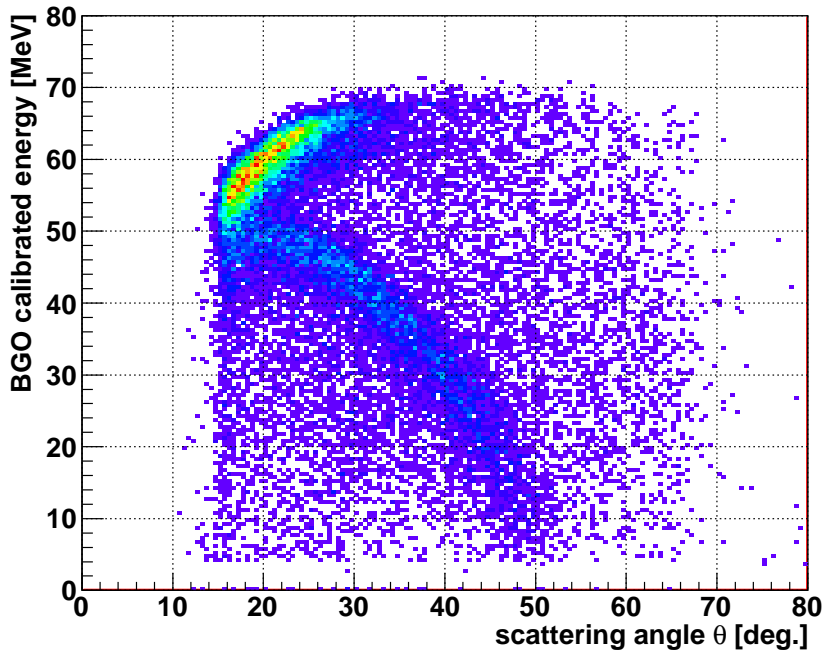


Figure 5.19: Correlation between BGO energy and scattering angle  $\theta$  after BGO energy calibration. The data for segment 8 is shown in this figure as an example.

The BGO energy calibration was performed for all the 24 BGO segments with the above method.

### BGO Energy resolution

In this section, the energy resolution of the BGO calorimeter after the energy calibration of the BGO is evaluated. However, it is difficult to evaluate the intrinsic energy resolution of the BGO calorimeter itself from this experiment, because the energy deposit of proton in CFT is not constant. In this section, we checked whether the BGO calorimeter was operated with sufficient performances by evaluating the spread of proton energy measured by the BGO calorimeter.

Figure 5.20 shows the spread of the energy distribution measured by the BGO calorimeter for each  $\theta$ , and Figure 5.21 shows the BGO energy distribution for the  $\theta$  region of 25 to 30 degree.

In order to select  $pp$  and  $pC$  scattering events, the same conditions as for the energy calibration described above were required.

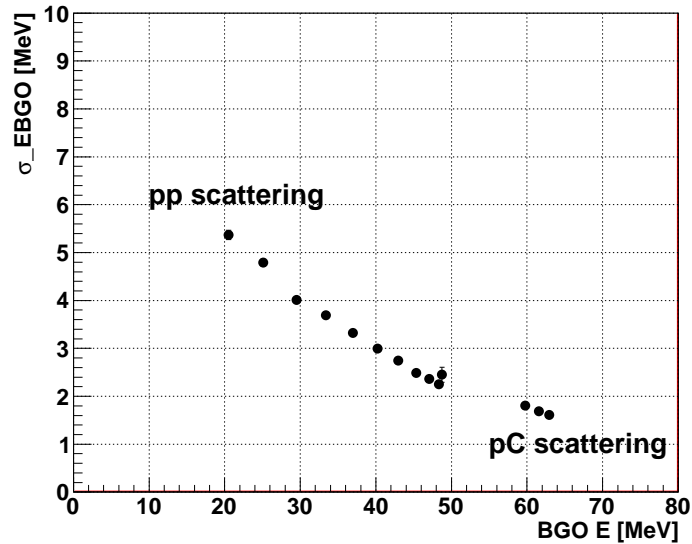


Figure 5.20: Spread of the energy distribution measured by the BGO calorimeter for each  $\theta$ .

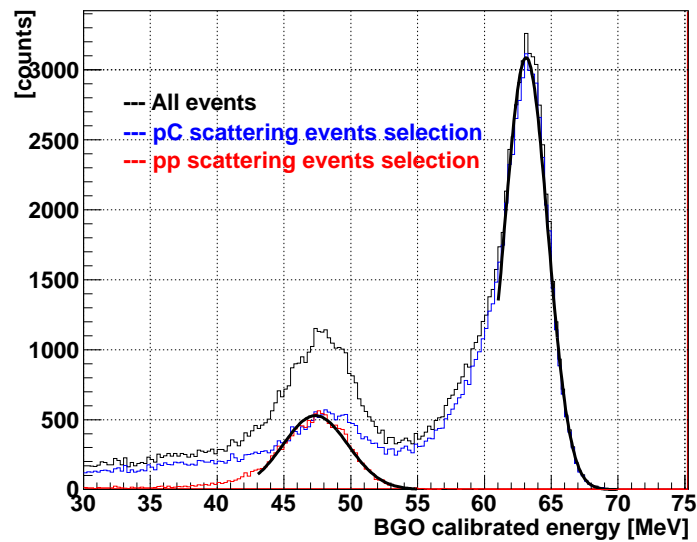


Figure 5.21: Energy distribution measured by BGO calorimeter, where the scattering angle  $\theta$  was selected from 25 to 30 degrees.

In this setup, since the scattered protons enter the BGO after passing through the CFT, the measured energy by the BGO calorimeter should be spread. Therefore, the obtained spread was different from the intrinsic energy resolution of the BGO calorimeter. In order to estimate the intrinsic energy resolution of the BGO calorimeter, the measured result was compared with the simulation which consider the effect of materials in CFT. The  $pC$  scattering event was used for this evaluation in order to avoid large ambiguity due to the small energy of protons. The simulated energy spreads and the assumed intrinsic energy resolutions of the BGO calorimeter are summarized in Table 5.5.

Table 5.5: Simulated energy spread of the BGO calorimeter

Assumed intrinsic resolution $\sigma_{EBGO}$ at 80 MeV proton	1%	1.2%	1.5%	2%
Spread after passing through CFT ( $\theta = 25 \sim 30$ degree)	2.29%	2.29%	2.54%	2.93%

The spread of the energy measured by the BGO calorimeter was obtained to be  $\sigma = 1.6$  MeV for 63.4 MeV proton, which corresponds to 2.47% ( $\sigma$ ). By comparing the measured result with the simulated results, the intrinsic BGO energy resolution was estimated to be 1.2% and 1.5% in ( $\frac{\sigma}{Mean}$ ) for 80 MeV proton.

For the  $\Sigma p$  scattering experiment, the required performance of the BGO calorimeter is 80 MeV and  $\frac{\sigma}{Mean} = 3\%$ . Therefore, we confirmed that the required performance was sufficiently satisfied.

## 5.7 Energy calibration of CFT

The energy calibration of CFT was performed by comparing a measured ADC value with a simulated energy deposit for each scattering angle  $\theta$  as mentioned in the calibration of the BGO calorimeter. The response of energy deposit  $dE$  for scattering angle  $\theta$  is different between the straight layer and the spiral layer due to their layer structures. They are explained separately in the following sections.

### 5.7.1 MPPC output normalization

In order to make the operating points of all the MPPCs uniform, the amplification factor of each MPPC was set to be as uniform as possible by adjusting the operation voltage. However, as shown in Figure 5.22, there still existed difference in the operation point.

In the ideal case, the ADC gain of each fiber should be calibrated individually. However, the statistics of the calibration data for one fiber was not enough. Therefore, we combined the ADC values in each layer and the calibration was performed for each layer. For this purpose, the ADC value of each MPPC should be normalized.

Figure 5.22 shows a scatter plot between the fiber segment number and the ADC distributions in a certain CFT layer in the  $pp$  and  $pC$  scattering experiment. The range of  $\theta$  was selected from 20 to 30 degrees. In this figure, the ADC value of 0 on the vertical axis corresponds to the pedestal, which was obtained by clock trigger data during beam irradiation.

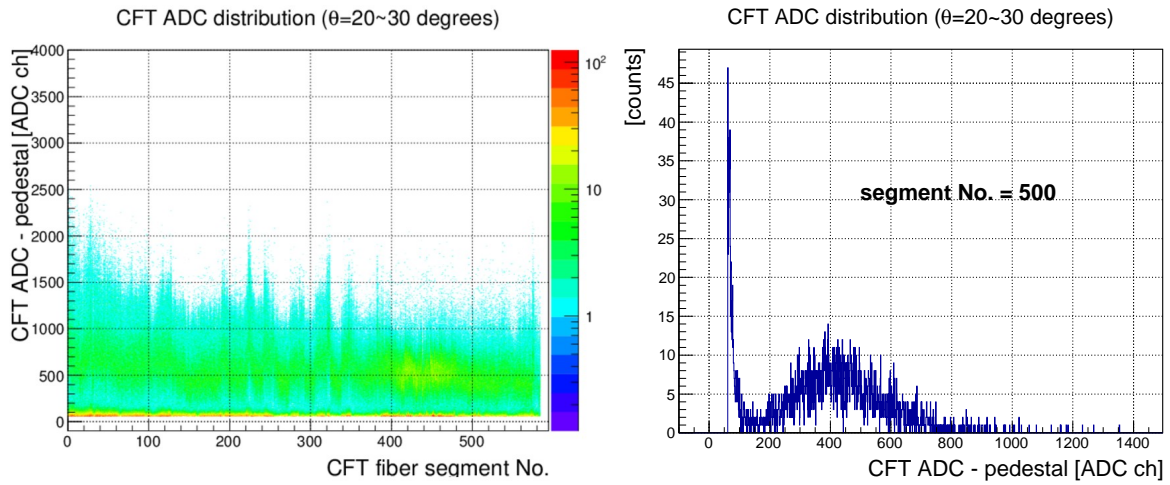


Figure 5.22: Left figure shows CFT ADC for each segment of a certain layer with scattering angle  $\theta = 20\text{-}30$  degrees in the  $pp$  and  $pC$  scattering experiment. The ADC value of 0 on the vertical axis corresponds to the pedestal. Right figure shows the ADC distribution for a certain segment. Each peak position was obtained for each segment.

As can be seen from this figure, the output ADC is not uniform for the same energy deposit. The peak position of each MPPC's ADC was normalized to be 5.

Figure 5.23 show the result of CFT's ADC normalization.

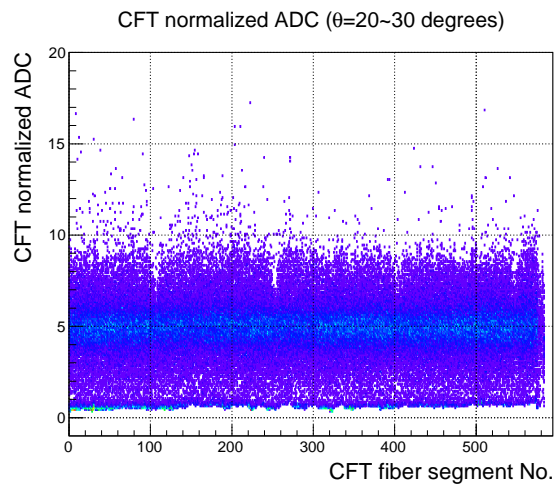


Figure 5.23: ADC values of the CFT's MPPCs normalized by using scattered protons from  $\text{CH}_2$  target and proton beam.

### 5.7.2 CFT straight layer

Since the straight layer's fiber was placed parallel to the beam direction, the "pathlength" inside the fiber of emitted proton depends on the scattering angle  $\theta$  as shown in Figure 5.24. Corresponding to the path length, the energy deposit in the fiber should also change.

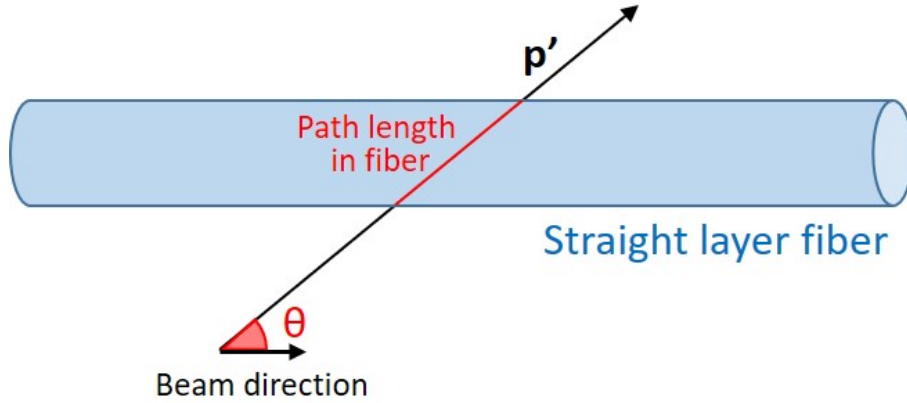


Figure 5.24: Schematic illustration of the relation between a path length in fiber and  $\theta$ .

The energy deposit in the fiber also depends on the energy of proton.

Therefore, we have to consider these two components to understand the  $\theta$  dependence of the energy deposit.

Figure 5.25 (a) shows  $\theta$  dependence of the normalized ADC where  $pp$  and  $pC$  scattering events were mixed. As we mentioned, the normalized ADCs of all the segments in one layer are combined. In this figure, data of the straight layer 3 is shown. To calibrate the energy, the  $pp$  and  $pC$  scattering events should be separated. The separation method is the same as mentioned in the BGO calibration.

Figure 5.25 (b) and (c) show the scatter plots between  $\theta$  and the normalized ADC for  $pp$  and  $pC$  scattering events, respectively.

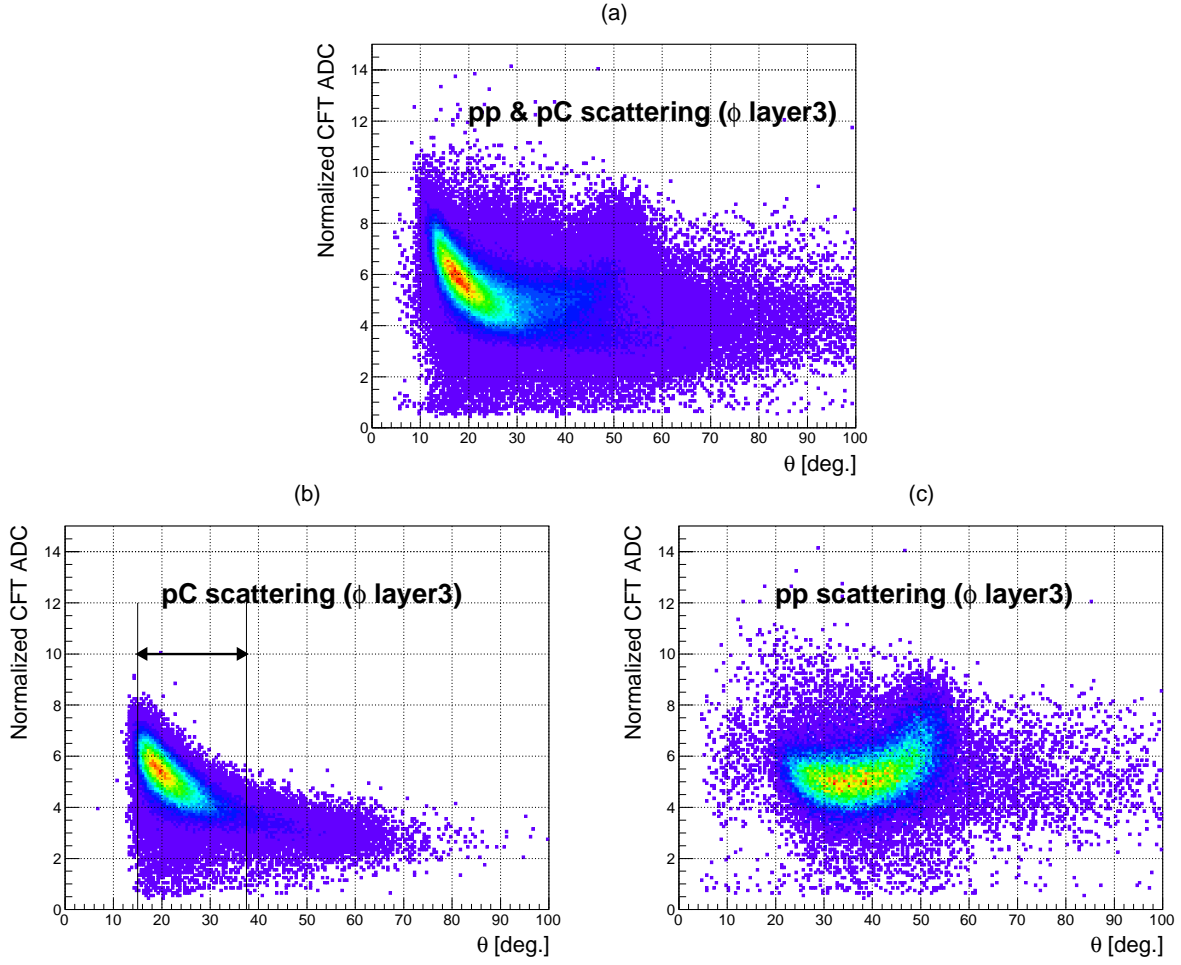


Figure 5.25: Scatter plots between  $\theta$  and the normalized ADC value. Up figure shows both of  $pp$  and  $pC$  scattering events. Left figure shows  $pC$  scattering events by selecting the proton's kinetic energy measured by the BGO calorimeter. Right figure shows  $pp$  scattering events selected by requiring two particle detection in CFT.

There is a larger correlation between  $\theta$  and the normalized ADC in  $pC$  scattering. This is suitable for the energy calibration. Therefore, the  $pC$  scattering data were used for energy calibration of CFT.

Similar to the energy calibration of the BGO calorimeter, the normalized ADCs of CFT were compared with the simulated energy deposit as a function of the scattering angle  $\theta$ . Figure 5.26 (b) and (b') show the comparison between the data and the simulation, respectively. The relation between the data and the simulation with the same scattering angle  $\theta$  for every 2.5 degrees are shown

in Figure 5.26 (c).

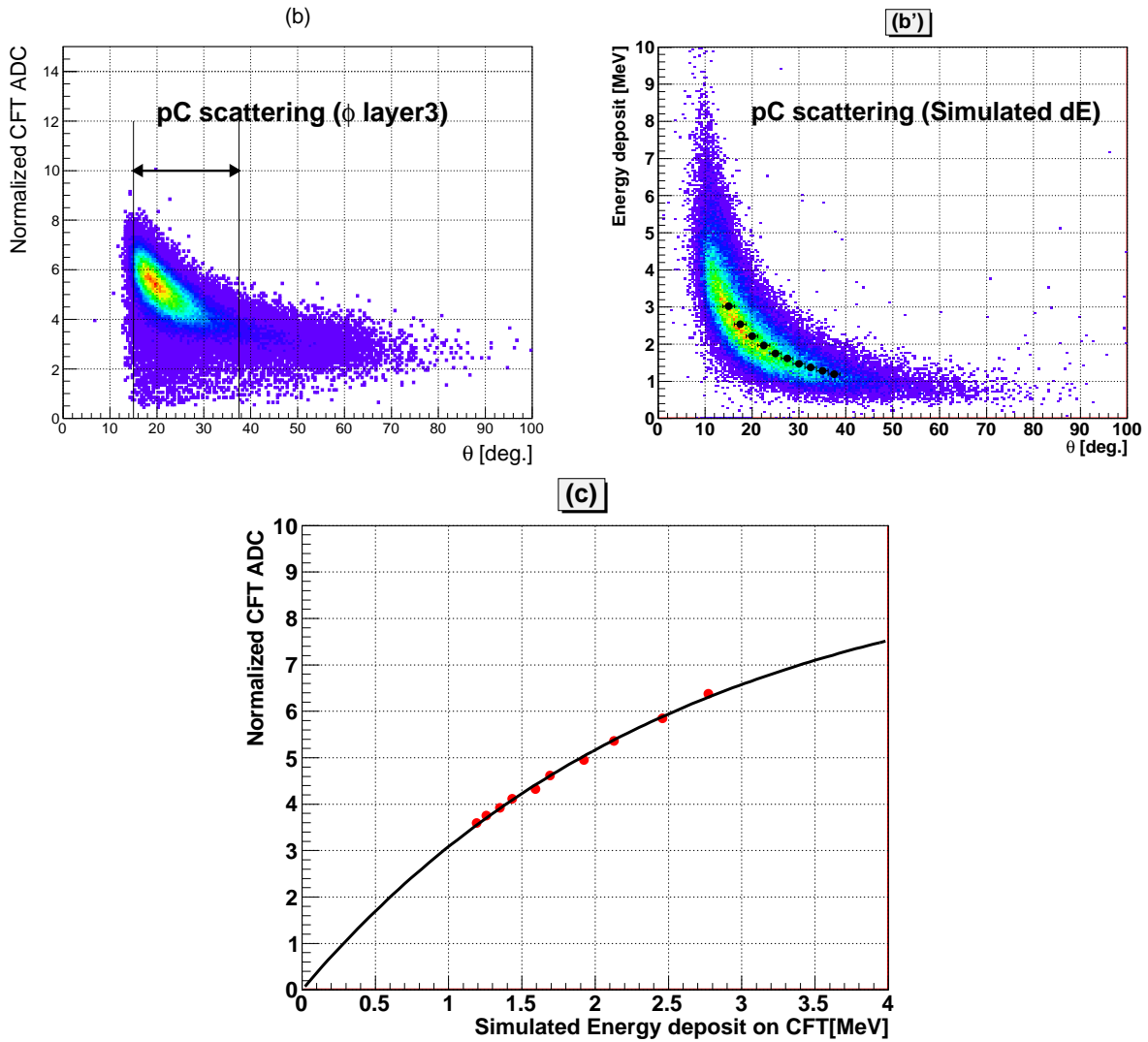


Figure 5.26: Left figure (b) is the same with Figure 5.25 (b). Right figure (b') shows the simulated angular dependence of the energy deposit in CFT straight layer for  $pC$  scattering. Bottom figure (c) shows the correlation between the normalized CFT ADC actually measured and the simulated energy deposit in CFT.

In Figure 5.26, the normalized ADC becomes saturated for the large energy deposit due to the saturation effect of MPPC. Here, the relation between the number of photons incident on one MPPC and its output (detected number of photons) should be considered. The output of MPPC is proportional to the

number of APDs (Avalanche Photodiodes, constituting MPPC) that detected photons. The number of effective APD pixels ( $N_{eff}$ ) in the MPPC covering the fiber end face is the maximum number of detectable photons. As the number of incident photons increases, multiple photons are incident on the same APD pixel, and the number of detected photons will be counted down. This relationship is expressed by the following equation[23],

$$N_{detected} = N_{eff} \times \left\{ 1 - \exp\left(\frac{-B \times dE}{N_{eff}}\right) \right\}$$

where,  $N_{detected}$  is the number of photons detected by MPPC, and  $N_{eff}$  is the number of effective pixels covering the fiber edge. B corresponds to the generated photon number for a unit energy.

By fitting the correlation in Figure 5.26 with this equation, the energy calibration function was obtained.

$N_{eff}$  was obtained to be about 200 pixels as a result of this fitting. By considering the size of the CFT fiber of  $0.75 \text{ mm}\phi$  and the MPPC size of  $1 \times 1 \text{ mm}^2$ ,  $N_{eff}$  should be about 180 pixels. By considering that there is a gap of about 1 mm between the fiber end face and the MPPC, the obtained result could be explained.

Then we confirmed that this relation does not depend on the layers very much if the MPPC operation points are almost the same. We overwrite these relations of all the straight layers in Figure 5.27, where the calibration function is adjusted at the point of the energy deposit of 3 MeV in the left figure. The saturation shape of each layer was found to be consistent with each other. This correlation is used for the calibration of the spiral layers, because the clear relation in the spiral layers can not be seen due to the layer structure.

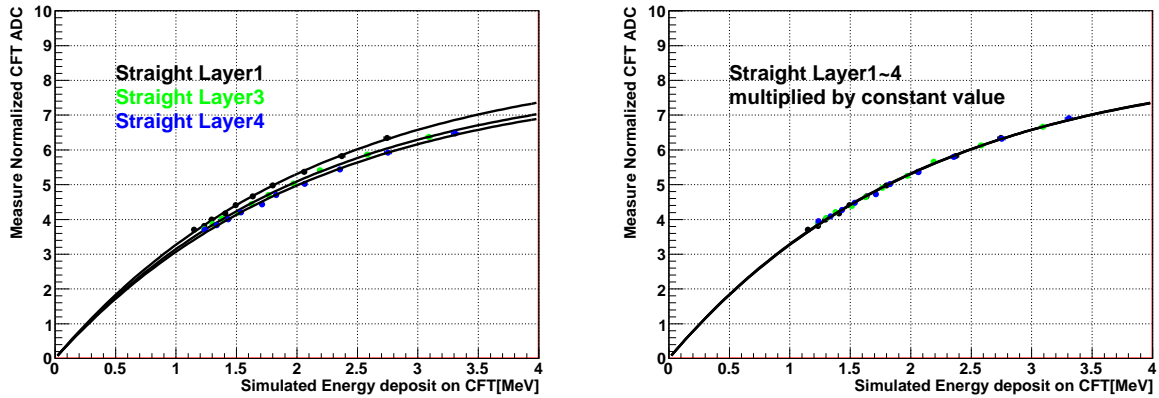


Figure 5.27: The shape of calibration curve obtained from CFT straight layers. Since the normalization standard of CFT ADC for each layer is different, the vertical axis is adjusted by multiplying the constant value at the point of the energy deposit of 3 MeV. Left and right figures show the correlation curves before and after multiplying the constant value. The saturation shape of each layer was consistent with each other.

### 5.7.3 CFT spiral layer

The energy calibration of the spiral layers of CFT will be explained in this section. Like the CFT straight layers, the correlations between the normalized ADC, which is proportional to the detected photon number, and the scattering angle  $\theta$  for  $pp$  and  $pC$  scattering events are shown in Figure 5.28.

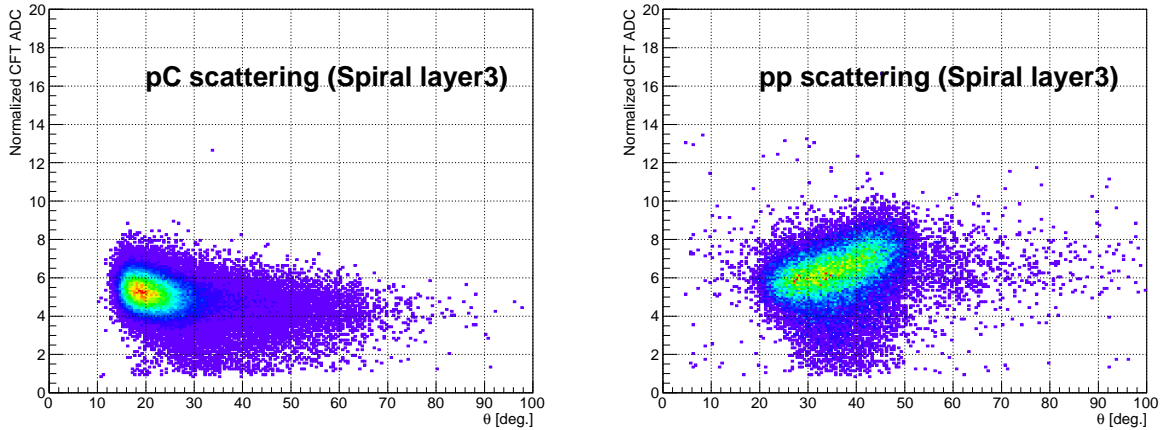


Figure 5.28: The scatter plot between the normalized ADC of CFT spiral layer(Layer3) and the scattering  $\theta$ . Left figure shows the correlation after selecting  $pC$  scattering, and right figure shows one after selecting  $pp$  scattering.

From the fiber arrangement of the spiral layer, the fiber cross section is elliptical, which is different from the straight layer. This caused a smaller path length variation against the change of  $\theta$  as shown in Figure 5.29. Therefore, the energy loss does not depend on  $\theta$  very much.

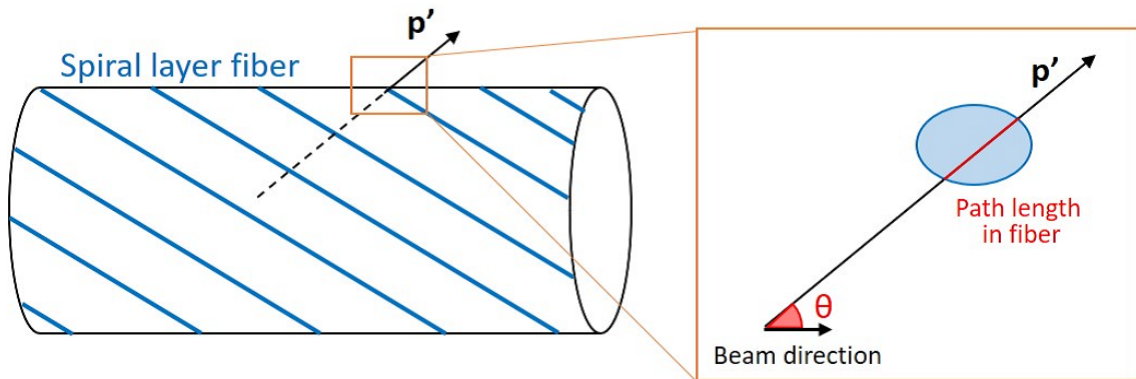


Figure 5.29: Cross sectional shape of the CFT spiral fiber section on the plane of the scattered proton.

On the other hand, changes in energy loss according to the proton energy was found in  $pp$  scattering in the right figure of Figure 5.28. However, in the spiral layer, there is ambiguity of the energy deposit in CFT due to the path length in fibers. Due to the fiber arrangement structure, the path length

change locally from 0 to the sum of the radius of some fibers. Therefore, it is difficult to reproduce the effect of such conditions of structures and materials in the simulation. For the above reasons, it is difficult to obtain the energy calibration function from actually measured light yield for the CFT spiral layer from this data. Therefore we decided to use another method.

The energy calibration curve was already obtained from the straight layers. Therefore, we keep this shape of calibration curve and multiply it by a constant coefficient to determine the calibration curve for the spiral layers.

Optimum coefficients were obtained by least squares method for the correlation between the detected photon number and the energy expected by simulation as shown in Figure 5.30. For the reference point in the energy calibration, the angular region of  $\theta = 25 \pm 1.25$  degrees was used. The ambiguity of the energy deposit in one fiber depends on the energy of incident proton strongly, the forward scattering angle, which corresponds to the larger energy of the scattered proton, was used.

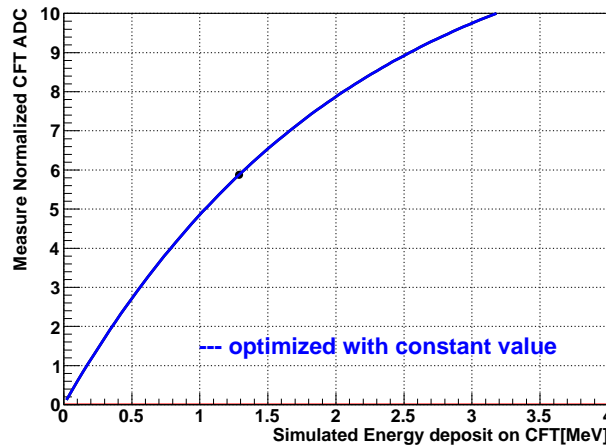


Figure 5.30: Energy calibration curve for the CFT spiral layer. Blue line shows the result obtained from the shape of straight layer calibration curve.

The blue line in Figure 5.30 shows the result obtained from the shape of straight layer calibration curve.

In this way, the energy calibration of CFT was performed on the straight layers and the spiral layers.

## Energy resolution

Since there are variations in the proton's energy deposit in CFT due to the difference of path length in the fiber, the measured energy spread is larger than the intrinsic CFT energy resolution. The evaluation is performed by selecting protons from  $pp$  scattering and  $pC$  scattering in the same way as in the previous section, and the result is shown in Figure 5.31.

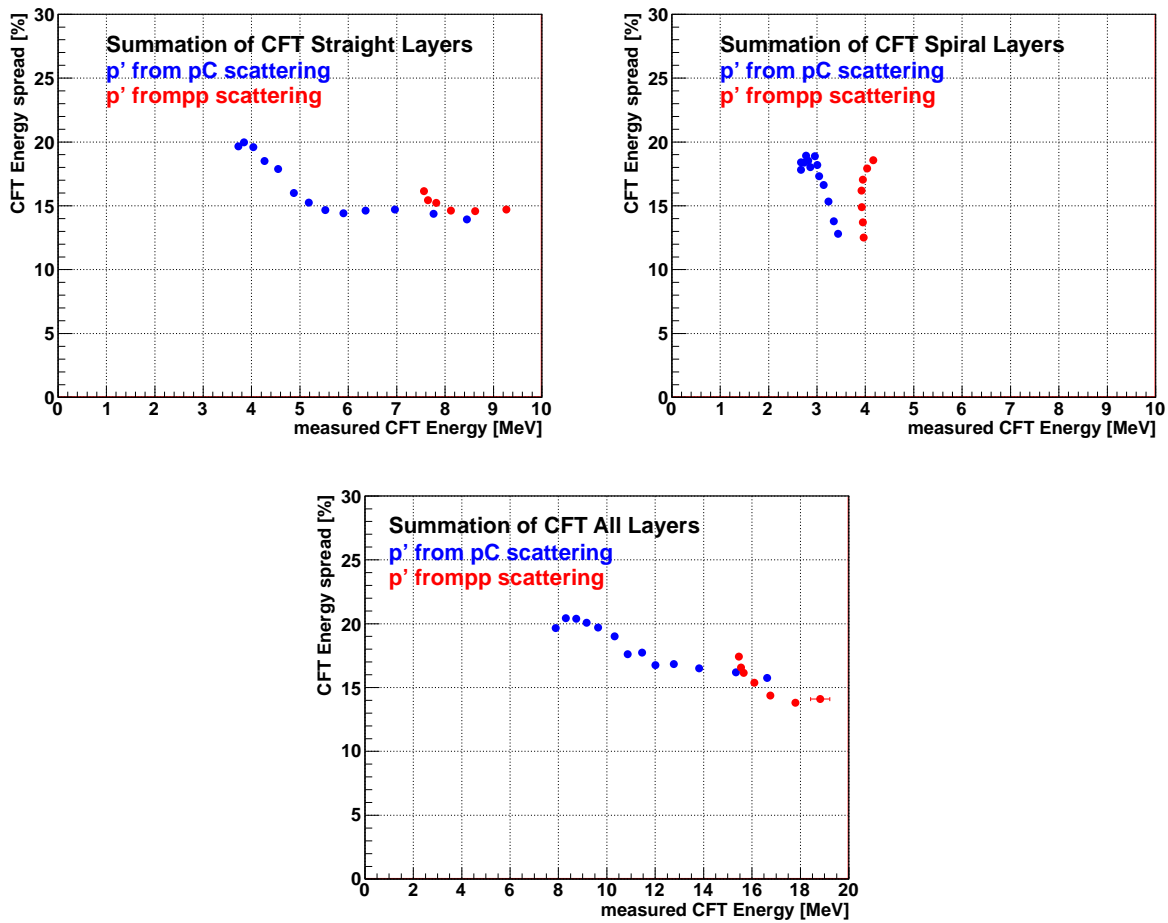


Figure 5.31: The spreads of the energy deposit in the CFT straight layer and spiral layer are shown in left figure and right figure, respectively. Bottom figure shows that of the total energy measured by all the CFT layers.

The dependence of the measured energy and the spread is different between the straight layer and the spiral layer, which is considered to be derived from the structure each layer. As can be seen from Figure 5.31, the measured energy

in the spiral layer is only several percent of the total proton's energy. Therefore, its influence is considered to be limited.

Overall, there was a tendency that the resolution improves in the large energy deposit region in CFT, but the tendency does not obey  $\frac{1}{\sqrt{E}}$  relation. If the energy calibration functions are individually obtained for segment by segment, the energy resolution is considered to be further improved.

Although future improvement can be expected, the CFT energy resolution has been achieved to be smaller than 20% at 10 MeV energy deposit in CFT.

In order to check whether the energy resolution of CFT satisfies the requirement for the  $\Sigma p$  scattering experiment, the performance for particle identification between proton and pion is evaluated in chapter 6.

## 5.8 $\Delta E$ distribution

Since the energy calibrations of the CFT and BGO calorimeters were performed, the kinetic energy of the proton can be reconstructed by adding the energy deposits of the CFT and BGO. Figure 5.32 shows the scatter plot between  $\theta$  measured by CFT tracking and the total proton energy measured by CFT and the BGO calorimeter for the CH<sub>2</sub> target data. The loci corresponding to  $pp$  and  $pC$  scattering are identified.

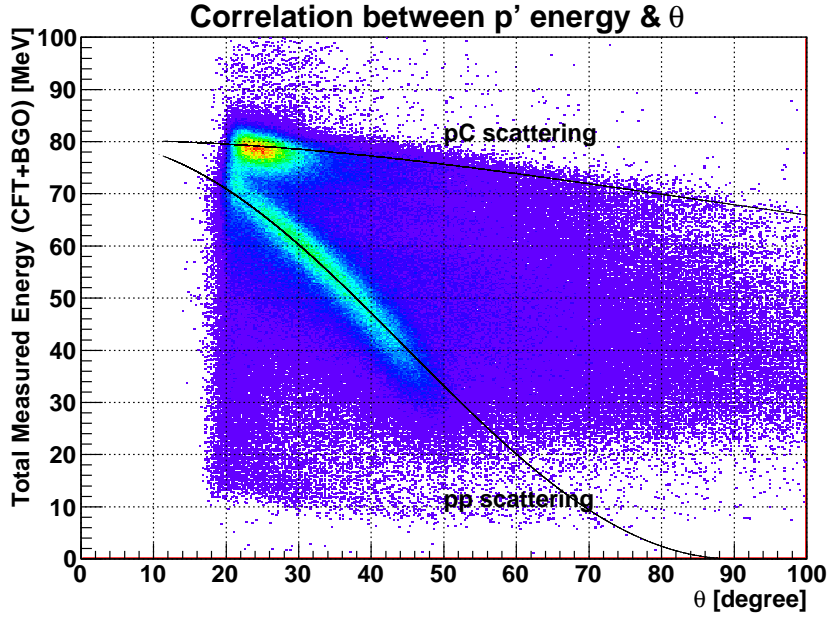


Figure 5.32: Scatter plot between scattering angle  $\theta$  and scattered proton energy measured by CATCH when the  $\text{CH}_2$  target is irradiated with a proton beam. The solid lines show the kinematically expected relations for  $pp$  and  $pC$  scatterings.

The kinematical lines for  $pp$  and  $pC$  scatterings are also overwritten in Figure 5.32. These lines are consistent with the measured correlation for each reaction of  $pp$  and  $pC$  scattering.

The difference between this calculated value and the measured value is defined as  $\Delta E$  as shown in following equation,

$$\Delta E = Ep'_{measure} - Ep'_{calculate}, \quad (5.2)$$

where  $Ep'_{measure}$  and  $Ep'_{calculate}$  represent the energy of proton measured by CATCH and the energy calculated kinematically from  $\theta$  and the beam energy, respectively.

Figure 5.33 shows scatter plots between  $\Delta E$  and  $\theta$  for  $pp$  and  $pC$  scatterings. In this figure, the  $pp$  and  $pC$  scattering events are selected with the same method as the previous section.

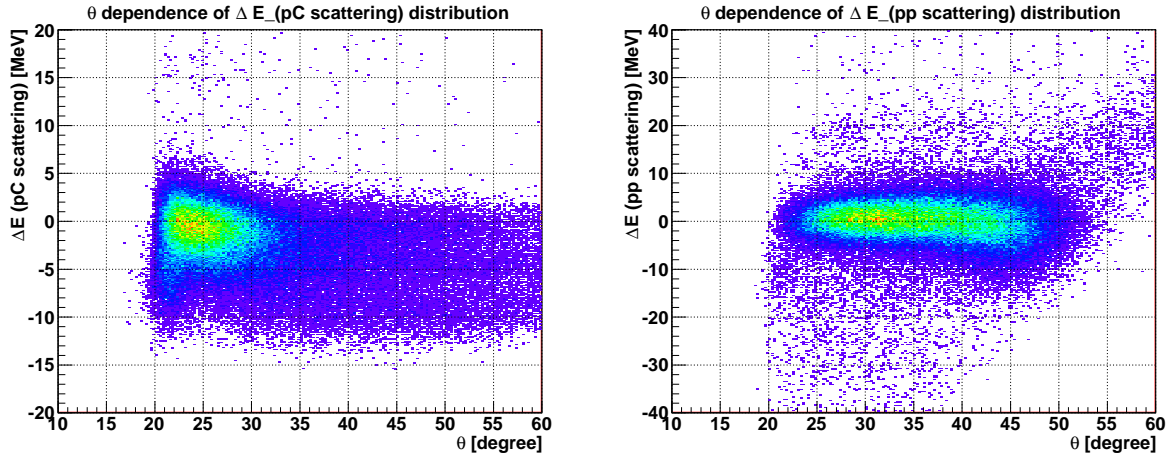


Figure 5.33: Left and right figures show the correlations between  $\Delta E (= E_{p'_{measure}} - E_{p'_{calculate}})$  and scattering angle  $\theta$  for  $pp$  and  $pC$  scattering, respectively.

We found that  $\Delta E$  actually distribute around zero, when the corresponding reaction events were selected. Sufficient energy resolution and angular resolution were required to discriminate the reactions.

The  $\Delta E$  distribution is obtained for each scattering angle  $\theta$  and the number of reaction events is counted. As an example, the  $\Delta E$  distribution at  $\theta = 25$  degrees is shown in Figure 5.34. Because it is difficult to estimate the energy deposit in the CFT frames, the events which were estimated to pass through the CFT frames were excluded from the evaluation.

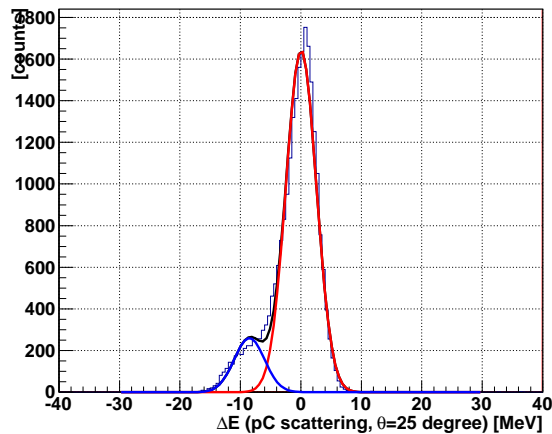


Figure 5.34: The  $\Delta E$  distribution for  $pC$  scattering within  $\theta$  of  $25 \pm 2.5$  degree.

The spread of the  $\Delta E$  distribution in Figure 5.34 was obtained to be 2.2 MeV( $\sigma_{\Delta E}$ ). This performance satisfies the requirement which is required for the typical condition of the  $\Sigma p$  scattering experiment. However, since this requirement depends on the background reactions. Therefore, it is necessary to check again for the  $\Sigma p$  scattering experiment whether this performances satisfy the requirements as discussed later.

When estimating the spread of  $\Delta E$  by a simulation considering the energy resolution of BGO ( $\sigma_{BGO\text{Energy}} = 1.2\%$  at 80 MeV) obtained in the past test experiment and the energy resolution ( $\sigma_{dECFT} = 20\%$  at 1 MeV energy deposit) of ideal CFT performances,  $\sigma_{\Delta E} = 1.87$  MeV was obtained.

In this evaluation, the measured result was worse than the estimated value because the CFT energy resolution and the angular resolution were worse than estimation. However, the influence of these difference is limited and it is enough to perform discrimination of  $pp$  and  $pC$  scattering events as discussed later. If reactions giving a large energy deposit in CFT occur, the influence will be expected to increase, so such cases have to be treated carefully.

The spread of the  $\Delta E$  distribution obtained by dividing into each scattering angle  $\theta$  is shown in Figure 5.35.

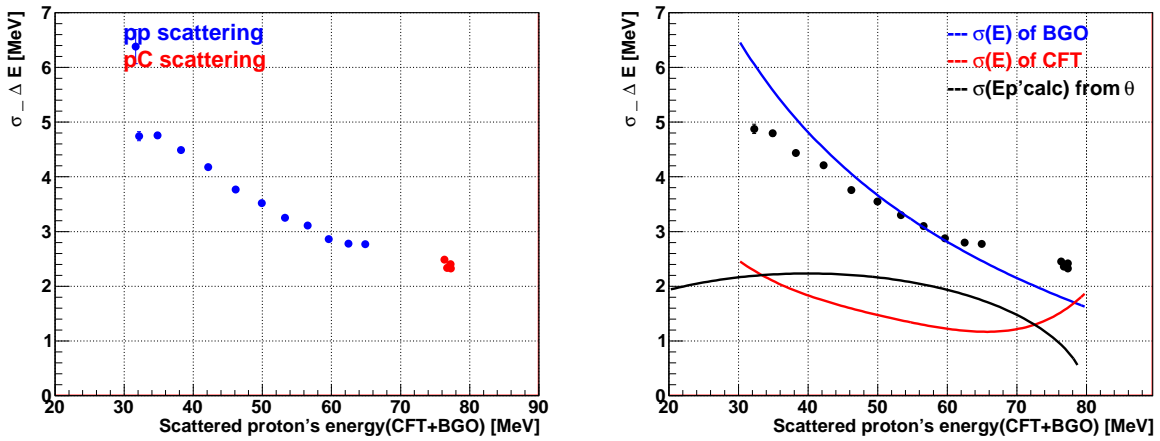


Figure 5.35: Left figure shows a scatter plot between  $\sigma_{\Delta E}$  and the energy of the scattered proton for  $pp$  and  $pC$  scatterings. Right figure shows contributions from the energy resolution of BGO calorimeter and CFT, and the angular resolution  $\sigma_{\theta}$  of CFT.

We confirmed that CATCH has sufficient performance to discriminate be-

tween  $pp$  and  $pC$  scattering events.

## 5.9 Cross section of $pp$ and $pC$ scattering

As a comprehensive performance evaluation of the CATCH system, we derived the  $pp$  and  $pC$  scattering cross sections to examine the accuracy in the cross section measurement. This examination is very important for our main purpose of measuring the differential cross sections of the  $\Sigma p$  scattering

After determining the number of detected events for each reaction of  $pp$  and  $pC$  scattering, the original number of the reaction events is obtained by dividing it by the detection efficiency of the CATCH system ( $eff_{CATCH}$ ).  $eff_{CATCH}$  means the detection probability of protons by the CATCH system, and it is expected to vary according to the incident angle  $\theta$  to the CATCH system and the energy of protons. Therefore, it is necessary to evaluate  $eff_{CATCH}$  for each conditions.

### 5.9.1 Event identification from $\Delta E$ distribution

As shown in Figure 5.34 in the previous section, the number of detected scattering events is counted from the  $\Delta E$  distribution. The results of obtaining the number of reactions identified by CATCH for each scattering angle  $\theta$  are shown in the Figure 5.36.

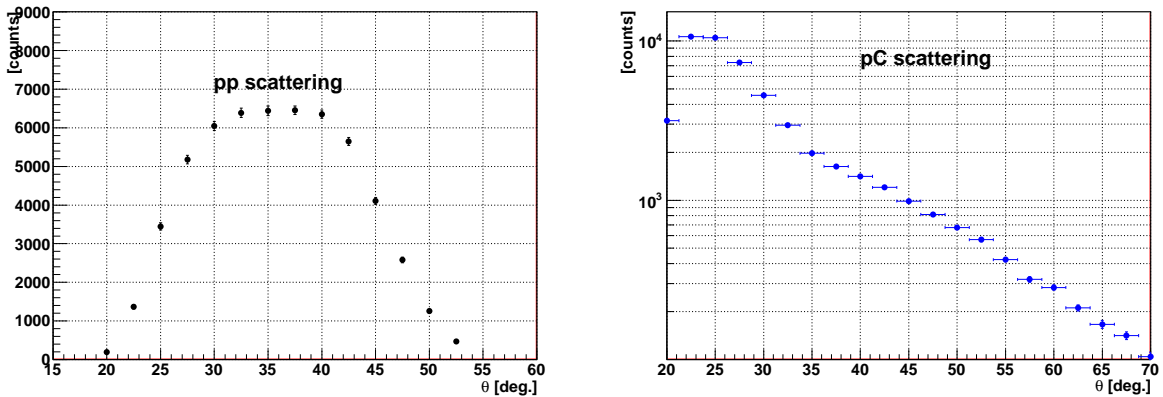


Figure 5.36: The number of detected scattering events is counted from the  $\Delta E$  distribution. Left and right figure show the obtained the number of reactions identified by CATCH for  $pp$  and  $pC$  scatterings, respectively.

In order to evaluate the measurement of the cross section, the result of this work is compared with the results of the  $pp$  and  $pC$  elastic scattering cross sections obtained in past experiments. Here, in the  $pC$  scattering, we have to consider the contamination of the  $pC$  inelastic scattering events. After deriving the scattering cross section from the number of identified events and the detection efficiency of CATCH system, the discussion of the  $pC$  inelastic scattering is carried out to determine the angular range to be compared (Section 5.8.6).

From the next section, the detection efficiency of CATCH is evaluated.

### 5.9.2 Proton detection efficiency of CATCH system

The scattered protons emitted from the target are considered to follow the process shown below until they are identified by  $\Delta E$  analysis.

1. scattering event occurs
2. scattered proton ( $p'$ ) penetrates CFT or stop in CFT
3. CFT reconstructs  $p'$  track or no track
4.  $p'$  reaches or does not reach to the BGO calorimeter
5. The BGO calorimeter measure the energy correctly or not correctly due to neutron emission

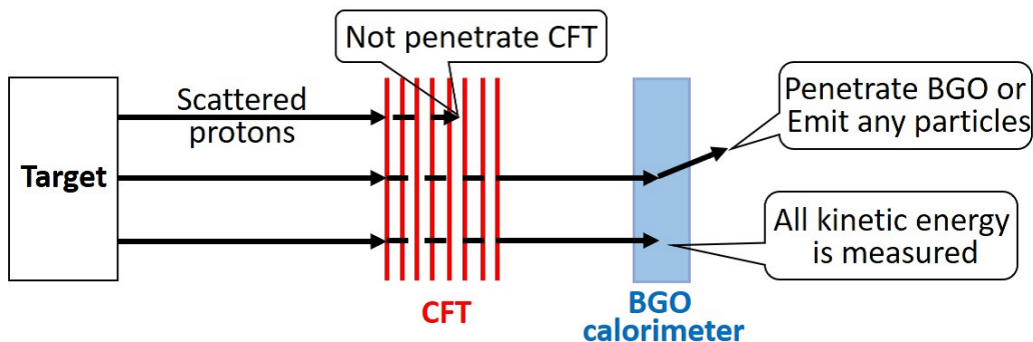


Figure 5.37: The process from scattering protons released from the target until measured by CATCH. In CFT part, they may stopped in CFT or go out of the CATCH detectors before penetrating CFT. In BGO part, the BGO calorimeter has a limited efficiency to detect the proton and measure its energy correctly.

Based on the above detection process, efficiency of CATCH ( $\epsilon_{CATCH}$ ) can be decomposed into each component as the following equation.

$$\begin{aligned} N_{Detection} &= N_{Reaction} \times \epsilon_{CATCH} \\ &= N_{Reaction} \times (\epsilon_{CFTthrough} \times \epsilon_{CFTtracking} \times \epsilon_{BGO}) \end{aligned} \quad (5.3)$$

Here,  $N_{Detection}$  is the detected number by CATCH,  $N_{Reaction}$  is the original number of reactions, ( $\epsilon_{CFTthrough}$  is the probability that proton penetrates CFT, ( $\epsilon_{CFTtracking}$  is the probability that CFT can reconstruct the trajectory of proton, ( $\epsilon_{BGO}$  is the probability that the BGO calorimeter can correctly measure the energy of proton.

The method to obtain each efficiency and its result are explained below. Since elastic scattering reactions are evaluated in this time, the incident angle  $\theta$  and the energy of scattered particle correspond to each other. Therefore, the efficiency was evaluated as a function of  $\theta$  for each reaction.

### 5.9.3 Probability of proton penetration CFT

The probability that the scattered protons penetrate the CFT ( $\epsilon_{CFTthrough}$ ) is discussed in this section. The other efficiencies are estimated by using the actual measured value, but only this term was estimated from a simulation, because the number of the reactions is an unknown quantity from the measurement. In the simulation, protons were generated with angles  $\theta$  and energies according to kinematics, and it was investigated whether they passed through CFT or not. In the simulation, since the deviation of the fiber position could not be reproduced, the scattering angle  $\theta$  is artificially spread so as to simulate the actual angular resolution.

Here, the ambiguity of the simulation should be discussed. In the simulation, cylinders with thickness of 0.75 mm were used instead of the CFT spiral layers because it was not easy to reproduce the spiral layer structure for fiber by fiber in the simulation. Although the thickness is the same with the fiber diameter, the path length in the fibers are different due to the fiber position structure. Figure 5.38 shows the path length in fibers at an incident angle of  $\theta = 45$  degree. If a particle passes through the gap between fibers, the energy deposit in fibers become small. On the other hand, if the particle passes through some fibers, the energy deposit in CFT becomes larger.

The averaged path length in fiber depends on the incident angle. When  $\theta$  is 90 degree, which means vertical direction to the layer plane, the average path length was calculated to be 0.77 mm. Depending on the  $\theta$ , the averaged path length become thicker about 0.2 mm at maximum.

In order to estimate the uncertainty of the path length of 0.75 mm to 0.95 mm, the simulation with each thickness was performed. Both the thickness cases were estimated as shown in Figure 5.39, and their difference is treated as the uncertainty of the  $\epsilon_{CFT\text{through}}$ .

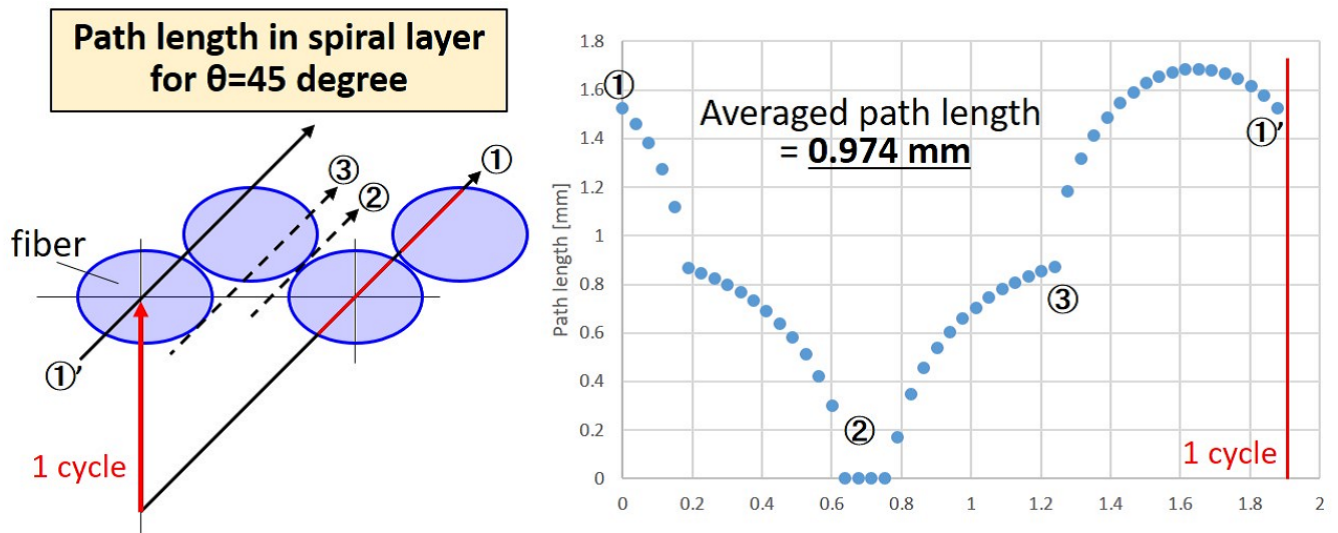


Figure 5.38: The path length in fibers of a CFT spiral layer. If a particle passes through the gap between fibers, the energy deposit in fibers becomes small. On the other hand, if the particle passes through some fibers, the energy deposit in CFT becomes larger.

Also, since it is required that there is a hit on the opposite side of the CFT track for reaction identification for the  $pp$  scattering events, the same condition is also requested here.

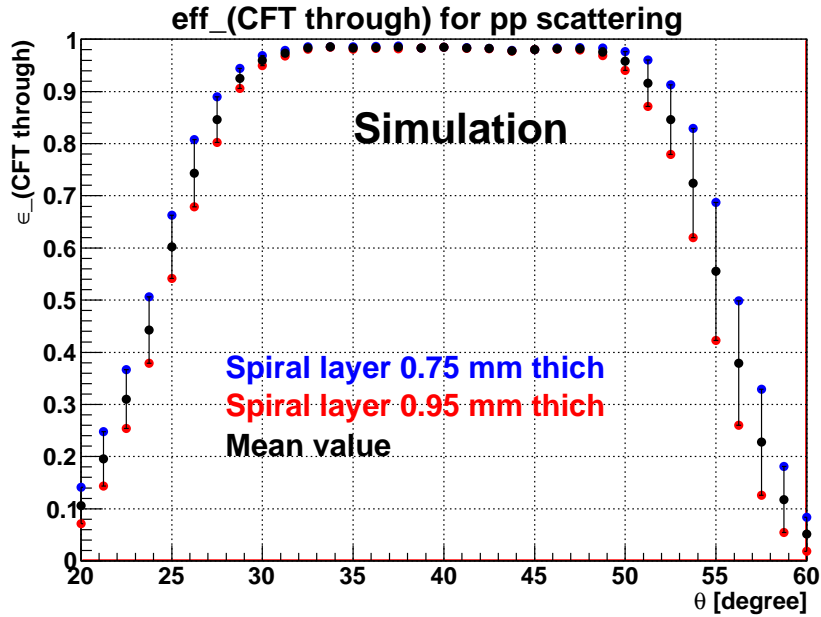


Figure 5.39: Using the  $pp$  scattering events generated in the simulation, the efficiency plotted in the vertical axis is obtained as the probability that at least one emitted proton passes through CFT and the proton at the opposite side also gives a hit to CFT. The simulation was performed with the thickness of 0.75 mm to 0.95 mm for each spiral layer. The difference between these results was treated as the uncertainty of the  $\epsilon_{CFT\text{through}}$ .

As confirmed from Figure 5.39, the efficiency decreases at the forward angle and the large angle regions.

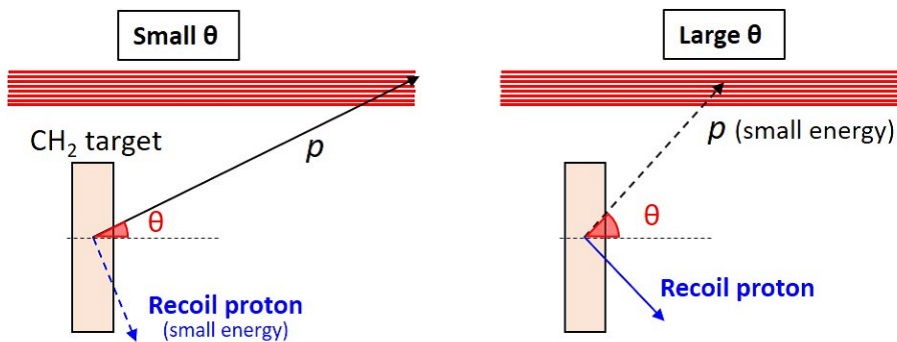


Figure 5.40: Pictures show the reason why  $\epsilon_{CFT\text{through}}$  becomes small at both ends of the acceptance range for  $pp$  scattering.

The reason that the  $\epsilon_{CFTthrough}$  decreases at an angle in the forward direction is that the energy of the proton on the opposite side detected by CFT decreases and stops in the target or in the air before reaching to CFT. Of course, if it goes to the front or other directions before reaching the outermost layer of CFT, it becomes out of acceptance and  $\epsilon_{CFTthrough}$  becomes small.

For angular regions at  $\theta$  50 degree, because the energy of scattered proton becomes small, it is considered that the proton becomes easier to stop in CFT.

In this way, the influence of the estimation conditions such as the amount of material becomes large in the region where the  $\epsilon_{CFTthrough}$  changes suddenly, and the ambiguity becomes large. On the other hand, almost the same results are estimated in the central  $\theta$  region.

$\epsilon_{CFTthrough}$  for  $pC$  scattering was also obtained from a similar simulation. In the case of  $pC$  scattering, the opposite hit in CFT was not required for the event selection.

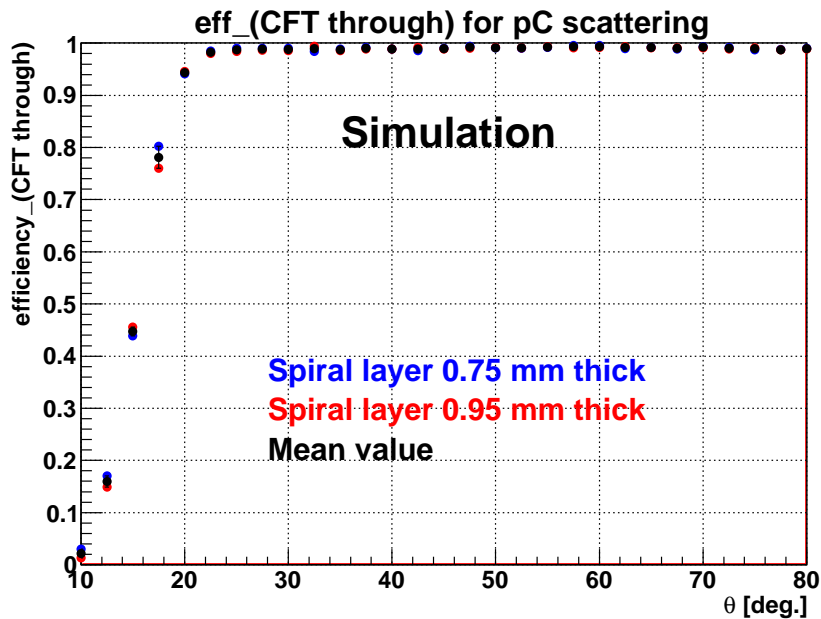


Figure 5.41: Using the  $pC$  scattering events generated in the simulation, the efficiency plotted in the vertical axis is obtained as the probability that at least one emitted proton passes through CFT. The ratio was estimated for each scattering angle with 2 types of the layer thickness of the CFT spiral layer in the simulation.

When comparing  $\epsilon_{CFTthrough}$  for  $pp$  and  $pC$  scattering reactions, the higher

probability of passing through CFT is estimated, since the energy of scattered proton from pC scattering is larger. This estimation also includes uncertainty considering of the thickness of CFT adhesive.

#### 5.9.4 Probability that CFT reconstructs trajectory of proton

After the scattered protons penetrate the CFT, their tracks were reconstructed by CFT tracking analysis. Even in the penetrating events, there are cases in which a trajectory was not obtained due to the inefficiency of layers of CFT. Therefore, it is necessary to evaluate the probability that the trajectories are obtained by CFT.

As mentioned in the previous section, the fiber position accuracy depends on the layer, the segment, and the  $z$  position.

In order to obtain the detection efficiency for each layer, the hit position which is predicted from a tracking analysis without using the information of the evaluated layer is compared with the actual hit position as shown in Figure 5.42.

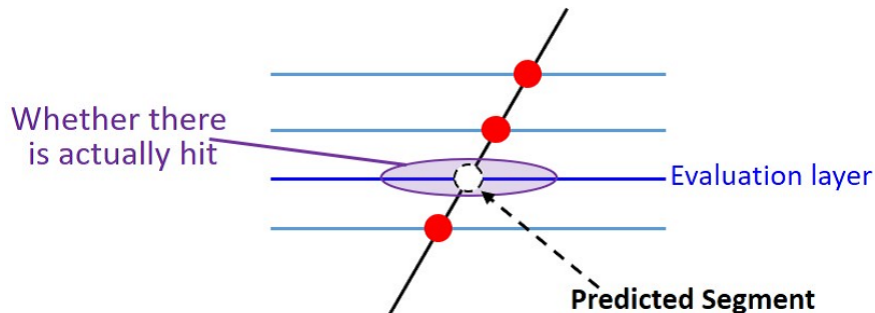


Figure 5.42: Explanation of analysis method for obtaining CFT detection efficiency. The segment number of hit fiber is predicted from other layers, and the actual hit segment number is compared with this predicted one.

The difference between the predicted position and the actual hit position is shown in Figure 5.43. In this analysis, if  $\Delta_{segment}$  is larger than 50, it is regarded as accidental hit irrelevant to the efficiency evaluation.

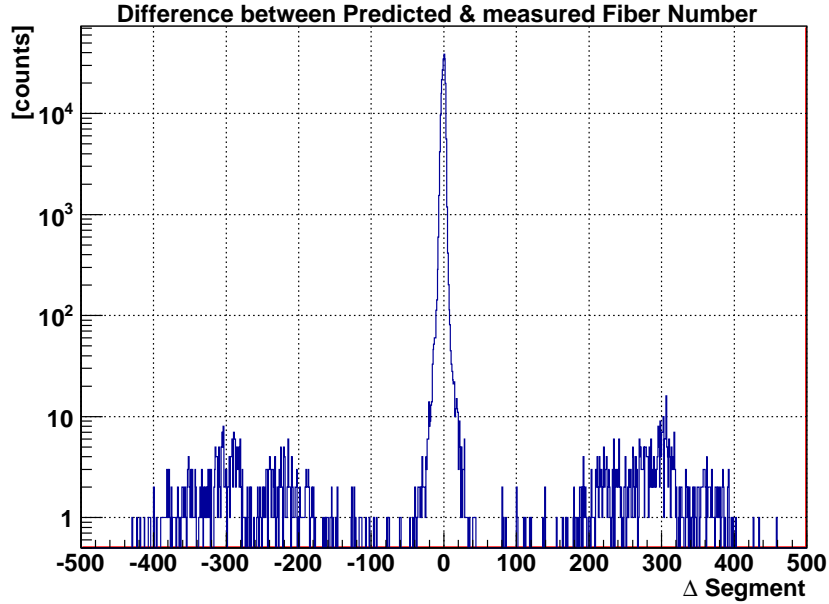


Figure 5.43: The distribution of the difference between the fiber segment number expected from the other layers and the number detected actually. It is not plotted if there is no actual hit. The events in the large  $\Delta_{segment}$  region are due to accidental hits.

The detection efficiency of each CFT layer is obtained by the following equation.

$$\epsilon_{CFT\text{detection}}(layer) = \frac{N_{hit}(\Delta_{seg} \simeq 0)}{N_{predicted}} \quad (5.4)$$

Here,  $N_{predicted}$  is the number of hits expected from the other layers  $N_{hit}(\Delta_{seg} \simeq 0)$  is the actually detected number around the predicted position.

Figure 5.44 shows the detection efficiency in this way. Furthermore, the probability of three or four hits in these layers is obtained as the tracking efficiency of the CFT straights layer as shown in right Figure 5.44.

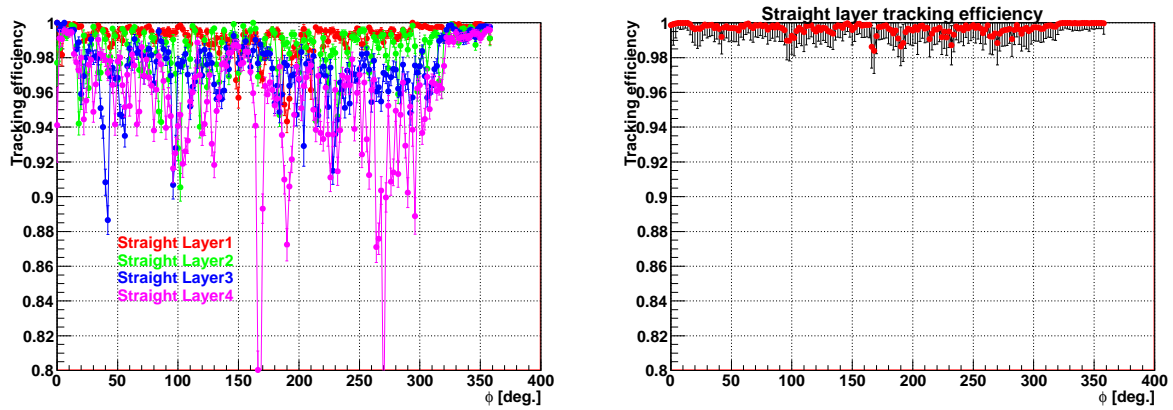


Figure 5.44: The left figure shows  $\phi$  dependence of the detection efficiency of each CFT straight layer obtained from tracking with the other layers and actual hits. The right figure shows the tracking efficiency when requiring three or four hits in the four straight layers.

From Figure 5.44, it was found that the detection efficiency of each layer has locally low efficiency in some regions. This is considered to be caused by poor positional accuracy in the assembly of the fibers, or difficulty in detecting hit due to MPPC readout problems. Therefore, there is no correlation between  $\phi$  dependence in each layer. For the tracking efficiency of the straight layer, an average of 99.7 % was obtained. Tracking efficiency was also slightly smaller in the area which is considered to have the influence of the fiber fixing frames of the spiral layers.

The spiral layer was analyzed in the same way, and result was obtained as shown in Figure 5.45.

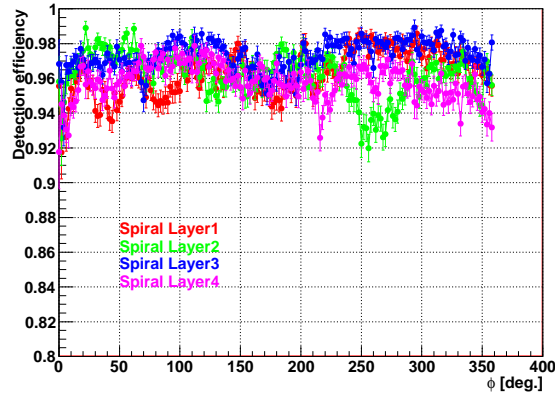


Figure 5.45: The left figure shows  $\phi$  dependence of the detection efficiency of each CFT spiral layer obtained from tracking with the other layers and actual hits.

The difference between the efficiency of straight and the spiral layers is discussed after confirming the  $\theta$  dependence of the efficiency. The  $\theta$  dependence of the efficiency of CFT straight layers was similarly obtained and shown in Figure 5.46. The detection efficiency of the straight layers is considered structurally independent of  $\theta$ , and it certainly was confirmed that there is not large  $\theta$  dependence.

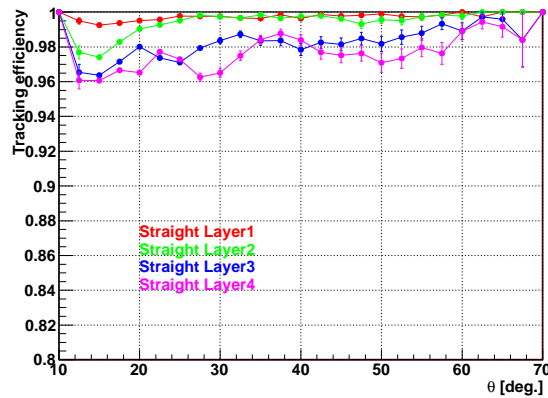


Figure 5.46: The left figure shows  $\theta$  dependence of the detection efficiency of each CFT straight layer obtained from tracking with the other layers and actual hits.

Also, Figure 5.47 shows the  $\theta$  dependence.

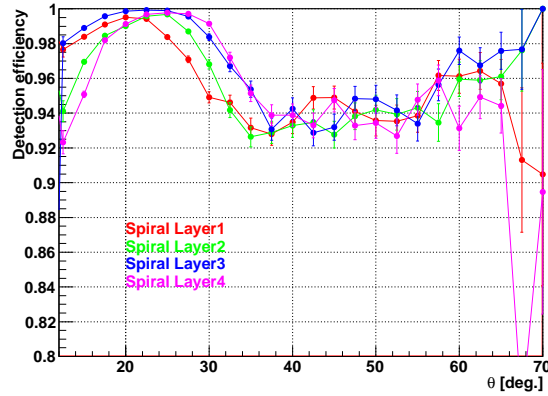


Figure 5.47: The  $\theta$  dependence of the detection efficiencies of each CFT spiral layer obtained from tracking of other layers and actual hits.

In this spiral layer, because the fibers are arranged as shown in Figure 5.48, the probability of getting through the gap between the fibers becomes high in the specific  $\theta$ .

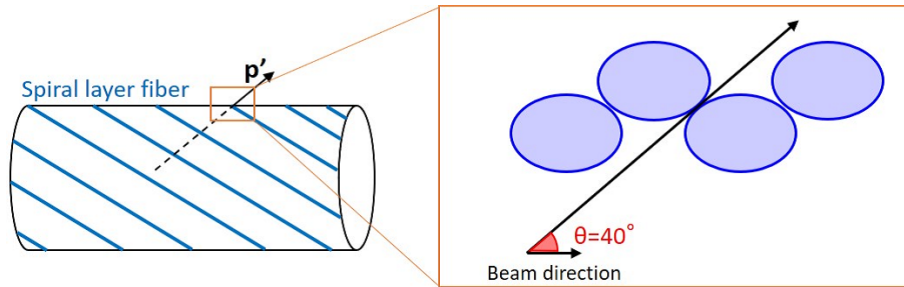


Figure 5.48: Structure of CFT spiral layer. The probability of getting through the gap between the fibers becomes high in the specific  $\theta$ .

As described above, the characteristics of the detection efficiency of each CFT layer are understood.

In order to obtain the tracking efficiency of CFT, the number of events in which the proton energy is measured by the BGO calorimeter was used as “number of CFT passing events”. Those events that reached the BGO should have passed CFT. However, in the case where the flight direction is changed in the CFT, the trajectory can not be reconstructed. Since this probability largely depends on the energy of proton and  $\theta$ , the efficiency should be estimated as functions of the proton energy and  $\theta$ . Because the energy of proton can

not be obtained from CFT measurement only, the energy deposit in the BGO calorimeter was used.

The tracking efficiency can be expressed as,

$$\epsilon_{CFT\text{tracking}} = \frac{N_{(CFT\text{ tracked})}}{N_{(proton\ reached\ BGO)}}, \quad (5.5)$$

where  $N_{(proton\ reached\ BGO)}$  is the number of detected proton by the BGO calorimeter and  $N_{(CFT\text{ tracked})}$  is the number of events for which the tracking is successful (we call it “tracked events”). In order to obtain the tracking efficiency of CFT for  $pp$  scattering, the BGO hit and the hit of CFT at the opposite side are required in the denominator. Figure 5.49 shows the illustration of the method to obtain the CFT tracking efficiency with BGO hit.

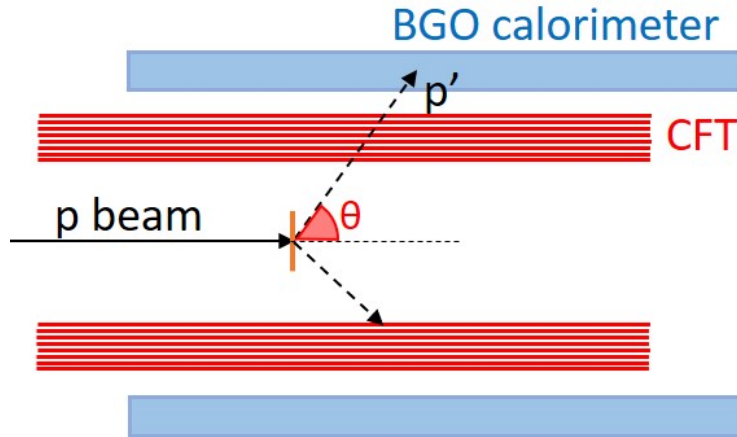


Figure 5.49: The illustration of the method to obtain the CFT tracking efficiency with BGO hit.

Figure 5.50 shows the correlation between the energy measured by the BGO calorimeter and the scattering angle  $\theta$  measured by CFT. The scattering angle  $\theta$  can be estimated from the energy measured by the BGO calorimeter by using this correlation.

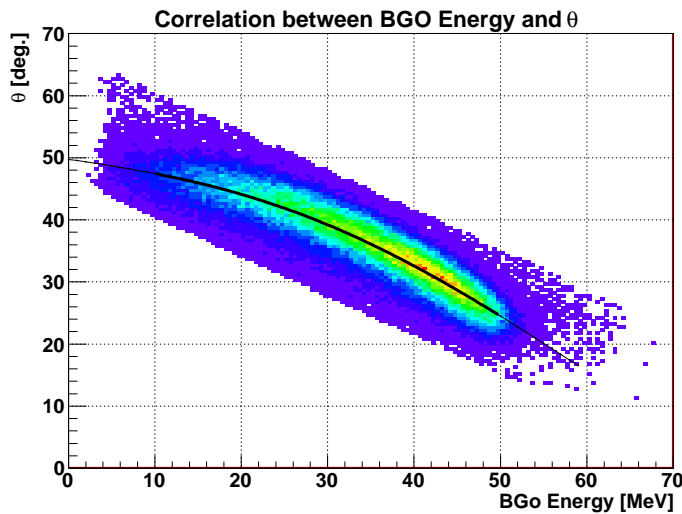


Figure 5.50: The correlation between the energy measured by the BGO calorimeter and the scattering angle  $\theta$  measured by CFT. The scattering angle  $\theta$  can be estimated from the energy measured by BGO calorimeter by using this correlation.

In the low energy region of the BGO calorimeter, we could not convert from the energy to  $\theta$  precisely due to their correlation and the energy resolution of the BGO calorimeter. Therefore, the evaluation range was decided to be less than  $\theta$  of 45 degree.

Tracking efficiency of CFT was obtained as a function of the energy of proton measured by the BGO calorimeter. After that, by converting the BGO energy to the scattering angle  $\theta$ , the  $\theta$  dependent result was obtained as shown in Figure 5.51

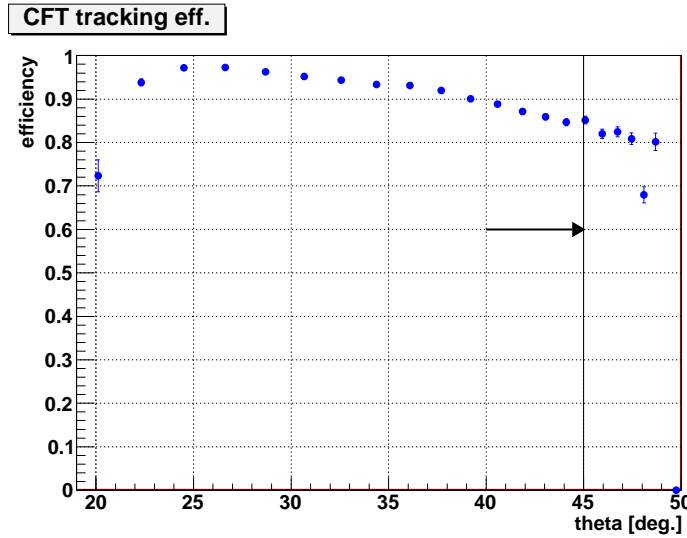


Figure 5.51:  $\theta$  dependence of the CFT tracking efficiency in which  $\theta$  is estimated from the energy of protons measured by the BGO calorimeter.

As the scattering angle  $\theta$  increases, the proton energy decreases, and the probability of reconstructing the track will be smaller due to multiple scattering in CFT materials.

It seems that there is an influence of the structure of the arranged fibers. However, it is considered that it depends more on the proton energy in the  $pp$  scattering event.

### 5.9.5 Probability that BGO calorimeters measure the energy correctly

For the events in which the protons pass through the CFT and the trajectories are obtained from the CFT tracking analysis, the probability that the protons are incident on the BGO calorimeter and the energy is measured correctly ( $\epsilon_{BGO}$ ) should be evaluated. This value includes the effect of BGO calorimeter's geometrical acceptance. Also this value includes the effect from a light shielding sheet on the outside of the CFT, a reflecting material and a light shielding sheet used to wrap the BGO crystals. Due to such materials, the protons may sometime be stopped and not to enter the BGO calorimeter with a probability.

$\epsilon_{BGO}$  is obtained from following formula.

$$\epsilon_{BGO} = \frac{N(BGO \text{ measured events})}{N(CFT \text{ tracked events})} \quad (5.6)$$

Here, the denominator *CFT tracked events* must be obtained only from CFT analysis information. For *pp* scattering events accidental background events can be mostly removed by requesting hits on the opposite side of CFT, but there are not such strong selection conditions for *pC* scattering event so that other background events were included. (The selection of the *pC* scattering in the previous evaluation used the energy measured by the BGO calorimeter.) Therefore,  $\epsilon_{BGO}$  for *pC* scattering event was assumed to be the same as for the *pp* scattering.

First of all,  $\epsilon_{BGO}$  for *pp* scattering events was obtained as shown in Figure 5.52.

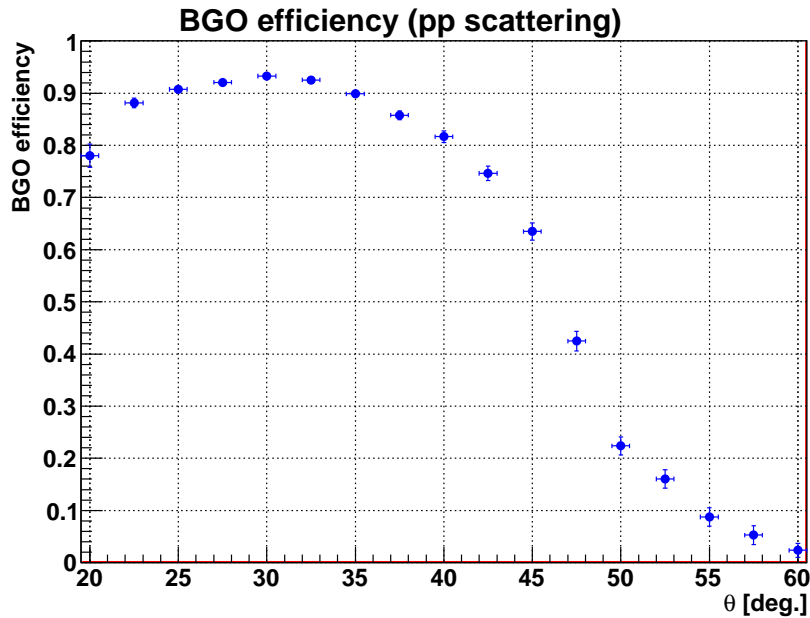


Figure 5.52: The probability that the BGO calorimeters measure the energy of protons correctly emitted from *pp* scattering.

In Figure 5.52, it is found that  $\epsilon_{BGO}$  is dropped in the forward  $\theta$  due to the acceptance of the BGO calorimeters. Also, the reason that  $\epsilon_{BGO}$  decreases at backward angles larger than around 40 degrees is considered to be due to decrease of the proton energy.

Next,  $\epsilon_{BGO}$  for *pC* scattering should be obtained. For *pp* scattering, the opposite side hit was requested in the CFT tracking for clear event selection. On the other hand, there is no similar condition for clearly selecting the *pC*

scattering event by CFT tracking alone. Even in the event with a successful CFT tracking, protons with various energies from break-up and knock-out on a carbon nuclei can not be separated from  $pp$  scattering.

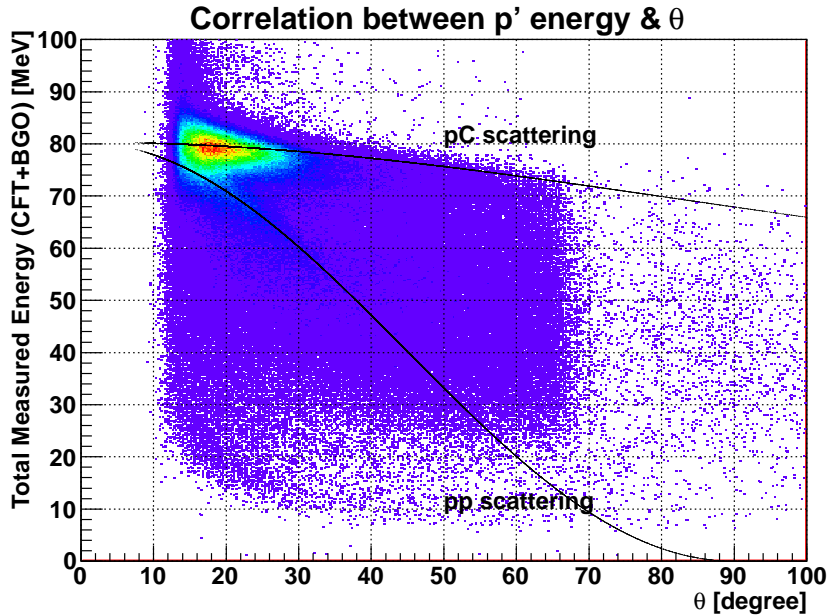


Figure 5.53: The correlation between the total energy measured by CATCH and  $\theta$ , requiring the number of tracks = 1 and non-hit on the opposite side of CFT in order to select  $pC$  scattering. There are many events away from the  $pC$  scattering kinematics shown in the solid line.

Therefore, the  $\epsilon_{BGO}$  for  $pC$  scattering was estimated from the  $\epsilon_{BGO}$  for  $pp$  scattering. For  $pC$  scattering, scattered proton energy is always larger than  $pp$  scattering. In the  $pp$  scattering, when the scattering angle is closer to 90 degree, the proton energy goes down to zero.

In other words, the  $\epsilon_{BGO}$  for  $pp$  scattering in a region with a sufficiently large proton energy ( $\theta = 30$  degree) was used as the  $\epsilon_{BGO}$  for  $pC$  scattering for the whole  $\theta$  region. Thus, the  $\epsilon_{BGO}$  obtained from the  $pp$  scattering events is also used as that of the  $pC$  scattering events as shown in Figure 5.54.

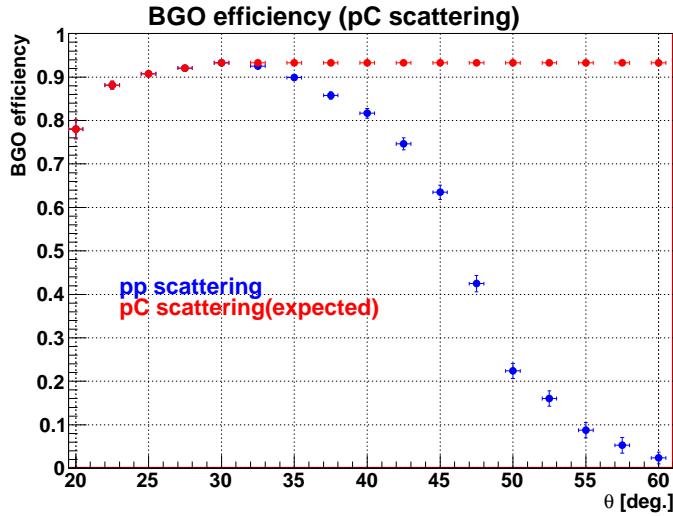


Figure 5.54: Probabilities that the BGO calorimeter can correctly measure the energy of proton. The efficiency obtained from from the  $pp$  scattering events is also used for the  $pC$  scattering events at large angles.

In order to obtain the  $\epsilon_{BGO}$  for the  $pC$  scattering events, the assumption that  $\epsilon_{BGO}$  is roughly same for the same proton energy was used. However, since the correlation between the  $\theta$  and the energy of proton is different between the  $pp$  and the  $pC$  scattering events, the conditions such as the path length in CFT are not strictly the same.

As for the calibration data in the J-PARC experiment, since protons of variety of energies are incident also in  $pp$  scattering, it is possible to use the various combination of  $(E_{p'}, \theta)$  in order to obtain  $\epsilon_{BGO}$ . Therefore,  $\epsilon_{BGO}$  will be obtained without such an assumption.

### 5.9.6 Result of cross section

All the components of the efficiency of CATCH were obtained as described in the sections above. Figure 5.55 shows the  $\epsilon_{CATCH} = \epsilon_{CFT\ through} \times \epsilon_{CFT\ tracking} \times \epsilon_{BGO}$  obtained by multiplying these components.

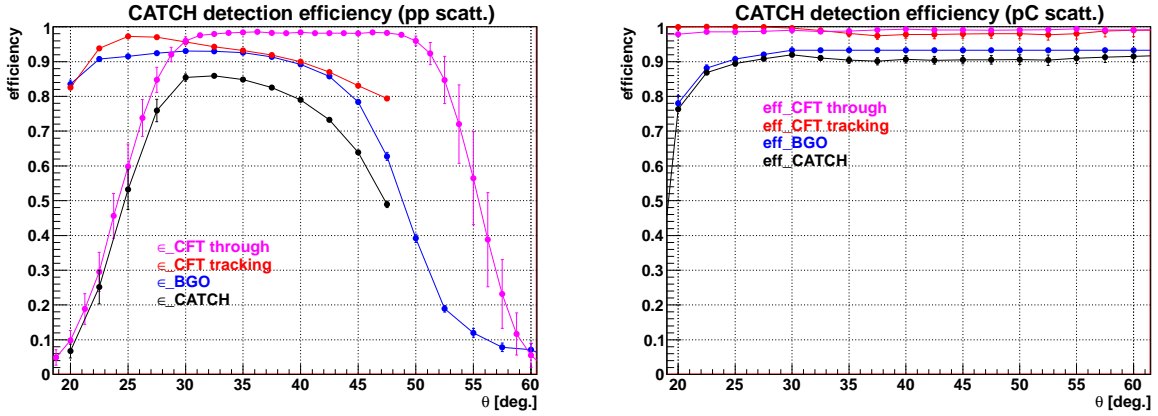


Figure 5.55: Left and right figures shows the  $\epsilon_{CATCH} = \epsilon_{CFT\ through} \times \epsilon_{CFT\ tracking} \times \epsilon_{BGO}$  for the  $pp$  and the  $pC$  scattering events obtained by multiplying these components.

As can be seen from this figure, the  $\epsilon_{CATCH}$  for the  $pp$  and  $pC$  scattering events were different. It is considered that  $\epsilon_{CATCH}$  is largely influenced mainly by the energy of the particles.

Figure 5.56 was obtained by dividing the number of detected events in Figure 5.36 by this  $\epsilon_{CATCH}$ . This reaction number corresponds to the relative value of the cross section.

To obtain the absolute value of the cross section, beam intensity, target thickness and data acquisition efficiency are necessary. Although the latter two values were measured, the uncertainty of the beam intensity measurement was large, and thus it was difficult to derive the absolute value of the differential cross section. This relative differential cross section will be used to evaluate the performance of the CATCH system.

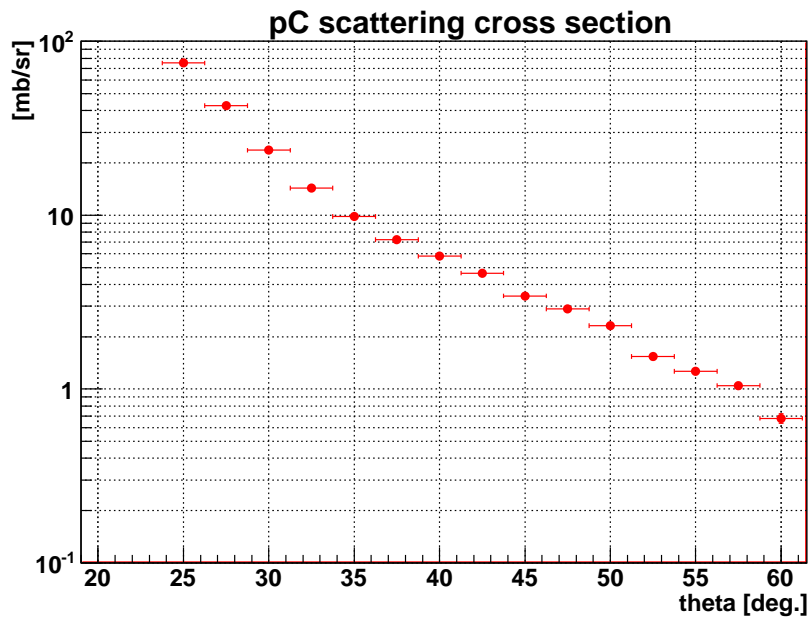
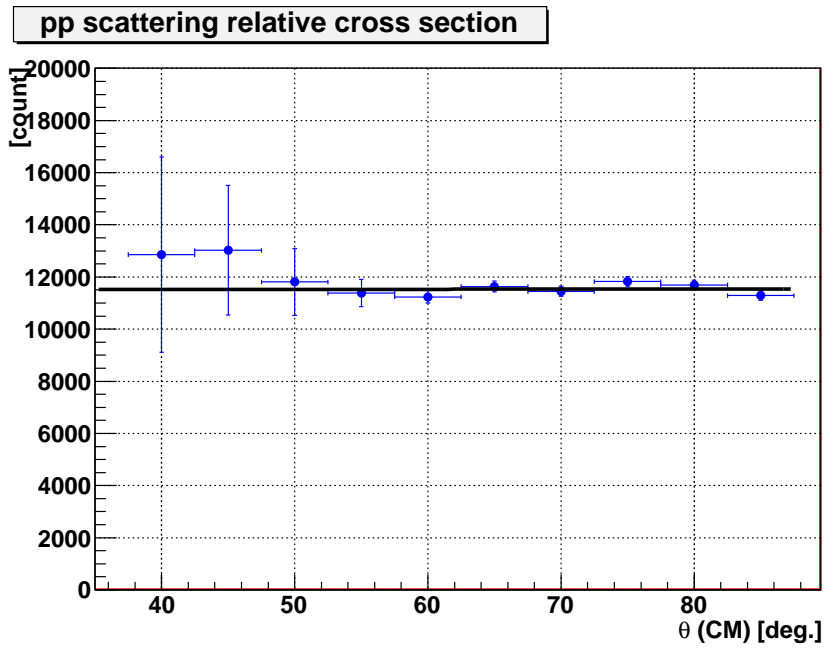


Figure 5.56: Left and right figures show the relative cross sections for  $pp$  and  $pC$  scattering, respectively. The relative cross sections were obtained from the number of events detected by CATCH and the detection efficiency and the geometrical acceptance.

In the  $pp$  scattering, the errors around both ends of the measurement region of the scattering angle is large, because the efficiency greatly changes there.

The angular correlation is obtained by fitting the data of Figure 5.56 with a straight line. As a result, the slope of the angular dependence was obtained to be  $a = 0.4 \pm 8.8$  [count/ $\theta_{rmCM}$ ] with the  $\chi^2 = 7.95$ . This dependence can be considered to be flat.

As a reference, the differential cross section of the  $pp$  scattering is obtained from a partial-wave analysis based on rich experimental data of nucleon-nucleon scattering experiment [24]. The angular dependence of the cross section with the beam energy of 80 MeV can be predicted to be flat in the region over  $\theta_{CM} = 30$  degree. Actually the result of this test experiment was consistent with the flat angular dependence as shown in Figure 5.57. The measured relative differential cross section and reference value were normalized at one point for the comparison.

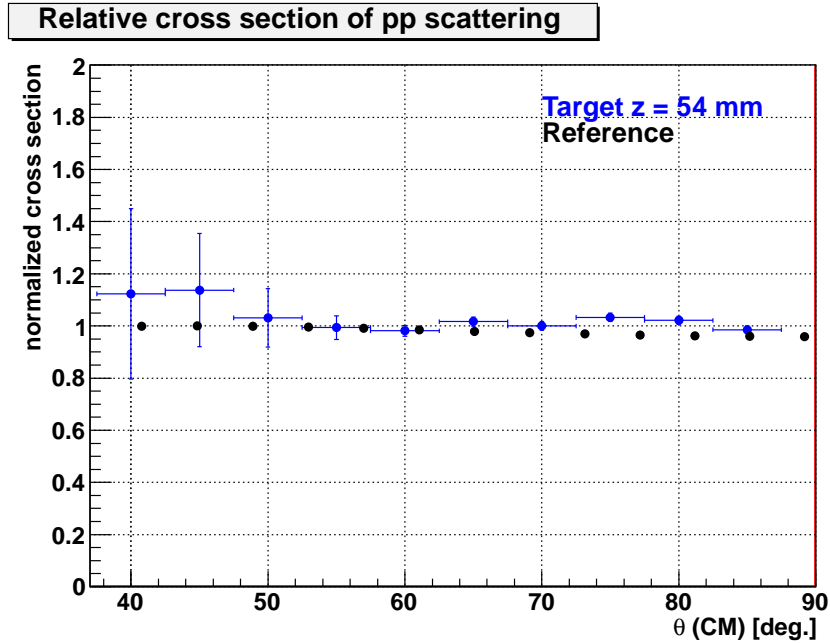


Figure 5.57: Differential cross section of the  $pp$  scattering obtained from a partial-wave analysis based on rich experimental data of nucleon-nucleon scattering experiment [24]. The angular dependence for the beam energy of 80 MeV can be predicted to be flat over the  $\theta_{CM} = 30$  degree. It was consistent with the measured relative cross section.

Here, in the  $pC$  scattering, there is contribution from not only the elastic scattering but also the excited state of carbon nuclei. There are two references

comparable with the result of the  $pC$  scattering. One is the differential cross section of the elastic scattering and inelastic scattering of excited states of a carbon nuclei[25]. However, the beam energy was 65 MeV different from this test experiment, which could not be compared with this result directly. Another is the differential cross section of only the  $pC$  elastic scattering for a 80 MeV beam[26].

Figure 5.58 shows the differential cross section of the  $pC$  scattering from a past experiment [25]. The beam energy of the past experiment was 65 MeV, and that of this test experiment was 80 MeV.

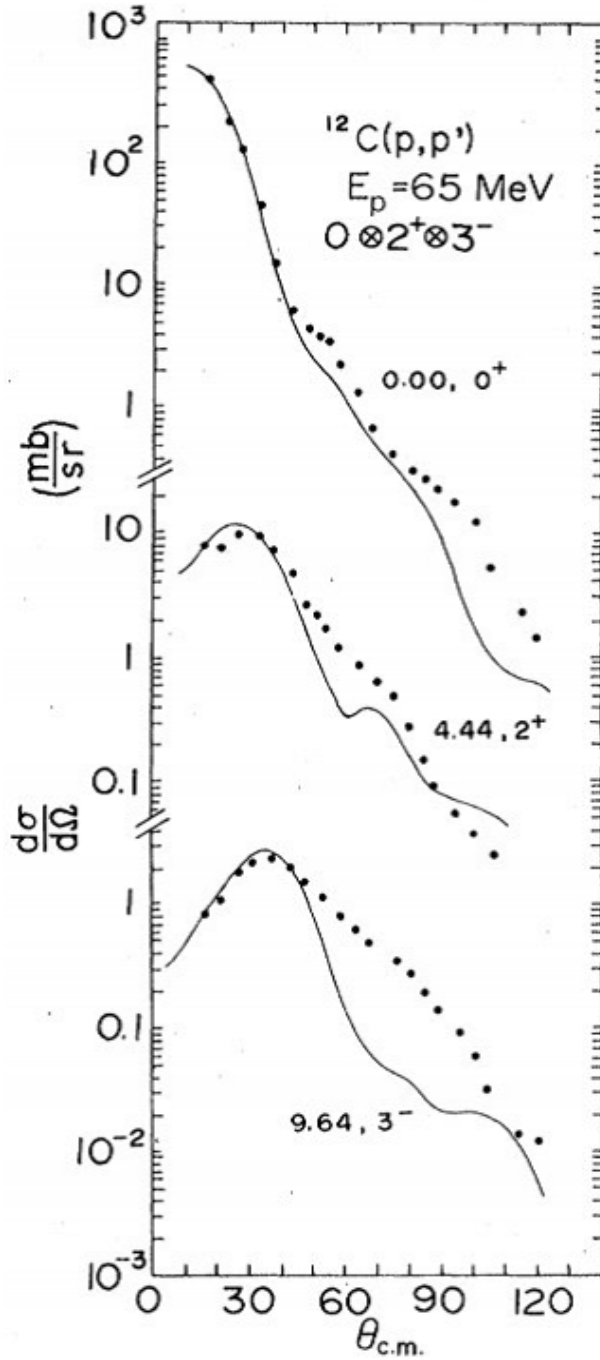


Figure 5.58: The differential cross section of the  $pC$  scattering from a past experiment [25]. The beam energy of this past experiment was 65 MeV, and that of the CATCH test experiment was 80 MeV.

From Figure 5.58, at  $\theta = 25$  degree, the ratio of elastic to inelastic scatterings

is 12.4 times larger, and at  $\theta = 35$  and 45 degrees 2 and 1.8 times larger, respectively. In addition, the momentum transfer to the carbon target becomes larger in the large scattering angle, and the probability of producing the  $^{12}\text{C}(2^+)$  excited state at 4.4 MeV should be larger. Figure 5.59 shows the  $\Delta E$  distribution of the  $pC$  scattering at  $\theta = 25, 35, 45$  degrees in the actual measurement. The peak at  $\Delta E = 0$  corresponds to the  $pC$  elastic scattering event.

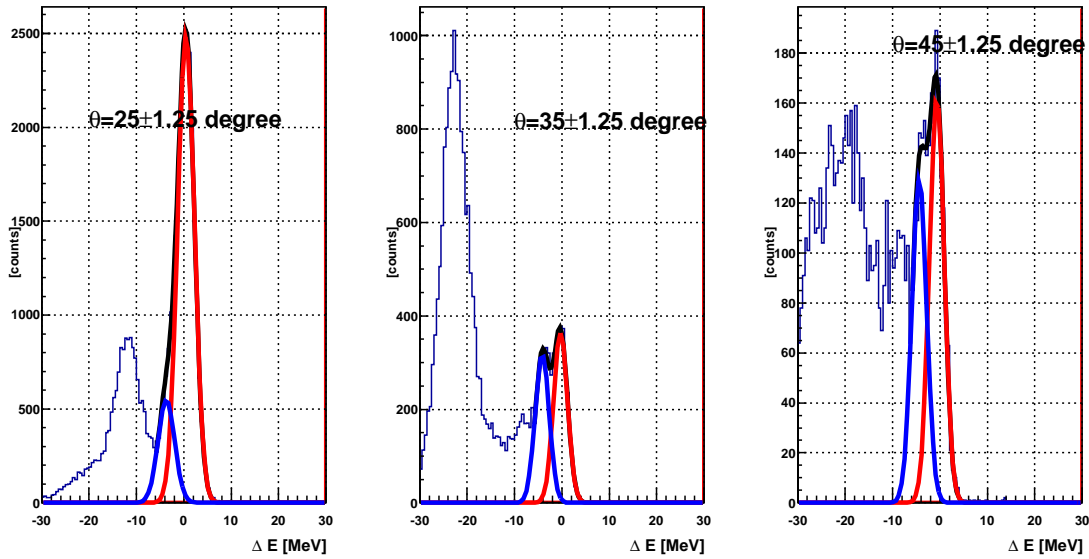


Figure 5.59: The  $\Delta E$  distribution of the  $pC$  scattering at  $\theta = 25, 35, 45$  degrees obtained from the test experiment with CATCH system. Each distribution is fitted with two Gaussian functions for the elastic scattering ( $\Delta E = 0$ ) and the first excited state ( $\Delta E = 4.4$  MeV).

Since the result of the past experiments, which can be compared under the same conditions with this test experiment, gives the cross section of the elastic scattering only, it is necessary to estimate the number of the elastic scattering events from these  $\Delta E$  distributions. However, with the  $\Delta E$  resolution of CATCH system, the  $\Delta E$  distribution of the  $pC$  elastic scattering overlaps with the inelastic scattering events going to the first excited state of carbon nuclei (4.4 MeV), so it is difficult to obtain the number of the elastic scattering events exactly.

Therefore, we tried two kinds of fitting of  $\Delta E$  distribution and evaluated the angular range where the present measurement can be compared with the

cross section in the past experiment. One method is to fit the  $\Delta E$  distribution at  $-3 \leq \Delta E \leq 30$  MeV in order to avoid the mixing of the excited states distributed around  $\Delta E = -4.4$  MeV and above. Another method is to use two Gaussian functions for the ground state and the first excited state of 4.4 MeV. Figure 5.60 shows the two fitting methods for the same  $\Delta E$  distribution of the  $pC$  scattering.

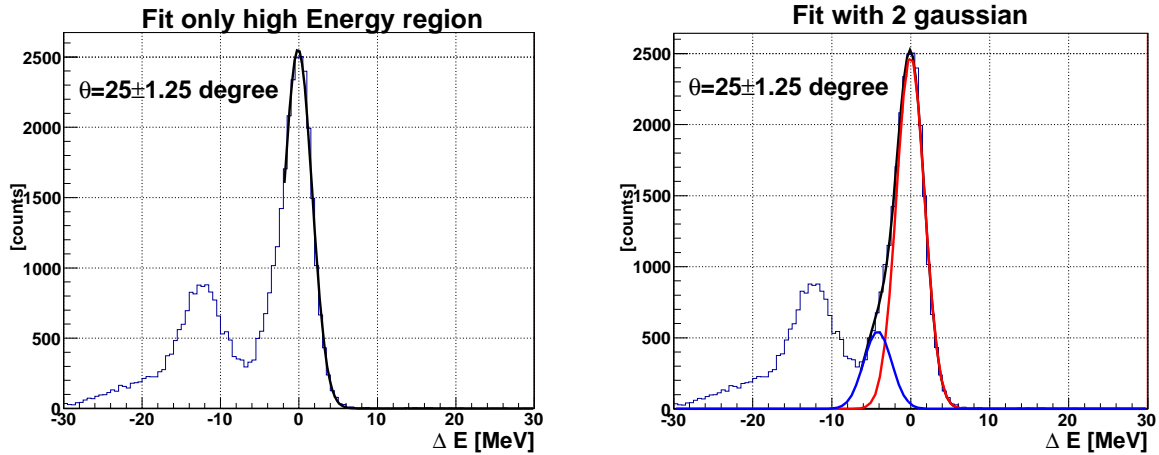


Figure 5.60: The two fitting methods for the same  $\Delta E$  distribution of the  $pC$  scattering. Left figure shows the method to fit the  $\Delta E$  distribution at  $-3 \leq \Delta E \leq 30$  MeV in order to avoid the mixing of the excited states distributed around  $\Delta E = -4.4$  MeV. Right figure shows the method to use two Gaussian function for the ground state and the first excited state of 4.4 MeV.

Figure 5.61 shows the relative differential cross section of the  $pC$  scattering derived using the two fitting methods for counting the number of the identified events and the detection efficiency of CATCH system. Right figure of Figure 5.61 shows the residual distribution obtained by normalizing the result of the past experiment at  $\theta = 25$  degree.

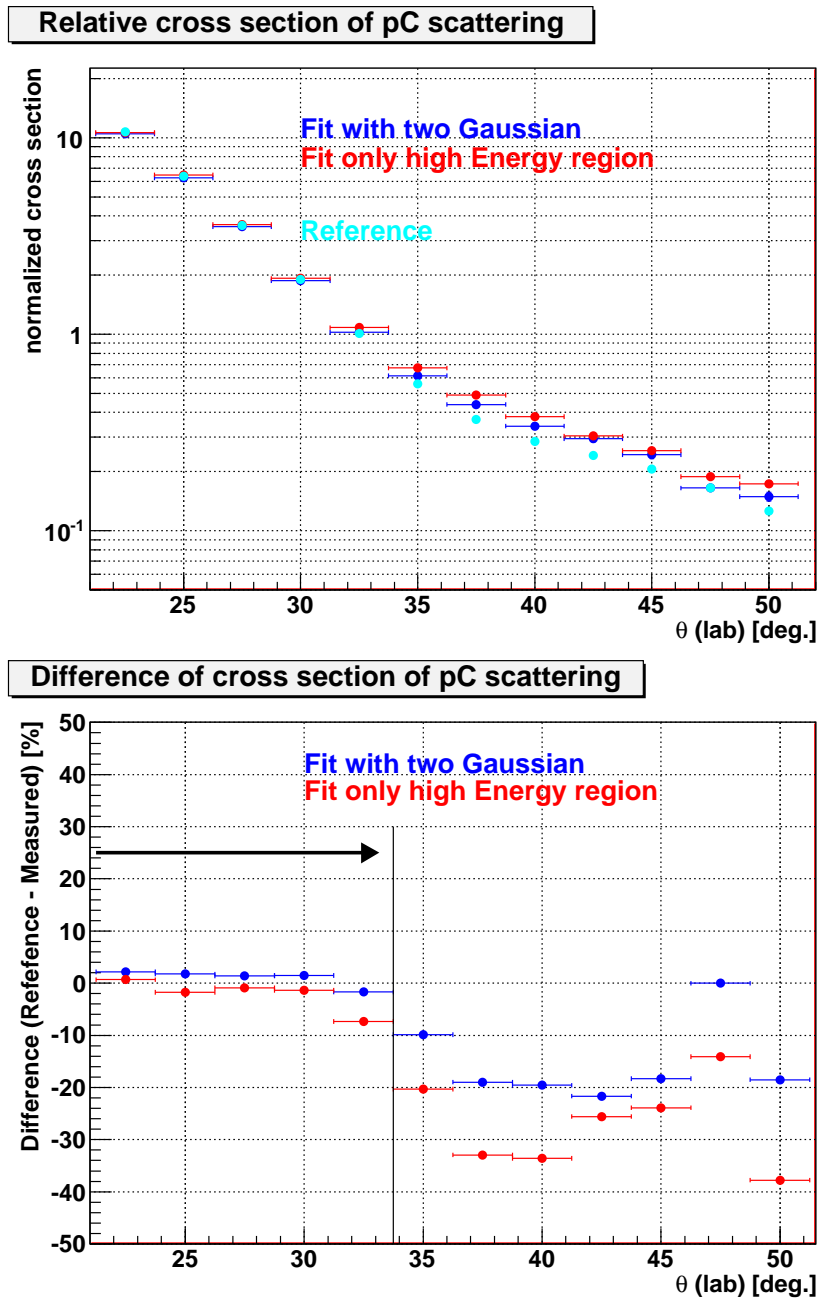


Figure 5.61: Left figure shows the relative differential cross section of the  $pC$  scattering derived using the two fitting methods for the  $\Delta E$  distribution. The result of the past experiment[26] is normalized at  $\theta = 25$  degree. Right figure shows the residual distribution.

In this way, it was difficult to extract only the elastic scattering events from the  $\Delta E$  distribution including the inelastic scattering events in large  $\theta$  region. However, in region of  $\theta < 35$  degree, the difference between the two methods is small and the residual values are within  $\pm 10\%$ . This suggests that the number of elastic scattering events is counted successfully to compare with the past result. This angular range of  $\theta < 35$  degrees is adopted for the comparison with the past  $pC$  scattering data.

The purpose of the present analysis is not to check whether separation of the excited state is possible, but to check whether the derivation of the scattering cross section (the angular distribution of the relative cross section) is successful. Therefore, a more detailed analysis of the excited state is omitted.

The obtained performance of the CATCH system to derive the cross section here is discussed in the next section including the dependence of the target position.

### 5.9.7 The target position dependence of the derivation of the cross section

Up to this point, the analysis was done for the data with the fixed target position. However, since CATCH has a sensitive area of 400 mm in the  $z$  direction, we need to check a possible dependence on the target  $z$ -position. Furthermore, it is considered that the response to the particle trajectory depends on  $(z, \theta)$  due to the variation in the CFT fiber arrangement. Since there is only one combination of  $(z, \theta)$  to incident CFT at only one target position, so we took data with the target at three different positions. By changing the target position, the dependence of the combinations of  $\theta$  and  $z$  can be studied as shown in Figure 5.62.

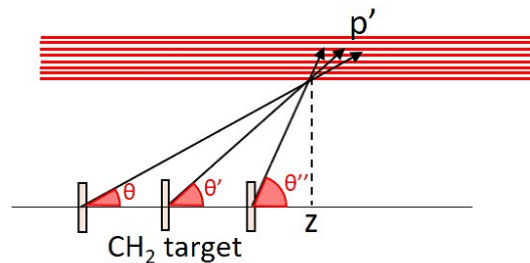


Figure 5.62: Three target positions were used to evaluate the dependence of the combinations of  $\theta$  and  $z$ .

Figure 5.63 shows the efficiency obtained for each target position. The efficiency is roughly the same for the three target positions. However, slightly differences are seen. Therefore, it was found that it is necessary to evaluate the efficiency for each  $z$  position and incident angle  $\theta$ .

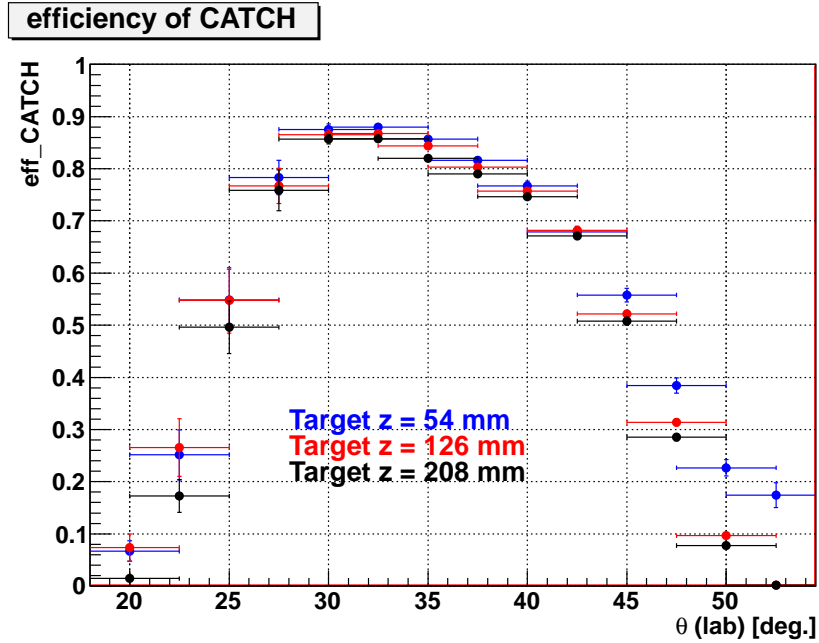


Figure 5.63: The  $\epsilon_{CATCH}$  for the  $pp$  scattering event for three target  $z$  position.

Figures 5.64 show the results of the cross sections for each target position and the results of the past experiments [26] as a reference. The relative cross section of  $pC$  scattering was normalized with the same normalize factor as that of  $pp$  scattering.

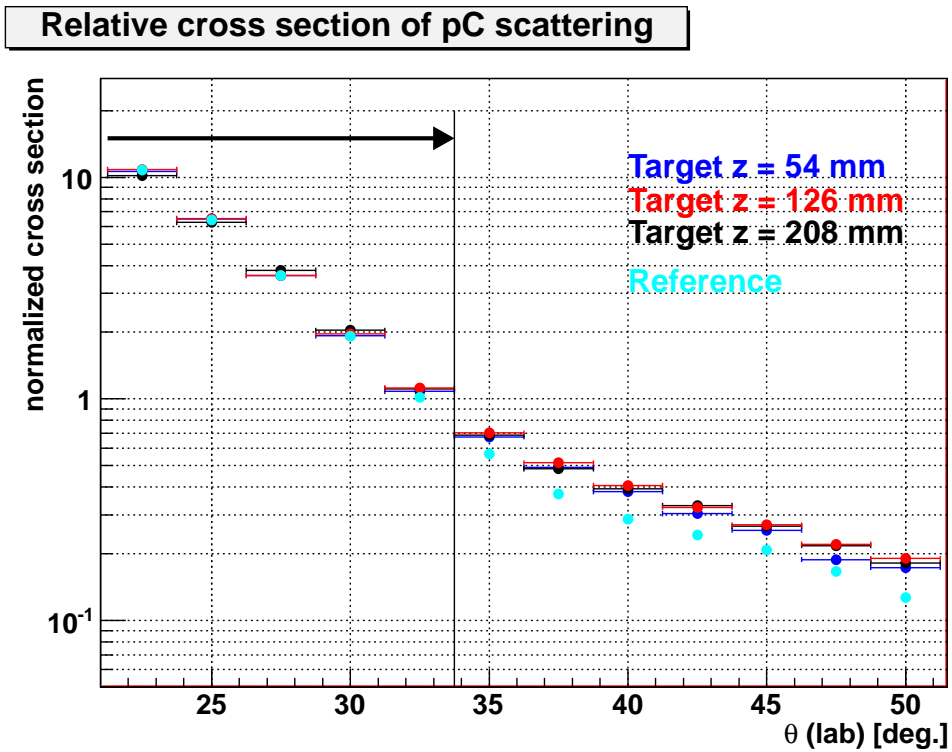
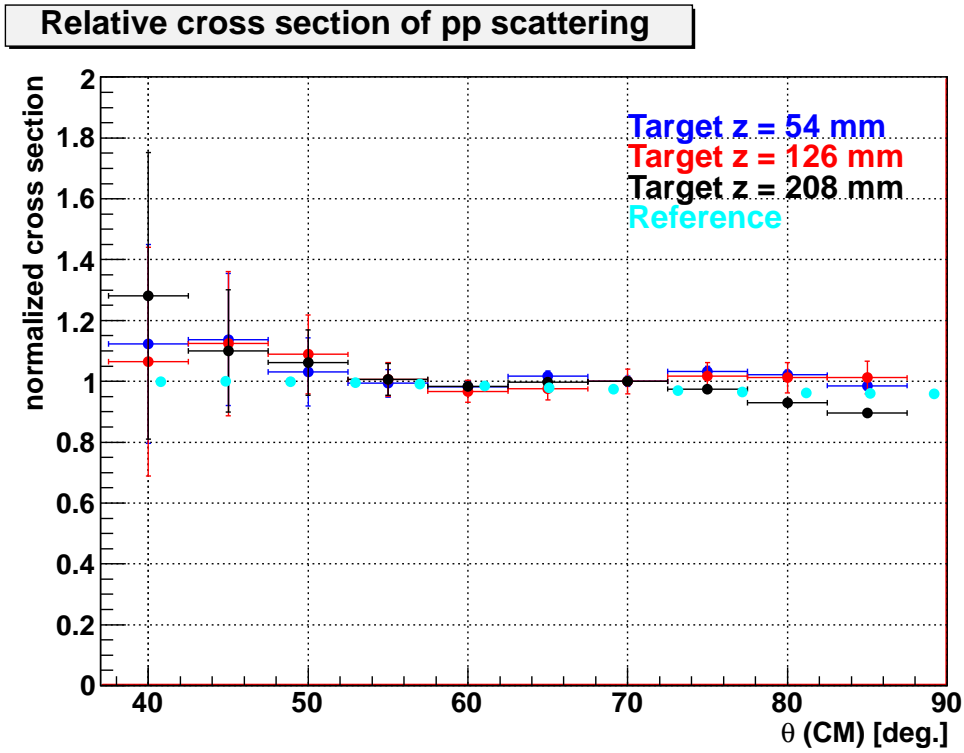


Figure 5.64: Left and right figures show the target position dependence of the cross section for  $pp$  and  $pC$  scatterings, respectively. The result of the past experiment [26] is also shown with the normalized value.

In this way, although the detection efficiency differs for each target position, the efficiency was obtained for each condition from the data, and the scattering cross sections were derived in each case. The observed slight disagreement of the cross sections in Figure 5.64 will be treated as systematic errors in the cross section when the  $\Sigma p$  scattering cross section is measured by CATCH.

The detection efficiencies of CATCH for  $pp$  and  $pC$  scatterings were analyzed separately. However, by using the same normalize factor for  $pp$  and  $pC$  scatterings, these relative cross section were considered to be obtained successfully. It means that the each analysis methods does not have the serious problem.

There are large errors especially in both ends of the measured angular region in  $pp$  scattering events. The reason for this error is considered to be due to the ambiguity of the estimation of the detection efficiency of the CATCH system which changes greatly in the edge region. However, the accuracy of the cross section is within 10% in the center region. In addition, by comparing the results of the  $pC$  scattering event of this test experiment with that of the past experiment, it is confirmed that the  $\theta$  dependence of the relative cross section of  $pC$  scattering is consistent in the region of  $\theta < 35$  degree.

This difference is regarded as a systematic error of the analysis, and its value was obtained as shown in Figure 5.65.

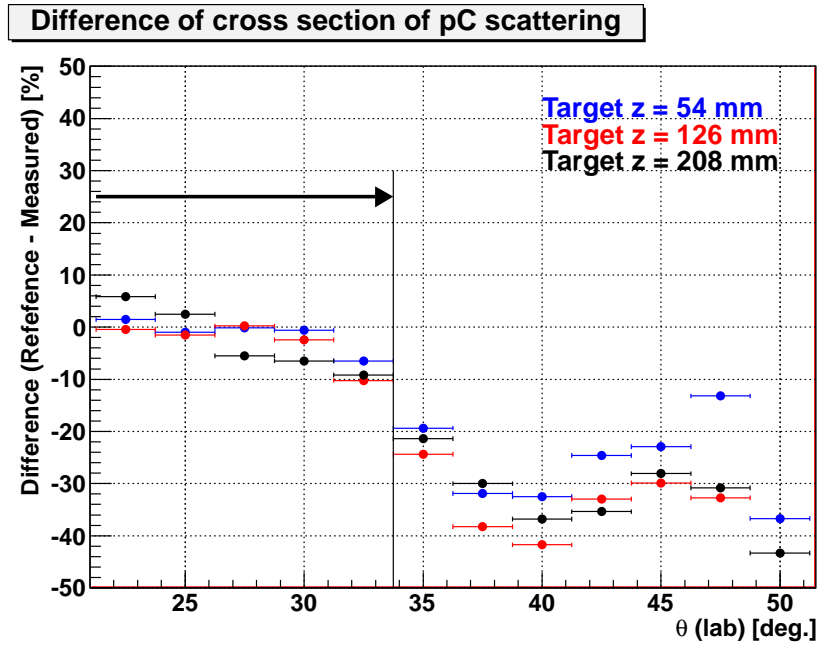


Figure 5.65: The difference between the differential cross section of the past experiment and the test experiment. This difference is regarded as a systematic error.

We have confirmed that the CATCH system has performance to measure the cross sections of  $pp$  and  $pC$  scatterings with the systematic error less than  $\pm 10\%$ . It satisfies the requirement for the  $\Sigma p$  scattering experiment of 10%.

This measurement accuracy of the cross section depends on the contribution of background events. In the next chapter, the response of CATCH in the  $\Sigma p$  scattering experiment is studied by using the performances of the CATCH system evaluated from this test experiment.

## Chapter 6

# Estimation for the $\Sigma p$ scattering experiment

Performance evaluation of the CATCH system was performed by the test experiment. Here we estimate the accuracy of the cross section measurement in the  $\Sigma p$  scattering experiment with the evaluated performances.

### 6.1 Evaluation results of CATCH performances

The performances of CATCH obtained from the results of test experiment are summarized again in Table 6.1.

Table 6.1: Summary of the evaluated performances of the CATCH system

Detectors	Requirements	Obtained performance
CFT	Time resolution	$\sigma_{time} = 1.8 \text{ ns}$
	Energy resolution	20% for 8 ~ 20 MeV proton
	Angular resolution	$\sigma_{\theta} = 1.6^{\circ}$
BGO calorimeter	Energy resolution	$\sigma_{Energy} = 1.2 \sim 1.4\%$ at 80 MeV proton

Almost all the performances satisfy the requirements. However, because the energy resolution of CFT was worse than the designed value, the energy response  $\Sigma p$  scattering events ( $\sigma_{\Delta E}$ ) should be estimated with the obtained performances.

## 6.2 $\Delta E$ resolution

Since the sensitivity of the angular resolution of CFT ( $\sigma_\theta$ ) to  $\Delta E$  strongly depends on the reaction kinematics, the  $\Delta E$  resolution ( $\sigma_{\Delta E}$ ) is evaluated for  $\Sigma p$  scattering in this section.

$\Delta E_{\Sigma p}$  is the difference between two energies obtained by two methods for the same energy of the recoil proton from the  $\Sigma p$  scattering reaction. Since  $\Delta E$  is used for identifying scattering events, its resolution is important to obtain the number of scattering events precisely.

The energy  $Ep'_{calculate}$  is obtained from the recoil angle  $\theta$  of the recoil proton, when the  $\Sigma$  beam energy and direction are measured by the spectrometer systems. The other energy  $Ep'_{measure}$  is obtained from the measurement of the proton energy by CFT and the BGO calorimeter.

The spread of  $Ep'_{calculate}$  depends on the angular resolution of CFT, and that of  $Ep'_{measure}$  depends on the energy resolutions of CFT and the BGO calorimeter. Each spread is estimated below.

### 6.2.1 The spread of the energy calculated from recoil angle

The angular resolution of CFT tracking affects the spread of  $Ep'_{calculate}$ . Figure 6.1 shows the relation between the recoil angle and the energy of the recoil proton from  $\Sigma p$  scattering. If there is a difference between the actual angle and the measured angle, the calculated energy  $Ep'_{calculate}$  also changes. The deviation of the calculated energy  $Ep'_{calculate}$  depends on the angular resolution  $\sigma_\theta$  and sensitivity of  $\theta$  to  $Ep'_{calculate}$ .

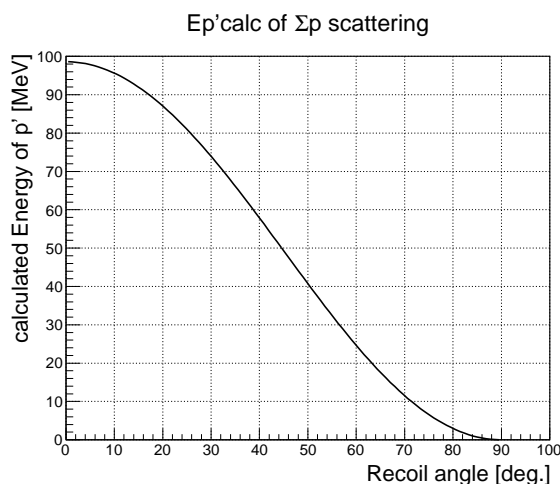


Figure 6.1: The energy  $E_{p'_{calculate}}$  calculated from the recoil angle  $\theta$  of the recoil proton from a  $\Sigma p$  scattering events. Here, the  $\Sigma$  beam energy is assumed to be 100 MeV. The deviation of the calculated energy  $E_{p'_{calculate}}$  depends on the angular resolution  $\sigma_\theta$  and sensitivity of  $\theta$  to  $E_{p'_{calculate}}$ .

Here, the angular resolution of CFT was obtained to be 1.6 degrees as described in Chapter 5. Therefore, the spread of  $E_{p'_{calculate}}$  is estimated as shown in Figure 6.2. Since the size of  $\sigma_{E_{p'_{calc}}}$  depends on the beam energy, the ratio  $(\frac{\sigma_{E_{p'_{calc}}}}{E_{p'_{calc}}})$  is also shown in Figure 6.2.

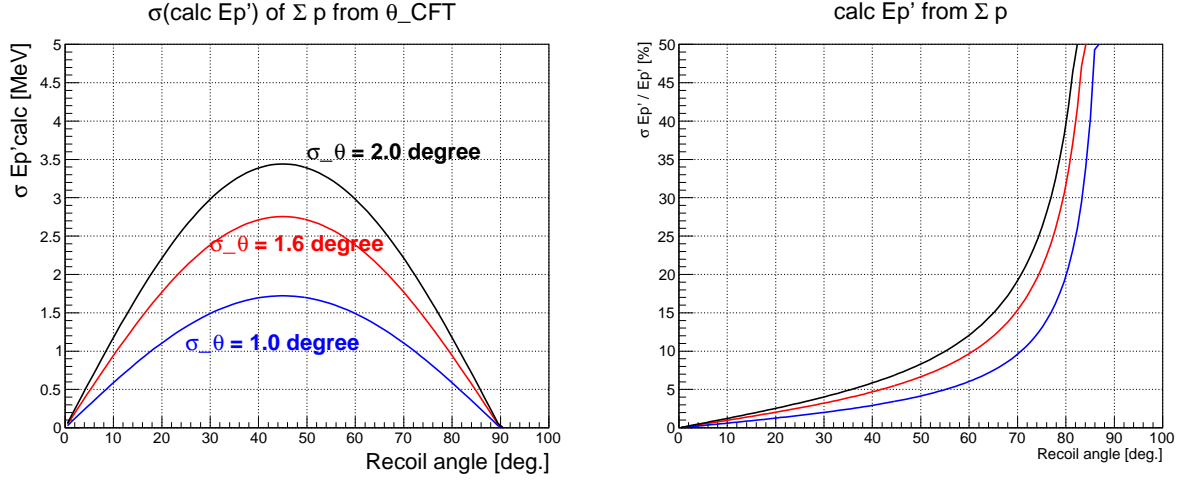


Figure 6.2: Left figure shows the energy  $Ep'_{calculate}$  calculated from the recoil angle  $\theta$  of the recoil proton from a  $\Sigma p$  scattering event. Black, red and blue lines show the result for the  $\sigma_\theta = 2$  degrees, 1.6 degrees, and 1 degree, respectively. Here, the  $\Sigma$  beam energy is assumed to be 100 MeV. Right figure shows the ratio of  $(\frac{\sigma_{Ep'_{calc}}}{Ep'_{calc}})$  which is independent of the energy of  $\Sigma$  beam.

This spread of  $Ep'_{calc}$  is the contribution of the angular resolution to the  $\Delta E$  resolution.

### 6.2.2 The spread of the energy measured by CFT and BGO calorimeter

The spreads of  $\Delta E$  for  $pp$  and  $pC$  scattering events were obtained in Chapter 5. This value includes contribution of  $\sigma_{Ep'_{calc}}$  especially in  $pp$  scattering events. On the other hand, the energy spread of  $pC$  scattering events do not depend on the  $\theta$  strongly. Therefore, the spread of  $\Delta E$  of  $pC$  scattering can be roughly regarded as  $\sigma_{Ep'_{measure}}$ . By fitting the obtained correlation between  $\sigma_{\Delta E}$  and the energy of the recoil proton with a function proportional to  $\frac{1}{\sqrt{(E)}}$ , the  $\sigma_{Ep'_{measure}}$  was estimated as shown in Figure 6.3 (right).

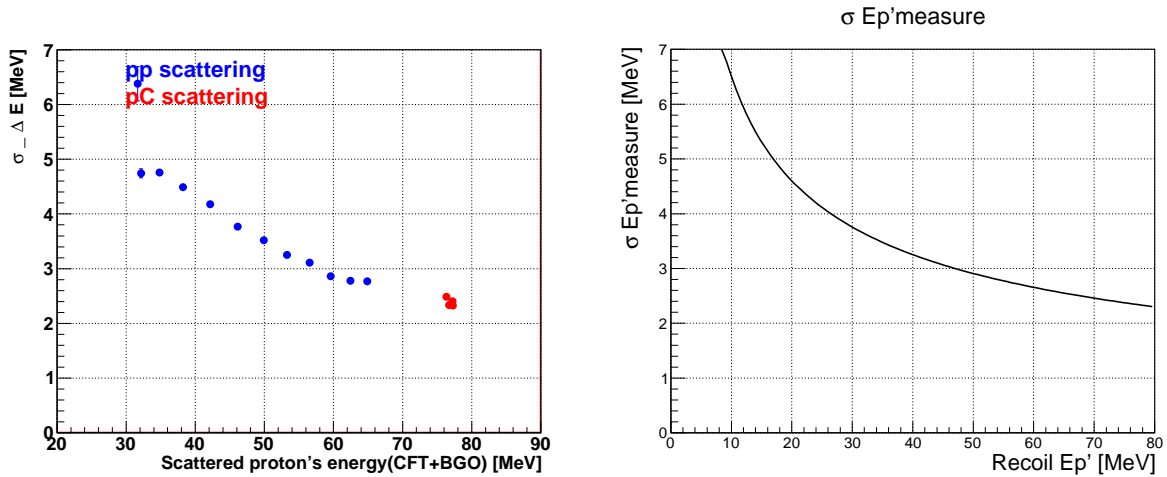


Figure 6.3: Left figure shows the correlation between  $\sigma_{\Delta E}$  and the energy of the scattered proton for  $pp$  and  $pC$  scatterings obtained the test experiment. Right figure shows the estimated  $\sigma_{Ep' \text{ measure}}$  with a function proportional to  $\frac{1}{\sqrt{(E)}}$  based on the measurement results.

### 6.2.3 The spread of $\Delta E$

The spread of  $\Delta E$  is expressed with  $\sigma_{Ep' \text{ calc}}$  and  $\sigma_{Ep' \text{ measure}}$  as following,

$$\sigma_{\Delta E} = \sqrt{\sigma_{Ep' \text{ calc}}^2 + \sigma_{Ep' \text{ measure}}^2}. \quad (6.1)$$

The  $\sigma_{Ep' \text{ calc}}$  and the  $\sigma_{Ep' \text{ measure}}$  values estimated from the evaluated performance of CATCH are shown in Figure 6.4. The  $\sigma_{Ep' \text{ calc}}$  is affected by not only the effect of the angular resolution of CFT, but also the effect of the performances of the spectrometers tagging the  $\Sigma$  production such as the momentum resolution, the angular resolution and vertex resolution of the reaction point. The total  $\Delta E$  resolution was obtained by including these spreads as shown in Figure 6.4 (bottom).

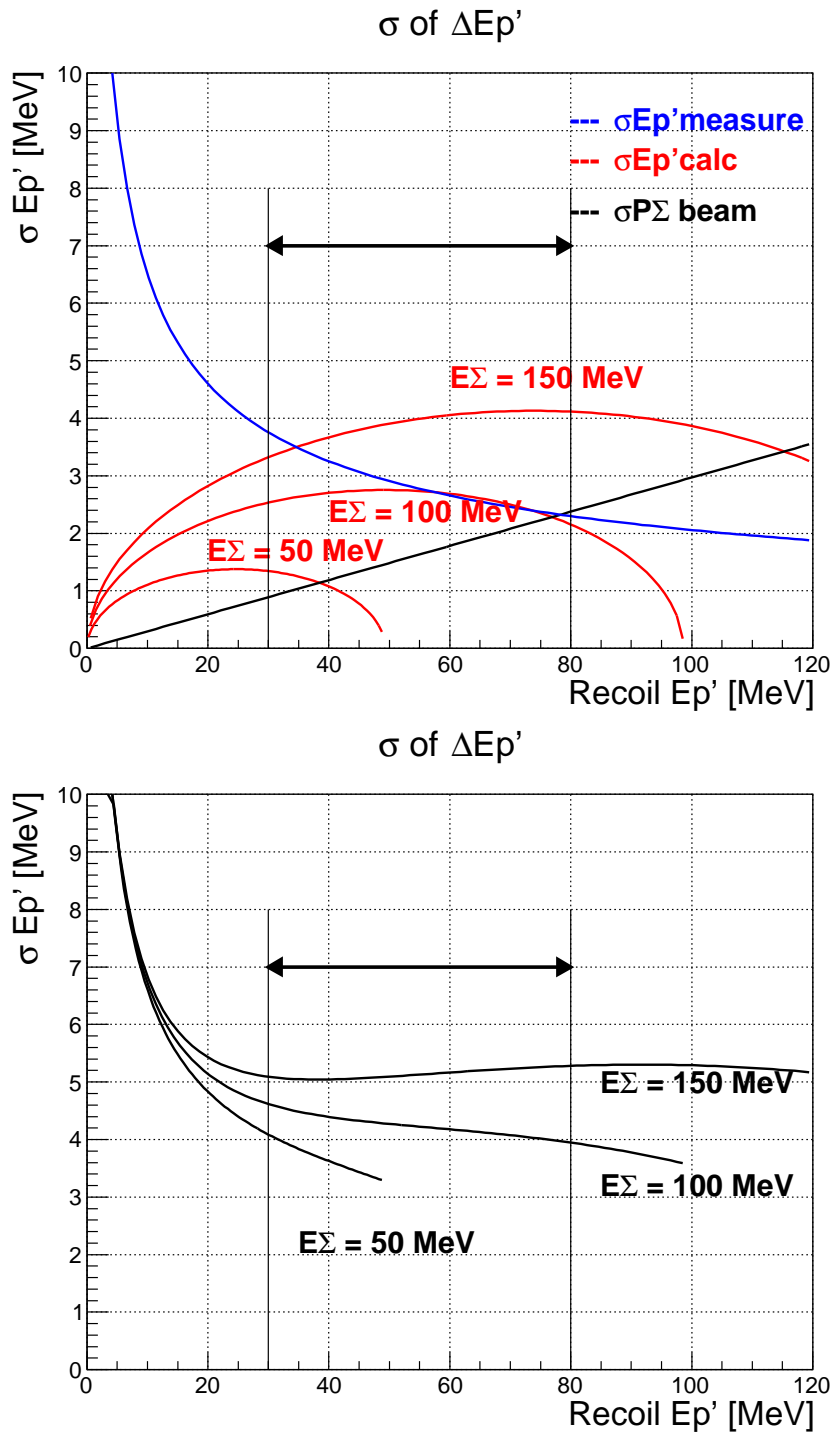


Figure 6.4: Top : Red lines and blue line show  $\sigma_{Ep'calc}$  from CFT angular resolution and  $\sigma_{Ep'measure}$  from the energy resolution of CFT and the BGO calorimeter, respectively, as a function of recoil proton energy. The  $\sigma_{Ep'calc}$  is the calculated energy spread of recoil proton assuming that the angular resolution of CFT is  $\sigma_{\theta} = 1.6$  degrees. The range of the arrow means the actually measured region of in this test experiment. Black line shows  $\sigma_{Ep'calc}$  affected by the performances of the spectrometers tagging the  $\Sigma$  production. Bottom : Total  $\Delta E$  resolution including the three spreads shown in the top figure with three lines.

The resolution of  $\Delta E$  for the whole energy of  $\Sigma$  beam is estimated to be better than  $\sigma_{\Delta E} = 5.5$  MeV. From estimation by a simulation of the  $\Sigma p$  scattering experiment, the resolution of  $\Delta E$  was required to be better than 7 MeV to achieve the accuracy of the cross section better than 10% as shown in Table 2.3. Because the  $\Delta E$  resolution estimated from the actual CATCH performances satisfies the requirement, the differential cross section of the  $\Sigma p$  scattering events is considered to be derived within the accuracy of  $\pm 10\%$ . This result indicates that experimental data of the scattering cross sections which can be compared with different theoretical models will be taken for the first time from the  $\Sigma p$  scattering experiment with the CATCH system. It will open a new era in the study of the baryon-baryon interactions.

## Chapter 7

### Summary

We are planning to perform a  $\Sigma$ -proton scattering experiment at J-PARC (J-PARC E40) in order to investigate the baryon-baryon interaction and to confirm the repulsive force due to the quark Pauli effect, which is considered as one of the origins of the repulsive core in the nuclear force.

According to theoretical models based on quark-gluon picture for the short range part of the baryon-baryon interactions, the  $\Sigma^+p$  channel is expected to have an extremely repulsive core due to the Pauli effect in the quark level. In addition, measurement of the  $\Sigma^-p$  channel is also necessary to test the present theoretical models based on meson exchange picture with the flavor SU(3) symmetry.

In the past experiment at KEK, all particles related to the scattering reaction needed to be measured with the “imaging method” by using imaging detectors such as a scintillating fiber active target to identify the scattering event. However the detector response was slow and thus the meson beam intensity was limited to be 250 k/spill (spill  $\simeq$  2 seconds). Due to both the underlying experimental difficulty due to the hyperon’s short lifetime and the low beam intensity, the number of the detected scattering events was only a few tens.

In order to measure the cross section with high statistics and a good accuracy, we introduce a new identification method of the scattering event. In this new method, momenta of a  $\Sigma$  beam and a recoil proton are used without detecting  $\Sigma$  particle directory, and the scattering event can be identified by checking the kinematical consistency that is represented by “ $\Delta E$ ”.  $\Delta E$  is defined as a difference between two values for the recoil proton energy obtained by two different methods. The first value ( $E_{p_{calc}}$ ) is a calculated energy of the recoil

proton kinematically from the  $\Sigma$  beam energy and the scattering angle. The second value ( $E_{p_{measure}}$ ) is an actually measured energy. For the  $\Sigma p$  scattering events, the  $\Delta E$  distribution has a peak around zero. From the number of the peak counts, we can derive the cross section of the scattering. Because any slow detectors are not used in this method, a high intensity  $\pi$  beam can be used in order to produce many  $\Sigma$  particles

In order to realize the new experimental method, detector systems for both the  $\Sigma$  beam reconstruction and the recoil proton detection were essential. For the  $\Sigma$  beam reconstruction, the existing spectrometer systems for multi-purposes are utilized. On the other hand, the recoil proton detector should be a dedicated system with a large acceptance and sufficient performance for detecting  $\Sigma p$  scattering events. For this reason, we developed a new detector system called CATCH (Cylindrical Active Tracker and Calorimeter system for Hyperon-proton scattering).

In the  $\Sigma p$  scattering experiment at J-PARC, a high intensity  $\pi$  beam of  $2 \times 10^7/\text{spill}$  (spill  $\simeq 2$  seconds) is used to produce as many  $\Sigma$  beams as possible via the  $\pi^\pm p \rightarrow \Sigma^\pm K^+$  reaction. The momenta of the  $\pi$  beam and the scattered  $K^+$  are analyzed by the spectrometers to reconstruct the momentum of the produced  $\Sigma$  particle.  $\Sigma$  beams around 500 MeV/ $c$  are tagged by the spectrometers. The scattering angle  $\theta$  and the kinetic energy of the recoil proton is measured by CATCH to identify the  $\Sigma p$  scattering events.

CATCH consists of a Cylindrical Fiber Tracker (CFT) and a bismuth germanate (BGO) calorimeter. These detectors were required to satisfy sufficient performances for the energy resolution, the time resolution, the angular resolution, the acceptance and so on for realization of the  $\Sigma p$  scattering experiment.

The CFT consists of four straight layers and four spiral layers made of about 5000 scintillation fibers with a diameter of 0.75 mm. Each fiber signal is read by a Multi-Pixel Photon Counter (MPPC) fiber by fiber. The fabrication of CFT was performed by introducing some new technical ideas of the fiber position fixing method. As for the BGO calorimeter, 24 BGO crystals are placed in order to surround CFT. The size of one crystal piece is  $30 \times 25 \times 400 \text{ mm}^3$ . The waveform of the BGO signal is readout with a Flash ADC in order to separate pile-up events.

Since the fiber position was slightly deviated from the designed position, the fiber position was corrected in the off-line analysis with cosmic ray measurement

data.

We performed a test experiment to operate the CATCH system and to evaluate the performances for the first time. The experiment was performed in January 2017 at CYRIC (Cyclotron Radio Isotope Center, Tohoku University, Japan). An 80 MeV proton beam was irradiated on a polyethylene (CH<sub>2</sub>) target installed inside CATCH and the scattered proton was measured by CATCH.

The measured energy with CFT and the BGO calorimeter were calibrated using the  $pp$  scattering data from the energy of scattered protons which depends on the scattering angle measured by CFT. The angular resolution of CFT was evaluated to be 1.6 degrees ( $\sigma_\theta$ ) from the opening angle between two protons emitted from  $pp$  scattering. The energy resolution of the BGO calorimeter was obtained to be 1.5%  $\sigma_{E_{BGO}}$  for 80 MeV proton, and that of CFT was obtained to be better than 20% for the energy deposit of a proton in CFT from 8 MeV to 20 MeV.

These performances affect the resolution of  $\Delta E$  ( $= Ep'_{calc} - Ep'_{measure}$ ), which is used to identify the scattering events. The sufficient  $\Delta E$  resolution is necessary to distinguish the scattering events from the background. The  $\Delta E$  resolution for the  $pC$  scattering was obtained to be about 2.3 MeV ( $\sigma_{\Delta E}$ ).

The  $\sigma_{\Delta E}$  depends on the beam energy and kinematics, the estimation for the  $\Sigma p$  scattering experiment is necessary. Based on the obtained angular resolution and energy resolution of CFT and the BGO calorimeters, the  $\Delta E$  distribution of  $\Sigma p$  scattering was estimated to be better than 5.5 MeV ( $\sigma_{\Delta E}$ ) for all conditions. This value satisfies the requirement of 7 MeV ( $\sigma_{\Delta E}$ ) to well discriminate the  $\Delta E$  peak from background.

The (relative) differential cross sections of the  $pp$  and  $pC$  scatterings were derived with CATCH and the  $\Delta E$  method, and they were found to be consistent with past experimental data within 10%. For the newly developed CATCH system, we have established an analysis method for deriving the cross section. Thus we have confirmed that the CATCH system has sufficient performances for the  $\Sigma p$  scattering experiment at J-PARC.

# Bibliography

- [1] M. M. Nagels et al., Phys. Rev. D15 (1977) 2547; D20 (1979) 1633; P. M. Maessen et al., Phys. Rev. C40 (1989) 2226; Th. A. Rijken et al., Nucl. Phys. A547 (1992) 245c.
- [2] M. Oka and K. Yasaki, Quarks and Nuclei, et. W. Weise, Vol 1 (World Scientific, 1984) 489; K. Yazaki, Nucl. Phys. A479 (1988) 217c; K. Shimizu, Nucl. Phys. A547 (1992) 265c.
- [3] O. Hashimoto, H. Tamura, Prog. Part. Nucl. Phys. 57 (2006) 564-653
- [4] Y. Yamamoto, et al., Progress of Theoretical Physics Supplement No. 185, 2010 72-105
- [5] T. Nagae, et al., Phys. Rev. Lett. 80, (1998) 1605
- [6] T. Inoue et al., HAL QCD collaboration, arXiv:1007:3559 [hep-lat]
- [7] K. Miwa et al.:Document for the J-PARC PAC from P40 [https://j-parc.jp/researcher/Hadron/en/pac\\_1101/pdf/KEK\\_J-PARC-PAC2010-12.pdf](https://j-parc.jp/researcher/Hadron/en/pac_1101/pdf/KEK_J-PARC-PAC2010-12.pdf)
- [8] J. Haidenbauer, et al., Nucl. Phys. A 915 (2013) 24-58
- [9] F.Eisele, et al., Phys. Lett B 37 (1971)
- [10] J.K. Ahn et al., Nucl. Phys. A648 (1999)
- [11] H.Kanda et al., Nucl. Phys. A 761 (2005)
- [12] Y.Kondo et al., Nucl. Phys.A 676 (2000)
- [13] K. Miwa et al.: Proposal for an experiment at J-PARC, [http://jparc.jp/NuclPart/pac\\_1101/pdf/KEK\\_J-PARCPAC2010-12.pdf](http://jparc.jp/NuclPart/pac_1101/pdf/KEK_J-PARCPAC2010-12.pdf)

- [14] K. Miwa, Technical Design Report from E40 (2015)  
[http://lambda.phys.tohoku.ac.jp/~miwa9/E40/doc/doc\\_20150515\\_en.pdf](http://lambda.phys.tohoku.ac.jp/~miwa9/E40/doc/doc_20150515_en.pdf)
- [15] M.L. Good and R.R. Kofler, Phys. Rev. 183 (1969) 1142.
- [16] D.J. Candlin et al. Ncl. Phys. B226 (1983) 1.
- [17] Y. Akazawa, Master's thesis, Tohoku university (2014) (Japanese),  
[http://lambda.phys.tohoku.ac.jp/~rdb/human\\_resource/thesis/2008\\_B\\_1\\_M\\_1.pdf](http://lambda.phys.tohoku.ac.jp/~rdb/human_resource/thesis/2008_B_1_M_1.pdf)
- [18] Kuraray scintillation fiber, <http://kuraraypsf.jp/index.html>
- [19] M. Ikeda, Master's thesis, Tohoku university (2017)  
[http://lambda.phys.tohoku.ac.jp/~db/human\\_resource/thesis/2011\\_B\\_1\\_M\\_1.pdf](http://lambda.phys.tohoku.ac.jp/~db/human_resource/thesis/2011_B_1_M_1.pdf)
- [20] R. Honda, et al., PoS PhotoDet2012 (2012) 031.
- [21] T. Shiozaki, Master's thesis, Tohoku university (2015) (Japanese),  
[http://lambda.phys.tohoku.ac.jp/~db/human\\_resource/thesis/2009\\_B\\_2\\_M\\_1.pdf](http://lambda.phys.tohoku.ac.jp/~db/human_resource/thesis/2009_B_2_M_1.pdf).
- [22] EASIROC developed by Omega/IN2P3, <http://omega.in2p3.fr/>
- [23] Y. Akazawa et al., Nuclear Instruments and Methods in Physics Research A, Elsevier B.V., 787, 193-196 (2015).
- [24] R. A. Arndt, et al., Phys. Rev. C 76, 025209 (2007)
- [25] S. Kato et al., Phys Rev C Nucl Phys. 1985 May;31(5):1616-1632
- [26] M. Ieiri et al., NIM in Phys. Res. A257, 253 (1987)